FREQUENCY SYNCHRONIZATION TECHNIQUES FOR COORDINATED MULTIBASE MIMO WIRELESS COMMUNICATION SYSTEMS

by

Bradley Zarikoff

M.A.Sc., Simon Fraser University, 2004

B.Eng., University of Victoria, 2002

A THESIS SUBMITTED IN PARTIAL FULFILLMENT
OF THE REQUIREMENTS FOR THE DEGREE OF
DOCTOR OF PHILOSOPHY
in the School
of
Engineering Science

SIMON FRASER UNIVERSITY
Fall 2008

APPROVAL

Name: Bradley Zarikoff

Degree: Doctor of Philosophy

Title of thesis: Frequency Synchronization Techniques for Coordinated Multi-base MIMO Wireless Communication Systems

Examining Committee: Dr. Daniel Lee
Chair

Dr. James K. Cavers, Senior Supervisor

Dr. Paul K. M. Ho, Supervisor

Dr. Rodney Vaughan, Supervisor

Dr. Sami Muhaidat, Internal Examiner

Dr. Steven D. Blostein, External Examiner,
Professor, Department of Electrical and Computer Engineering
Queen's University

Date Approved: _____

Abstract

This thesis is a study into the synchronization of the downlink of a coordinated multi-base/multiuser (CMBMU) system. The goal of CMBMU systems is to form a system-wide MIMO network using multiple co-channel basestations (BSs) and mobile subscribers (MSs). Compared to existing cellular systems, CMBMU benefits include increased micro- and macrodiversity.

The effects of channel and system impairments on the sum-rate capacity of a linear downlink CMBMU beamforming technique are examined in order to establish which impairments are most problematic. The presence of multiple carrier frequency offsets (CFOs) within the system is identified as the largest problem. It is demonstrated that the effect of local oscillator induced CFO on the sum-rate capacity is more significant than Doppler-induced CFO.

Then, multi-CFO estimation techniques are explored. A MS-side estimator that exploits the convexity of the maximum likelihood (ML) metric is derived. Since convexity of the ML metric is dependent on the length of the training sequence and the severity of the CFO, segmentation methods that guarantee convexity of the ML metric are formulated. The performance of both the convex estimators and the segmentation methods are shown to asymptotically meet the Cramer-Rao lower bound for multi-CFO estimates.

As it is impossible for the MS to correct for the BS CFOs in the CMBMU downlink, an estimation and correction technique that requires co-operation between the BSs and MSs is presented. The initial MS-side estimates, which are fed back to the BSs, are shown to be biased. The proposed technique overcomes this bias, with the end result being that the entire system is brought to a common carrier frequency.

During multi-CFO estimation, additional channel impairments such as timing offset,

frequency selective channels and time selective channels can complicate matters. Straightforward modifications to the ML metric are made that compensate for timing offset and frequency selective channels. A new ML metric based on a parameterized channel estimate that uses the autocorrelation function of the channel gains is used to compensate for time selective channels. Improvements to the CFO MSE of nearly two orders of magnitude are achievable over using the original channel estimator.

Keywords: basestation coordination; beamforming; carrier frequency offset; fading channel; MIMO systems; mobile communication systems

To Emillie and Nikolai.

"To venture causes anxiety, but not to venture is to lose one's self.... And to venture in the highest is precisely to become conscious of one's self."

— Søren Kierkegaard, Danish philosopher, 1813-1855

Acknowledgments

First, to my senior supervisor Jim, I would like to express my most profound appreciation for his exceedingly patient, solid, and intuitive style of teaching, which encouraged me to pursue these studies. I can only hope that I can return the favour to others in the years to come. Financial assistance from the Natural Sciences and Engineering Research Council of Canada (NSERC) was greatly appreciated. I would also like to recognize support from Simon Fraser University, the School of Engineering Science, the Faculty of Applied Science and the Dean of Graduate Studies. And thank you to my partner Emillie, whose encouragement and praise supported me throughout my graduate degrees. Emillie, you gave me the sun.

Contents

List of Tables

List of Figures

List of Abbreviations

AWGN additive white Gaussian noise

BC broadcast channel

BD block diagonal

BER bit error rate

bps/Hz bits per second per Hertz

BPSK binary phase shift keying

BS basestation

BSC basestation controller

ccdf complementary cumulative distribution function

CDMA code division multiple access

CE combining estimator

CFO carrier frequency offset

CIPT channel-independent performance training

CMB coordinated multibase

CMBMU coordinated multibase/multiuser

CMA complex multiply and add

CPM continuous phase modulation

CRLB Cramer-Rao lower bound

CSI channel state information

dB decibels

DCS digital communication system

DPC dirty paper coding

EPT equal power transmission

FDMA frequency division multiple access

FFT fast Fourier transform

FIM Fisher information matrix

GHz Gigahertz

Hz Hertz

i.i.d. identically and independently distributed

ISI inter-symbol interference

km/h kilometres per hour

LO local oscillator

LS least squares

m metres

MAC multiple access channel

MCE MS-side CFO estimate

MCS mobile communication system

MF matched filter

MIMO multiple-input/multiple-output

ML maximum likelihood

MS mobile subscriber

MSE mean square error

MSS mean square spread

MU multiuser

MUD multiuser detection

OFDM orthogonal frequency division multiplexing

PCE parameterized channel estimator

pdf probability density function

PO phase offset

ppm parts per million

PSD power spectral density

PSK phase shift keying

QAM quadrature amplitude modulation

QCE quasi-static channel estimator

rad radians

RF radio frequency

s seconds

SDMA space division multiple access

SE segmented estimators

SIMO single-input/multiple-output

SISO single-input/single-output

SINR signal to interference and noise ratio

SNR signal to noise ratio

ST-AO simultaneous training - assumed orthogonality

ST-G simultaneous training - gradient step

ST-N simultaneous training - Newton step

STC space-time coding

SVD singular value decomposition

TDM time division multiplexing

TDMA time division multiple access

TE telescoping estimator

TO time orthogonal

TS training sequence

W Watt

ZF zero-forcing

Preface

This preface summarizes published and submitted works that are associated with this thesis, and were done as part of my Ph.D. studies at Simon Fraser University. The full citations are given in the bibliography.

The topic I chose for in-depth literature review was that of downlink transmission in multiple-input/multiple-output (MIMO) systems. Much of the literature consisted of novel methods for interference mitigation between downlink streams and for resource allocation to maximize the system throughput. The topic of synchronization was rarely encountered in these capacity- and interference-oriented papers, and so my focus shifted to the practical aspects of the MIMO downlink. At this point, the topic of macrodiversity, which is popular with my senior supervisor, came up. After doing a literature search on macrodiversity systems (referred to in this thesis as coordinated systems) for the MIMO downlink, I decided to focus on carrier frequency offset (CFO) synchronization.

My initial research was on multi-CFO estimation at the mobile subscriber (MS). Although there existed a few publications on the topic (related to Doppler-induced multiple CFOs), there were a number of shortcomings that I identified. My first publication [89] began with the justification for multi-CFO estimation based on multiple independent local oscillators (LOs) instead of Doppler. This led to an efficient gradient-based convex CFO estimator, with benefits over existing multi-CFO estimators shown via simulation. A major extension to this work [91] included a segmented estimator that was capable of operating with any length of training sequence and any CFO magnitude. The Newton-based convex CFO estimator was also presented, as was the Cramer-Rao lower bound for CFOs originating from multiple-LOs.

The second major work included basestation (BS) CFO estimation and correction techniques, and has recently been submitted for publication [92]. This included the work on

maximum likelihood (ML) BS CFO estimation and the structure of MS-side CFO estimate feedback and correction.

The extension of the convex estimators to compensate for time-selective channels is covered in [90]. This work included both coverage of the estimate error and the derivation of the parameterized channel estimate. The specifics on CFO error performance are not included in [90]. This work shows the performance improvement possible with the use of the parameterized channel estimate.

The relation between this thesis and the work published during my Ph.D. research is summarized as follows:

- The capacity expressions and some of the figures in Chapter 3, along with the Gradient method of Section 4.2.1, is presented in [89].
- The work done in [91] includes the Newton estimator in Section 4.2.2, the segmented estimators presented in Section 4.4, the complexity comparison in Section 4.5, and the extension to symbol asynchronous and frequency selective channels in Section 4.6.
- Chapter 5 is a summarized version of the work submitted in [92], on BS CFO estimation and correction.
- The modified ML metric in Chapter 6, including the CFO and channel state information mean square error, is presented in [90].

Chapter 1

Introduction

Multiple antenna systems are proving to be an essential component of high capacity wireless networks. The traditional communication system trade-offs between bandwidth and power have been joined by a third variable; the number of antennas. With intelligent antenna array and algorithm design, the capacity of these multiple-input/multiple-output (MIMO) systems can be increased in proportion to the number of antennas [75]. In lieu of a system provider having to purchase additional wireless spectrum, they now have the choice of adding additional antennas to their basestation (BS) or mobile subscriber (MS).

Spurred on by the past work into MIMO systems, current state-of-the-art research into the physical layer of communication systems focuses heavily on the maximization of capacity. Capacity is the theoretical maximum achievable data rate of the users in the system. Both the uplink and downlink have a number of well-known techniques that may be used to approach the capacity of a MIMO system. In the uplink, multiuser detection techniques such as the linear suppression filters [15, 84] and turbo techniques [77] are popular. For the downlink, spatial multiplexing in the form of singular value decomposition (SVD) filters [72] or optimum beamforming [14, 59, 78] are used.

At the same time, the concept of coordination of the BSs has been suggested as a way of increasing the capacity beyond that achievable by traditional cellular systems. The benefits of BS coordination, also called macrodiversity or network MIMO, were first quantified by Yeh et al. in 1984 [86] for the case of hard BS selection for both uplink and downlink channels. Modern BS coordination research focuses on a soft combination of the BS signals. Uplink techniques include intelligent techniques such as that proposed by Welburn et al. in [81], which combines the signals at the coordinated BSs using the optimum maximum

likelihood criterion. The concept and capacity of coordinated code division multiple access (CDMA) systems has been intensively explored [30, 61, 81, 82], while the downlink capacity of coordinated narrowband systems has been explored by Bacha et al. in [3]. As well, some of the problems associated with coordinated BSs are mirrored in the area of cooperative MS communications, in particular with regards to carrier frequency offset [7, 49, 76].

An area of overlap between the research areas of system capacity and BS coordination is the coordinated multibase/multiuser (CMBMU) downlink. In a CMBMU system, the BSs coordinate their signal transmissions to create what is effectively a giant distributed MIMO antenna. Related work includes efforts to minimize spatial correlation between co-located antennas by Dawod et al. in [19], an investigation into an orthogonal frequency division multiplexing (OFDM) based CMBMU system by Shao and Roy in [68], and a beamforming analysis that uses a linear model of coordinated BSs by Ng et al. in [53].

While practical considerations for downlink beamformers have been considered in the past [42, 45], they have been largely ignored for the CMBMU system. CMBMU systems pose new and different problems that result from the physical separation of the BSs. The ambitious task of coordinating transmissions from geographically separate radio transmitters invites skepticism. However, this thesis presents solutions for the major impediment of carrier frequency offset, as a step towards implementation of CMBMU systems

Although many published studies consider the concept of CMBMU systems, the novelty in this thesis is that there are no existing works that consider the CMBMU synchronization problem. The following sections give further detail on the motivation for this thesis.

1.1 Motivation

This section provides the motivation behind the research presented in this thesis. Justification for coordinated multibase/multiuser systems is presented, along with a summary of common assumptions made during system analysis that must be dealt with before implementation.

1.1.1 Mobile Communication System Capacity

The theoretical capacity of a communication system is a measure used to determine the limits on the obtainable data throughput. In order to meet the needs of current mobile applications, research engineers are constantly looking for ways of increasing this capacity.

Capacity is generally defined using the capacity theorem (see Section 2.1.2). As mentioned in the introduction, MIMO capacity includes the effect of multiple antennas, where the maximum capacity obtainable is proportional to the number of transmit antennas and the logarithm of the individual signal to noise ratios (see Section 2.1.3 for a more detailed discussion). Thus, the more antennas in the system, the more capacity.

However, the effect of the mobile communication channel is not inherently reflected in the capacity expressions. That is, a BS may be transmitting to a MS that is in a shadow region, which is defined as a region that has very high attenuation due to the surrounding environment such as buildings or hills. Even though the antennas may be spaced far enough apart to experience uncorrelated multipath in the microdiversity scale, these shadow regions introduce dependence on the macrodiversity scale. To combat the shadowing effect, distributed antennas can be employed, provided that the antennas are stationed far enough apart that they experience independent shadow effects.

The vast majority of mobile communication systems in use rely on the cellular model. By design, the cellular system places BSs in areas that experience independent shadowing. This makes cellular systems an ideal opportunity to implement the equivalent of a distributed antenna system, and collapse the traditional cellular model in favour of a single, large, distributed MIMO antenna array. The additional antennas will provide additional microdiversity, while the separated BSs will provide macrodiversity to improve the systems resistance to shadowing.

1.1.2 Common Assumptions

As communication systems are very complex, it is common for researchers to simplify the models. This simplification allows for interesting observations, but it gives an inaccurate depiction of system performance, as the simplifications routinely neglect channel impairments in the communication system model.

In the RF subsystem, impairments might include the frequency response of the antenna and amplifier, along with all accompanying matching circuitry. These impairments are very difficult to include in the communication system model, as they are based on the individual components, and are generally only accurate to within a few percent of a mean value. The best simulations would therefore require expectation over the component value distributions, an incredibly complex and almost impossible feat. For these effects, it is best to assume that the effects are negligible, or at the least, can be mitigated by intelligent circuit design. There

also exists the impairment of inaccurate oscillator frequencies, used for signal upconversion and downconversion. This phenomena, referred to as carrier frequency offset (CFO), is more easily modeled within the signal model.

For the channel, impairments that are ignored in commonplace models include the accuracy of the channel state information (CSI), the CFO due to the Doppler frequency (see Section 2.1.3), and the timing offset that exists among the various BSs and MSs in the communication system. These impairments are easily incorporated into the communication system model as additional parameters.

It should be noted that while there are many studies that neglect these model parameters, there also exists a subset of studies that focus directly on them. The effect of channel state estimation errors in MIMO channels have had intensive study [27, 31, 40, 41]. For CFO and timing offset, model-dependent synchronization techniques exist that take advantage of the system structure; for example, the parameter estimation schemes designed specifically for OFDM systems [10, 36, 46, 48]. However, no previous studies take into account the specific system structure of CMBMU systems.

1.2 Goals and Contributions

The goal of this thesis is to investigate the effects of channel impairments on the downlink of coordinated multibase/multiuser systems, and to devise solutions that correct or compensate for any capacity loss. Of particular interest is carrier frequency offset due to independent local oscillators, for reasons that will be made apparent in Chapter 3. This is done through an examination of the system capacity and error analysis of estimates of the CSI. The CSI is defined as the combination of CFOs, timing offsets, and channel gains.

1.2.1 Evolution of Wireless Systems

With respect to current or upcoming wireless system standards, the technique of coordinated beamforming is being considered in Mobile WiMAX [23] and the advanced Long Term Evolution (LTE) of 3G systems [56]. In both standards, downlink beamforming is being considered as a means of increasing the signal to interference and noise ratio (SINR) at the MS. While exact details of how a specific beamforming technique may overlay these standards is not considered in this paper, a few general comments are provided here.

Although this thesis does not explicitly consider multicarrier systems, many of the algorithms and techniques presented herein are applicable and/or easily adapted to suit. Specifically, the effect of additional inter-carrier and inter-user interference in a multicarrier system can be incorporated into the objective function for joint channel state and CFO estimation.

Further, in terms of the channel model, the proposed algorithms and techniques are particularly suited to systems that operate in dense multipath with medium/suburban to low/urban mobility. This is demonstrated in Chapter 3, and suggests that the proposed algorithms are particularly well suited for use in emerging 4G systems [56].

1.2.2 Objectives

Channel impairments inevitably lead to some degree of capacity degradation. The first objective is to examine the effects of various channel impairments on the downlink of a CMBMU system. The rationale behind the inclusion of a specific channel impairment in the system model will also be verified.

Methods of correcting for the channel impairments in the CMBMU system are essential to practical applications. Before correction can be accomplished however, high quality estimates of the CSI must be made, where estimate quality is general related to low mean square error (MSE). The second objective of this thesis is to examine channel impairment estimation and/or compensation. Of most interest is carrier frequency offset. Further complications such as frequency-selective channels, time-selective channels, and timing offset will be included as nuisance parameters, although further investigations could provide enough material for a second thesis.

The specific impairment of carrier frequency offset for downlink CMBMU systems is interesting in that it cannot be corrected for at the MS-side. This is a result of the beamformer weights at the coordinated BSs. Thus, the third objective is to examine the correction of the BS local oscillators using parameter estimation techniques.

In summary, the primary objectives of this thesis are:

- to identify the extent that channel impairments of carrier frequency offset and time-selective channels impair the capacity of the downlink of a CMBMU system,
- to create efficient estimation techniques for multiple carrier frequency offsets,

- to devise a metric for estimation of carrier frequency offset capable of operating in a time-selective channel, and
- to create estimation and correction techniques for basestation carrier frequency offsets.

1.2.3 Contributions

This thesis provides a number of novel contributions to the emerging area of cooperative multibase/multiuser systems, and to the estimation of signal properties more generally. In particular,

- it provides the only investigation to date of the effect of multiple independent BS CFOs on the capacity of a CMBMU downlink,
- it provides the best estimator to date of multiple frequency offsets in static channels,
- it provides the only estimator to date of multiple frequency offsets in fading channels,
- and, it provides the only method to date of bringing separate BSs to a common operating carrier frequency through use of estimates fed back by the MSs.

In more detail, the specific contributions and a brief summary of the results presented in this thesis are listed below:

- It was identified that the capacity of the downlink of a CMBMU system is dependent on the magnitude of the CFOs, the number of MSs, and the system signal to noise ratio (SNR), and is only marginally dependent on the number of BSs within the system. Also, when comparing the CFO due to independent local oscillators to the CFO resulting from the Doppler spread, it was verified that for normal values of local oscillator accuracy and relative mobile speed that the local oscillator effect is greater. This is also demonstrated for the capacity effects of a time-selective (i.e., fading) channel.
- Efficient multi-CFO estimators were devised. The proposed estimators are capable of achieving the lower bound in error performance, while using simultaneous training sequences to maximize the data rate per frame. Compared to existing time division multiplexed estimators, the proposed estimators require a lower peak power and have a greater time aperture, hence greater resolution, than the existing methods that are

practically implementable. Through the use of a novel segmentation process, it is shown that these estimators are capable of compensating for any magnitude of CFO.

- Although the capacity simulations demonstrate that time-selective channels do not have as large an effect as CFO, CFO estimation in the presence of a time-selective channel is a major concern. Simulations demonstrate the effect that time selectivity has on CFO and CSI estimation. To compensate, a new CFO estimator was devised that relies on a model of the channel autocorrelation. This work appears to be the first to address the problem of multiple frequency offset estimation in a time-selective channel. Simulations were performed that demonstrate that the design parameters for the time-selective CFO estimator must be carefully chosen to match the channel conditions.

- Since the MSs are incapable of compensating for multiple CFOs when downlink beamforming techniques are used, a CFO "tightening" technique was devised, by which the BSs correct their frequencies on the basis of feedback from the MSs. The tightening technique involves maximum likelihood estimators for individual BS and MS CFOs and a single frame of MS-side CFO estimate feedback. Also, BSs and MSs make corrections by shifting their carrier frequencies. The technique is capable of reducing the BS CFO spread considerably. While the addition of MSs improves the techniques performance, the addition of BSs marginally degrades the performance. The performance in systems with large variations in the BS to MS channel SNR is also demonstrated, with very favourable results.

1.3 Dissertation Organization

This thesis consists of four main parts, not including the background presented in Chapter 2. Chapter 3 examines the effect of CFO in the CMBMU system using expressions for the theoretical capacity. Simulations are used to demonstrate the effect of CFO, and contrast it to the effect of time-selective channels. The specific example of zero-forcing beamforming is used. In Chapter 4, ways of estimating multiple CFOs at the MSs are examined. In Chapter 5, estimation and correction of the BS CFOs are investigated. Lastly, time-selective channels are included in the CFO estimation model in Chapter 6, and a new metric is proposed that will accommodate fast fading channels. Conclusions are presented in Chapter 7.

Chapter 2

Background

This chapter provides a reference for theory and models used within the thesis. An overview of the notation and system model is also presented. In Section 2.1, a broad overview of the general communication system, including a brief description of system capacity, the fading channel, and the MIMO channel. Section 2.2 presents the high-capacity multi-user physical layer transmission schemes that are proposed for CMBMU systems, while Section 2.3 contains details on the central idea of multi-base coordination. Finally, the system model is presented in Section 2.4 and consists of components from the preceding sections.

2.1 Communication Systems

The primary goal of a digital communication system (DCS) is to transmit binary data from a source to a sink (see [57] for a full treatment or [70]-[71] for a tutorial review). This is extended to multiple sources and sinks in Section 2.2. For both the wired and wireless variations on the DCS, transmission of the data uses electromagnetic fields as the propagation medium [35]. The specific application of the transmitted data is generally not a concern of the physical layer communication system design, and thus will not be considered here. For a basic DCS, random noise can cause errors in the detection process. At the sink, thermal noise is introduced to all frequency bands. Accordingly, the primary goal of a digital communications engineer is to optimize the power and bandwidth to allow for efficient detection of the original binary data embedded in the thermal noise. This optimization takes the form of a combination of coding, modulation, and detection schemes. The DCS can be broken into a small number of functionally specific blocks, as shown in Figure 2.1. Note

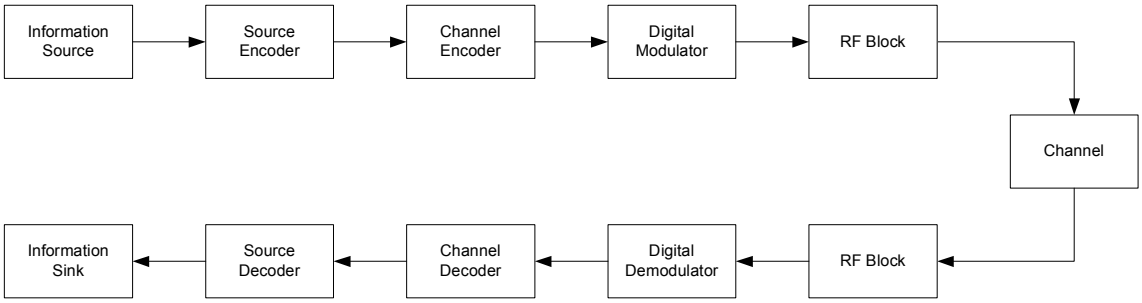

Figure 2.1: Block structure of a digital communication system (modified from [57]).

that although the source provides binary data for transmission, it is common to group bits into symbols of a higher dimension during the modulation step. Also note in Figure 2.1 that the various blocks at the source and sink provide inverse operations to one another.

The majority of DCSs rely on source and error correction coding. Source coding removes redundant information from the binary data at the source ([17], Chap. 5); this technique is used to minimize the amount of transmitted data, and effectively reduces the number of symbols that must be transmitted from source to sink. On the other hand, error correction coding seeks to add redundant information to the binary data [83]; by adding data-dependent symbols, this redundancy is used at the sink end of the communication link to increase the probability of selecting the correct symbol in the presence of channel impairments.

After coding, the data stream is modulated to the desired format for transmission over the electromagnetic medium. Modulation formats exist in both linear and non-linear form. Linear modulation, such as phase shift keying (PSK) and quadrature amplitude modulation (QAM), map m binary symbols onto one of $M = 2^m$ possible symbols. In essence, the modulator must choose from a "finite alphabet" of M potential symbols for every m bits that are input. A pulse shape is then applied to the modulated symbol, which defines how the signal utilizes the electromagnetic spectrum. That is, the desired bandwidth, power and symbol rate are all required to define the pulse shape. The sink uses prior knowledge of the pulse shape for efficient detection.

Non-linear modulation, such as continuous phase modulation (CPM), introduces memory between transmitted symbols, extending the effect of one symbol across many symbol periods. Modulation is done on the phase of the carrier, which results in a constant amplitude signal that eliminates the amplitude transitions common to the linear modulation

schemes. The constant amplitude signal, also known as constant envelope, allows usage of efficient non-linear amplifiers at the RF stage. This modulation is termed non-linear since the relation between the data symbols and the complex envelope of the carrier is non-linear.

The final step before transmitting the signal through the channel is the radio frequency (RF) hardware block. In this thesis, the term "radio frequency" is used to include all frequencies higher than baseband. The RF block is arguably the most important component of a DCS, as it facilitates the physical transmission of a signal over the propagation medium. In fact, a basic radio can be designed with only the RF block and information source. Most of the RF block is made up of amplifiers, frequency converters, and filters. For the wireless medium, where the term "wireless" refers to the electromagnetic spectrum, the RF block also includes antennas and a number of associated RF circuitry. This area is commonly overlooked in academic DCS research; it is usually assumed that the RF circuitry is ideal in the sense that there is no signal degradation or non-linearities and that both the source and sink have perfectly synchronized frequencies and timing. However, this is far from the truth, and some texts on DCSs will devote a chapter or more to dealing with these non-idealities.

Much of the current research into DCSs fits into the sub-category of the mobile communication system (MCS) [58]. Whereas other DCSs would transmit via a fixed medium such as coaxial cable or a point-to-point microwave link, MCSs transmit their signal over a time-varying wireless (or mobile) channel. As the term "mobile" suggests, the time-varying nature of the wireless channel stems from the fact that the source and sink are in motion relative to each other; this phenomenon is detailed in Section 2.1.3. The transmitted signal reflects off numerous objects, such that the data sink receives multiple copies of the original; this phenomenon is commonly known as "multi-path." Depending on the system configuration, multi-path can either benefit or degrade the symbol detection process at the sink. The benefits can be realized by using multiple antennas at either or both the source and the sink, as detailed in Section 2.1.4.

The following sections are organized as follows. Section 2.1.1 details the signals used in the MCS model, with Section 2.1.2 providing a short overview of system capacity. Section 2.1.3 gives a commentary of the fading channel mechanism and theory. Lastly, a short summary on the theory of multiple antennas is given in Section 2.1.4.

For this thesis, we assume that the antennas used to access the wireless channel are ideal in the sense that they have unit gain and are perfectly matched to the transmit and receive hardware in the RF block. Also, we do not consider source or error codes, since it is not

pertinent to this study on synchronization.

2.1.1 Baseband Signal Representation

The narrowband signal model is used in this thesis, where narrowband is defined by having a post-modulated symbol bandwidth that does not significantly exceed the coherence bandwidth (see Section 2.1.3 on the fading channel). The n^{th} data bit to be transmitted over the wireless channel is represented as $b\,[n]$. Defining the data or symbol rate as T_s, we can define the BPSK continuous-time modulator output as

$$s(t) = \sum_n b[n]p(t - nT_s), \tag{2.1}$$

where $p(t)$ is the continuous-time pulse shape. The matched filter (MF) $p^*(t - nT_s)$ is used at the receiver to maximize the signal to noise ratio, with the MF response $q(t) = \int_{-\infty}^{+\infty} p^*(\tau)p(t + \tau)d\tau$ used in the following to depict the effect of the pulse after the MF.

Proper design of the pulse shape allows multiple communication signals to share the wireless channel. The pulse shape $p(t)$ is designed with two criteria in mind: to ensure that the bandwidth is limited to W Hertz (Hz), and that inter-symbol interference (ISI) is avoided. The frequency content of the pulse shape $p(t)$ is defined as

$$P(f) = \mathcal{F}\left(p(t)\right) \tag{2.2}$$

where $\mathcal{F}(\cdot)$ represents the Fourier transform; $Q(f)$ represents the frequency content in the MF response $q(t)$. The bandwidth W of $P(f)$ is defined as the highest frequency that contains signal energy, or, for a pulse shape with unit energy, where $\int_{-\infty}^{\infty} |p(t)|^2\, dt = 1$, W must satisfy

$$\int_{-W}^{W} |P(f)|^2\, df = 1. \tag{2.3}$$

In practical implementation, $p(t)$ is truncated in time, resulting in high frequency components in $P(f)$. However, the time truncation is done in such a manner as to, at the least, maintain 95% of the signal energy within the $2W$ pulse bandwidth. For a narrowband wireless system, frequency division multiplexing (see Section 2.2) is accomplished by upconverting independent bit streams to separate carrier frequencies spaced at intervals of $2W$. Specifically, the condition for ISI-free transmission is represented as [57]

$$q(nT_s) = \begin{cases} 1, & n = 0 \\ 0, & n \neq 0 \end{cases}. \tag{2.4}$$

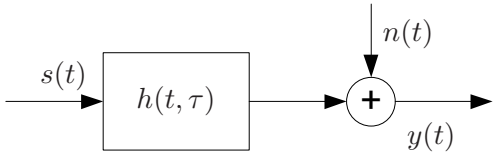

Figure 2.2: Baseband signal model.

In words, the ISI-free condition states that, after matched filtering, the k^{th} pulse will not contribute to any other pulse. The frequency-domain condition for ISI-free transmission was found by Nyquist; that is, the *Nyquist condition for zero ISI* states that the post-MF spectrum must satisfy

$$\sum_{m=-\infty}^{\infty} Q\left(f + m/T_s\right) = T_s. \tag{2.5}$$

By ensuring that W satisfies a maximum value, which is defined as

$$W < 1/2T_s, \tag{2.6}$$

and by using a pulse shape that satisfies (2.4) and (2.5), such as the optimum

$$q_{opt}(t) = \frac{\sin(\pi t/T_s)}{\pi t/T_s} = \text{sinc}(t/T_s), \tag{2.7}$$

perfect ISI-free conditions can be attained. Since a pulse $p_{opt}(t)$ based on the sinc function in $q_{opt}(t)$ has a very slow time decay of $1/t$, alternatives such as the square-root raised cosine pulse are commonly used, with a decay of approximately $1/t^3$ [57].

The baseband channel model is shown in Figure 2.2. It includes both the wireless channel gain and the thermal noise source that is present at the receiver; both phenomena provide challenges for communication system design. The model is represented mathematically as

$$y(t) = \int_{-\infty}^{\infty} s(\tau)h(t,\tau)d\tau + n(t), \tag{2.8}$$

where $h(t,\tau)$ is the time-varying channel gain (detailed in Section 2.1.3) and $n(t)$ is the additive white Gaussian noise that is injected at the receive circuitry. The channel impulse response $h(t,\tau)$ will be defined in full in Section 2.1.3 and the model will be extended to include multiple antenna elements in Section 2.1.4.

2.1.2 Capacity

Given the fairly generic signal model described here, there are still innumerable permutations possible through selection of a coding scheme or symbol weights. In fact, the weighting of transmitted symbols results in what is essentially a digital filter, which enables everything from maximization of the signal-to-noise ratio to multi-user channel access. The capacity of the wireless channel is an important tool that can be used to determine the efficiency of a given communication system model, including the effect of these permutations. Additionally, the effect of channel imperfections can be ascertained in the same way, through modification of the model.

The capacity of a single-input/single-output (SISO) communications channel was first derived for the case of a band- and power-limited memoryless Gaussian channel [32] to be

$$\mathcal{C}_{SISO} = W \log_2 \left(1 + \frac{P}{N_0 W} \right), \tag{2.9}$$

with units of bits per second, where W is the baseband channel bandwidth in Hz, P is the desired signal transmit power, and N_0 is the noise power spectral density (PSD) of the noise at the receiver. Note that for the complex channel that we consider, the bandwidth in (2.9) is replaced with $2W$.

2.1.3 Mobile Fading Channel

As shown in the baseband signal model of Section 2.1.1, the wireless channel impulse response, $h(t, \tau)$, is modeled as a two-dimensional variable. The channel impulse response is a result of both the multipath in the wireless channel and the relative movement between the source, sink and scatterers. Note that not all wireless channels are affected by time-varying multipath; for example, satellite links rely on a line-of-sight path. For this reason, we refer to any wireless channel that is affected by time-varying multipath as a mobile fading channel, or just a fading channel.

Communication systems operating in locations that are rich in scatterers have numerous distinct paths on which the signal may propagate. A scatterer can be any object from light poles to apartment buildings to mountains, with each object reflecting a different amount of the incident signal power due to variable reflection coefficients. The combination of the reflection coefficients and different total path lengths results in different phases, arrival times and power levels for each incident signal at the sink. Upon arrival at the sink, the incident

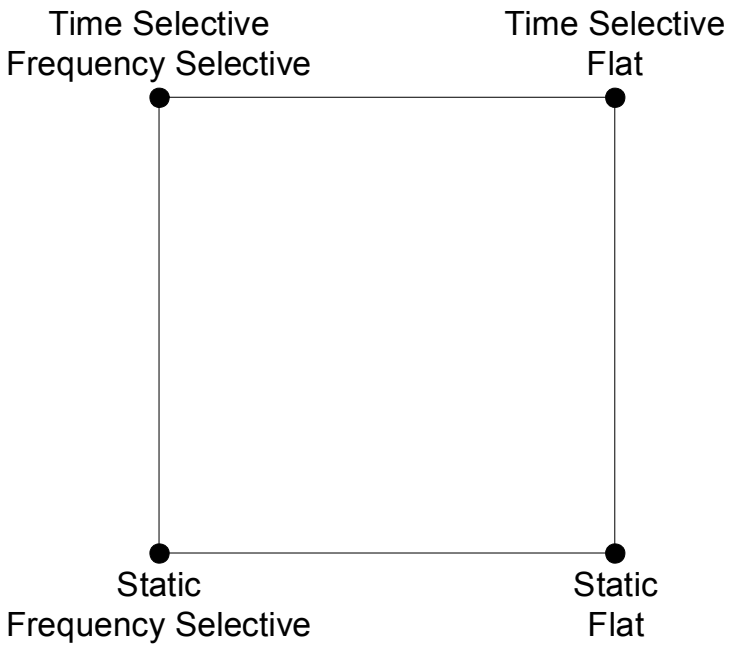

Figure 2.3: Fading channel descriptions.

signals can add either constructively or destructively. As a result, the mobile fading channel can vary in both frequency and time.

As the scatterers may be mobile and the relative delays between the signals may be different, there are many categories of fading channel. The key properties of the fading channel are shown in relation to one another in Figure 2.3. The figure shows four main categories, which are based on one of two critical assumptions: time-selective versus static, and frequency-selective versus flat. Time and frequency-selective channels are defined as those that vary in t and τ, respectively, over a specific time interval or a band of frequencies. The terms 'static' and 'flat' define channels that are insensitive during a specific time interval or band of frequencies. Thus, the 'static/flat' channel will be the least volatile, while the 'time-selective/frequency-selective' will be the most volatile. Note that since static and flat channels are defined over a specific time interval or frequency interval, if this interval were to be increased, the channel might become selective in time or frequency.

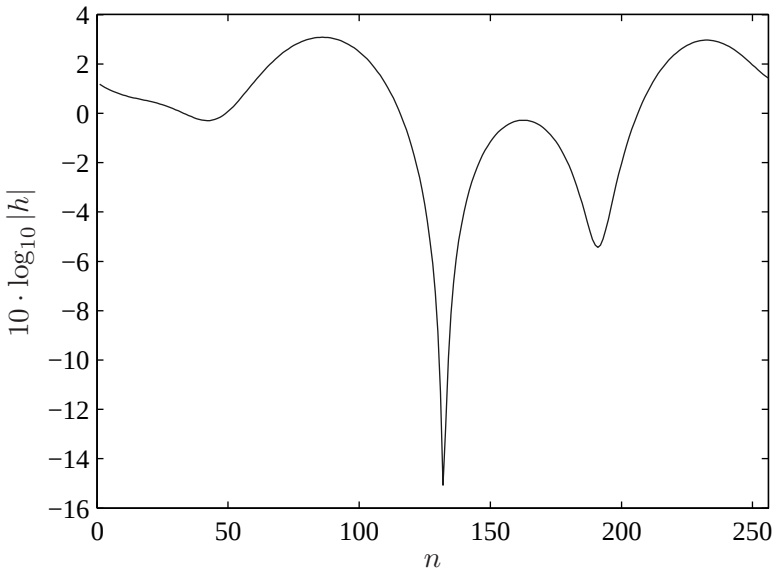

Figure 2.4: Example of a fading channel versus time.

Frequency Selectivity

Frequency selectivity is caused by the delayed arrival of independent multipath signals. Depending on the communication system bandwidth, these delayed arrivals can result in an uneven channel impulse response across the frequency band of interest. The coherence time τ_c is used to define the approximate length of the channel impulse response in seconds. Taking the Fourier transform $\mathcal{F}_\tau\left(h(t,\tau)\right)$ in τ will give the time-varying frequency response of the channel; for example, a channel with a single scatterer results in a Doppler shifted but flat frequency response (one arrival, so that $\tau_c = 0$). For a channel with more than one arrival, the channel gain is variable in frequency, or frequency-selective. In fact, $1/\tau_c$ is referred to as the coherence bandwidth W_c, and denotes the approximate bandwidth over which the frequency response is unchanging; for the ideal flat channel, $W_c = \infty$. It is important to note that there exist multiple definitions for the coherence bandwidth in the literature [12].

Time Selectivity

Time selectivity is caused by the movement of the source, sink and scatterers. Figure 2.4 shows an example channel response. Similar to the coherence bandwidth for frequency-selective channels, a coherence interval T_c can be defined for time-selective channels that conveys the approximate length of time in seconds that $h(t, \tau)$ remains constant. In fact, a fraction of the inverse of the Doppler frequency is generally used to define T_c, so , $T_c = 1/af_d$, where

$$f_d = \frac{v}{\lambda}, \tag{2.10}$$

v is the relative velocity between the transmitter and receiver in metres/second, and λ is the carrier wavelength in metres. Note that two fades can occur in the period $1/f_d$, so common values for a range from $a = 2.4$ to $a = 5.6$ [58].

Fading Channel Model

The channel model used in this thesis relies on the idea of separability between the time and frequency components of the impulse response [12]. In short, this means that the frequency response and the multipath autocorrelation are considered independent; if a more comprehensive model is necessary, the scattering function detailed in [12] can be used.

First, consider the statistics of a single snapshot of the channel impulse response, $h = h(t_0, \tau_0)$. Since we consider the quadrature channel [57], h is considered to be a complex random variable with a magnitude $a = |h|^2$. Assuming that there is no line-of-sight channel, and that there are sufficient scatterers so that the plane waves can be considered Gaussian distributed via the central limit theorem, a can be modeled as a Rayleigh random variable as described in the Jakes model [57, 58], with the pdf

$$p_a(a) = \begin{cases} \frac{2a}{\sigma^2} e^{-\frac{a^2}{\sigma^2}} & (0 \leq a \leq \infty) \\ 0 & a < 0 \end{cases}, \tag{2.11}$$

where σ^2 is the variance of the received signal, so that $E_h[Re^2(h)] = E_h[Im^2(h)] = (1/2)\sigma^2$. Further, assuming transmission of a pure tone, the use of isotropic antennas, and isotropic scattering, a common model for the PSD of the complex gain is

$$S_h(f) = \frac{A}{\pi f_d \sqrt{1 - \left(\frac{f - f_c}{f_d}\right)^2}}, \tag{2.12}$$

where A depends on the gain of the antennas. This PSD is dependent on the relative motion of the sink to the scatterers through the Doppler frequency f_d. The inverse Fourier transform of the Doppler PSD gives the autocorrelation of a, which is also dependent on f_d. The autocorrelation of the channel gain corresponding to (2.12) is

$$R_h(\Delta t) = J_0\left(2\pi f_d \Delta t\right), \tag{2.13}$$

where $J_0(\cdot)$ represents the zeroth order Bessel function [12] and Δt refers to a span of time in seconds. This model provides a generalization to relative motion between the MS and the scatterers to form an approximation to the channel autocorrelation; the assumptions seek to capture the aggregate movement of the entire system via the Doppler spread. The autocorrelation suggests that the correlation between a snapshot of the channel gain (an estimate, for example) and the current channel gain will progressively fall until they can be presumed uncorrelated. This progression is dependent on the Doppler spread, which in turn is dependent on the relative speed between the MS and the scatterers.

The system and channel model notation used in the past few sections is depicted using continuous time, with the continuous variable (t) denoting time dependence. Since the signals used in the models are located before upconversion to the carrier frequency at the source, or after sampling at the sink, the work in this thesis uses discrete notation for the signals. The notation $[n]$ is used to denote the n^{th} sample. From here on, this discrete model will be used exclusively.

2.1.4 MIMO Channel

Multiple input/multiple output (MIMO) channels are defined as having multiple antenna elements at both the source (transmitter) and sink (receiver). MIMO systems can provide two distinct benefits to a MCS: signal diversity and multiplexing [8]. System capacity of MIMO systems has been shown to rise proportional to the number of antennas in the system. In particular, for a system with an equal number of N_T transmit and N_R receive antennas, Telatar [75] demonstrated that the capacity efficiency of a MIMO system in a Gaussian channel can have a linear relationship to the number of antenna elements at the transmitter.

Following from Section 2.1.2, a general system capacity efficiency expression can be derived for the complex discrete MIMO channel [24]. Using the assumption that the components of $\mathbf{s}$ are i.i.d. Gaussian random variables, the general MIMO system capacity is

found to be

$$C = \log_2 \frac{\left|E\left[\mathbf{s}\mathbf{s}^\dagger\right]\right| \left|E\left[\mathbf{r}\mathbf{r}^\dagger\right]\right|}{\left|E\left[\mathbf{u}\mathbf{u}^\dagger\right]\right|}, \tag{2.14}$$

in units of bits per second per Hertz (bps/Hz), where $\mathbf{s}$ is the length-N_T transmit vector for a single time slot, $\mathbf{r}$ is the length-N_R receive vector for the same time slot, and $\mathbf{u} = [\mathbf{s}^T \mathbf{r}^T]^T$ is a length-$(N_R + N_T)$ vector. Although substituting symbols that are drawn from a finite constellation into the $\mathbf{s}$ and $\mathbf{r}$ vectors would invalidate the Gaussian signal assumption, it is widely accepted in the literature as a means to approximate the mutual information obtainable by the constellation.

Both $\mathbf{s}$ and $\mathbf{r}$ in (2.14) can be modified to include the effect of the desired MIMO system model. The complex channel gains for the MIMO channel are defined in the $N_R \times N_T$ matrix $\mathbf{H}$, the transmit symbols in the length-N_T vector $\mathbf{s}$ and the received samples in the length-N_R vector $\mathbf{r} = \mathbf{H}\mathbf{s} + \mathbf{n}$. The length-$N_R$ vector $\mathbf{n}$ represents the complex additive white Gaussian noise present at the receive antennas, with a covariance matrix $E[\mathbf{n}\mathbf{n}^\dagger] = N_0 \mathbf{I}_{N_R}$. The capacity expression is then

$$C_{MIMO} = \log_2 \frac{|N_0 \mathbf{I}_{N_R} + \mathbf{H}\mathbf{S}\mathbf{H}^\dagger|}{|N_0 \mathbf{I}_{N_R}|}, \tag{2.15}$$

where $\mathbf{S} = E[\mathbf{s}\mathbf{s}^\dagger]$ is a $N_T \times N_T$ covariance matrix that denotes the transmitted signal.

Since the publication of seminal works by Telatar [75] and Foschini and Gans [24], there has been a massive amount of work done on MIMO systems. Generally, the two can be split into two groups: diversity and multiplexing MIMO systems.

For a MIMO system to achieve capacity, it must use sophisticated coding over space and time. Eigenbeamforming, a form of MIMO multiplexing that is known to achieve MIMO capacity, can be used when $\mathbf{H}$ is known at both the transmitter and receiver. The method involves eigendecomposition of $\mathbf{H}$. The transmitter and receiver are first assigned sets of eigenvectors. By using these weights in a beamformer, the system is transformed into a set of $N_E = \min(N_R, N_T)$ orthogonal parallel channels. Starting with the SVD of $\mathbf{H} = \mathbf{U}\mathbf{\Sigma}\mathbf{V}^\dagger$, where $\mathbf{U} \in \mathbb{C}^{N_R \times N_R}$ and $\mathbf{V} \in \mathbb{C}^{N_T \times N_T}$ are unitary matrices of eigenvectors and $\mathbf{\Sigma} \in \mathbb{R}^{N_R \times N_T}$ holds the eigenvalues, we can define the transmitted signal covariance matrix as $\mathbf{S} = \mathbf{V}\mathbf{L}\mathbf{V}^\dagger$, where $\mathbf{L}$ is an $N_T \times N_T$ diagonal matrix that holds the power allocated to each of the new N_E spatial sub-channels (note that if $N_E \neq N_T$, then the remaining eigenvectors span the nullspace of $\mathbf{H}$, and are not used in eigenbeamforming). The capacity formula in (2.15) can

be rewritten as

$$C_{SVD} = \log_2 \left| \mathbf{I}_{N_R} + \mathbf{\Sigma L \Sigma}^\dagger \right|, \tag{2.16}$$

where $\mathbf{U}$ is taken outside of the determinant since it is unitary. Water-filling is done over the eigenvalues $\mathbf{\Sigma}$, with the resulting transmit power for each spatial sub-channel entered into the diagonals of $\mathbf{L}$. In the case where the CSI is unknown at the transmitter, it was shown in [24] that the capacity is optimized if $\mathbf{L}$ is set to an identity matrix scaled with the transmit power.

Alternative methods of using the MIMO channel to multiplex MSs or data streams independently from each antenna employ multiuser (MU) detection at the receiver or receivers. The technique of multiuser detection (MUD) is applicable even if no channel knowledge exists at the transmitter. Since MU-MIMO techniques are an enabling technology behind CMBMU systems, they are reviewed in Section 2.2.

Another way of capitalizing on MIMO arrays focuses on using the independent channel gains to smooth the time variations of the MIMO fading channel and boost the amount of energy received. Traditional techniques such as maximum ratio combining [85] make use of diversity at the receiver. By coherently combining the incoming samples from each antenna, the SNR for the current symbol is increased proportionally, while the average channel variation is reduced. A common technique for providing both transmit and receive diversity is space-time coding (STC), which comes in both block and trellis form. The benefit of STCs is that they are capable of using multiple transmit antennas to provide diversity. The term 'space-time code' comes from the fact that the transmit symbols are spread over both time and antenna as prescribed by the specific code. The Alamouti space-time code [2] is most famous for its elegant structure and its diversity and rate properties: operating with $N_R = 2$ and $N_T = 2$ over two symbol times, the Alamouti STC can deliver full fourth-order diversity at full rate (two symbols transmitted over two symbol periods). A major benefit of STCs is that they do not require channel gain information at the transmitters; only the receiver is required to have knowledge of the channel gains.

2.2 Multiuser Communications

This thesis considers narrowband multiuser systems that multiplex users within the same carrier frequency and time slot. The multiuser detection and transmission algorithms use

the spatial signature of the MIMO channel to provide separation in the signal space, and are commonly referred to as space division multiple access (SDMA) techniques.

The idea of multiple data streams occupying the same frequency and time is initially contrary to traditional interference avoidance strategies, since each user will be a direct interferer to every other user. However, in the same way that phased arrays can position a null in the direction of an interferer [33], the diversity of the channel matrix $\mathbf{H}$ provides a multi-path rich environment which signal processing techniques can exploit to provide isolation between the desired signals.

The uplink and downlink channels of MU-MIMO systems are not equivalent. In the point-to-point MIMO system example of Section 2.1.4, the capacity-achieving eigenbeamforming technique can be used since all available spatial diversity can be expended on a single communication link, and both sides have full CSI. However, full CSI may not be available to all MSs for downlink detection or uplink transmission; that is, MS k does not know the CSI of MS k'.

A few definitions are required before continuing: the uplink channel is also referred to as the multiple access channel (MAC). MAC-MIMO algorithms generally use some form of MUD, since the BS uses the spatial signatures of the multiple MSs for detection. The downlink channel is also referred to as the broadcast channel (BC). Algorithms that operate in the BC-MIMO channel, often referred to as SDMA techniques, include beamforming and pre-cancellation techniques.

The following sections present a summary of uplink and downlink techniques.

2.2.1 Uplink

The uplink consists of many MSs transmitting simultaneously to a single BS. For K MSs, the capacity expression for the MAC-MIMO system can be found using (2.14) to be [27]

$$C_{MAC} = \log_2 \frac{|N_0\mathbf{I}_{N_R} + \sum_{k=1}^{K} \mathbf{H}_k\mathbf{S}_k\mathbf{H}_k^\dagger|}{|N_0\mathbf{I}_{N_R}|}, \tag{2.17}$$

where $\mathbf{H}_k$ and $\mathbf{S}_k$ refer to the channel gain matrix and transmit covariance for the k^{th} MS.

In the MAC, when both the BS and all MSs have complete CSI, the transmit covariance matrix $\mathbf{S}_k$ can be customized per user, and the capacity-achieving technique of successive decoding can be used at the BS [27]. This technique makes use of user-specific decoding order and transmission rates to achieve capacity. As such, it is dependent on a downlink

feedback channel to inform the MS as to which transmit power matrix $\mathbf{S}$ should be used. An algorithm that optimizes the capacity of the MAC-MIMO channel through the transmit covariance matrices is that of iterative water-filling [88].

For the more general case where the reverse feedback channel is not available, there exist a vast number of MUD techniques that can be used to distinguish between the incoming signals. With equal power transmission at each MS, MUD techniques range from the finite alphabet-based optimal joint maximum likelihood technique [28] to zero-forcing (ZF) at the receiver [84]. A variety of techniques attempt to bridge this gap between optimal performance/high complexity and sub-optimal performance/low complexity [26, 51, 79, 80, 93].

2.2.2 Downlink

The downlink of a multiuser system consists of a BS transmitting independent data to a number of MSs. For K MSs, the sum-rate capacity expression for the BC-MIMO system can be found using (2.14) to be [27]

$$C_{BC} = \sum_{k=1}^{K} \log_2 \frac{|N_0 \mathbf{I}_{N_R} + \sum_{i=1}^{K} \mathbf{H}_i \mathbf{S}_i \mathbf{H}_i^{\dagger}|}{|N_0 \mathbf{I}_{N_R} + \sum_{i \neq k} \mathbf{H}_i \mathbf{S}_i \mathbf{H}_i^{\dagger}|}. \tag{2.18}$$

Note that all users are considered interference in the BC. This results from the fact that the MS do not have full channel CSI for all users, and thus all interference must be mitigated at the BS.

Since each MS is independent, there is no way for a MS to separate its desired signal from that of the other 'interferers' like in the MAC. An interesting observation in the BC is that assuming that the mobile channel is symmetric, CSI is necessary only at the BS to achieve capacity. This is due to the transmit antenna coordination, where all interference at the receive antennas is either eliminated or minimized. The optimum BC technique is known as dirty paper coding (DPC) [16, 22], named after the ability for a person to distinguish between words on a dirty piece of paper. It uses a variation based on successive cancellation. The DPC technique is computationally intensive because of the requisite complex random coding and vector quantization techniques [87]. Simpler techniques have been established, such as ZF transmission [87] and various adaptive beamforming techniques [5, 21, 29, 55, 59, 60, 64, 65]. Additionally, it has been proven that after equalizing the transmit powers from KN_T MS antennas in the MAC with the N_T BS antennas in the BC,

and assuming symmetric channels, the capacity is identical for both MAC and BC systems [65].

2.3 Basestation Coordination

A coordinated system refers to one in which the BSs coordinate as if all the antennas were located in the same MIMO array. The inter-base communication is done via a dedicated, high bandwidth, land-based communications link. For the BC, BS coordination entails joint selection of the complex weights or prefilters for all antennas, while for the MAC, it entails joint decisions based on the received samples. The desirability of such a scheme is due to the increase of the size of the BS antenna array; with B basestations, where each BS has N_T antennas, the coordinated BSs essentially become a BN_T distributed array. The benefits of BS coordination include: an increased immunity to shadow effects, since now if a MS is in the shadow for one BS, it may not be for another [67]; an increased level of microdiversity, which results in a higher rank channel gain matrix; and an inherent knowledge of adjacent cell user channel states and transmit symbols, which provides the basis for advanced interference cancellation. While the distance between the BSs may cause implementation issues, the potential gains are great.

The idea of merging the traditional cellular structure into a more integrated system is not new. There has been ample investigation into coordinated CDMA systems. Good coverage of general macrodiversity in a CDMA system can be found in [30], where Hanley considered feasibility of a completely coordinated and synchronized network. Romero-Jerez et al. in [61] addressed a simplified form of uplink macrodiversity by allowing multiple BSs to receive a MS signal, with the strongest BS signal used to chose the receiver. They show that while a MS in a non-macrodiversity CDMA system will be allocated to the BS with the best average channel, a MS in a macrodiversity CDMA system will be allocated to the BS with the best instantaneous channel, causing an increase of capacity and a decrease in the severity of the fades. This is true for narrowband systems as well [39]. Kim et al. [38] combined the interference considerations of microcells and macrocells. The uplink consists of a true macrodiversity receiver, where all BS received signals are used for detection. For the downlink, the macrodiversity system chooses the best BS link for transmission, much like the uplink in [61]. It is instructive to note that quasi-orthogonal CDMA systems, which are interference limited like narrowband systems, are restricted in the downlink because the

MS can not make use of the distributed reception available at uplink; as noted in Section 2.2, this is the difference between the MAC and the BC. However, for true orthogonal systems this is not the case, since an ideal system will have orthogonal downlink channels which are noise limited.

Advances in signal processing technology have made implementation of BS coordination in narrowband systems feasible. For narrowband systems, work by Karimifar and Cavers [37] focuses on the reduction of information transfer between coordinated BSs, given a variety of BS cell layouts and MS populations. In [52], Ng et al. adopt a linear BS model, where the BSs are aligned in a linear fashion so that each BS only experiences interference from its two nearest neighbours. A Kalman filter is designed for MUD using this model. For the downlink, the linear BS model is used again in [53], with the Kalman filter modified to coordinated BS transmitters. Some analogous work has been done on techniques that mimic a coordinated network, such as the correlation minimization technique of Dawod et al. in [19]. Expanding on the idea of simple macrodiversity for transmission, it is interesting to note that a coordinated MU-MIMO system could provide a type of soft handoff for narrowband systems, providing some of the capacity gains seen with soft handoff in the wideband systems.

2.4 System Model

This section presents the CMBMU system models used throughout the thesis and the associated signal notation. They include an example downlink beamforming model in Section 2.4.1, a parameter estimation model in Section 2.4.2, and a BS CFO correction model in Section 2.4.3. First, a brief overview of the common system parameters is as follows.

Since we are not concerned with achieving the capacity of the multiuser system, source and error correction coding techniques are not considered. A single antenna-to-antenna communication link is described as follows. A quadrature modulator/demodulator is used, and as a result, the transmitted signal, fading channel, and noise are two-dimensional. An appropriate pulse shape, such as the root raised cosine, is used at the transmitter; the pulse has a bandwidth W. The signal is upconverted, transmitted with a carrier frequency of f_c, and downconverted. At the receiver, a MF is used to maximum the signal-to-noise ratio, and is sampled at a rate f_s, where $T_s = 1/f_s$ is the symbol duration. At the q^{th} antenna of the k^{th} MS, the samples are stored in $y_{k,q}[n]$.

The mobile channel is modeled as follows. To start, no delay spread is included. The magnitude of each complex channel gain $H_{b,m,k,q}[n]$ from the m^{th} antenna of the b^{th} BS to the q^{th} antenna of the k^{th} MS has a Rayleigh distribution. That is, both the real and imaginary components are Gaussian distributed. The variance or power of $H_{b,m,k,q}[n]$ satisfies $E\left[|H_{b,m,k,q}[n]|^2\right] = 1$, while the mean is $E\left[H_{b,m,k,q}[n]\right] = 0$. The channel gains are also time correlated according to the Jakes fading model (Section 2.1.3). For each MIMO array, it is assumed that the channel gains are identically and independently distributed (i.i.d.).

The system and channel imperfections are modeled as follows. It is assumed that all RF circuitry at both the transmitter and receiver is linear. Any power loss or gain in the signal due to passive RF components, amplifiers, or antennas is subsumed into the channel SNR. The pulse shape $p(t)$ is chosen such that ISI is zero. The local oscillators at each BS and MS suffer from an offset from the assigned carrier frequency f_c, defined as f_b^{BS} and f_k^{MS}, respectively. For the symbol period T_s, the normalized CFO is defined as

$$c_b^{BS} = 2\pi f_b^{BS} T_s \tag{2.19}$$

and

$$c_k^{MS} = 2\pi f_k^{MS} T_s \tag{2.20}$$

in units of radians (rad). This normalized CFO can be viewed as the unwanted phase rotation during one symbol period. The effective MS-side CFO for the b^{th} BS at the k^{th} MS is thus

$$c_{b,k} = c_b^{BS} - c_k^{MS}. \tag{2.21}$$

Further detail on CFO is given in Section 3.1 and 3.2. During the RF stage, the received signal is corrupted by the additive white Gaussian noise (AWGN) signal $z(t)$. The two-sided power spectral density of $z(t)$ is $\Phi_{zz}(f) = N_0$ Watts/Hz. The SNR of the signal from the b^{th} BS observed at the k^{th} MS antenna is represented as $\Gamma_{b,k}$, and includes the contribution from all N_T BS antennas. The symbol SNR is then defined after optimum sampling at the output of a unit energy filter matched to the pulse shape. The SNR $\Gamma_{b,k}$ is expressed as

$$\Gamma_{b,k} = \frac{E_{b,k}}{N_0}, \tag{2.22}$$

where $E_{b,k}$ is the energy received at the k^{th} MS from the b^{th} BS.

In this thesis, the following conventions are used:

- All signals are represented in complex baseband form.
- Bold lowercase variables such as $\mathbf{a}$ represent vectors, and bold uppercase variables such as $\mathbf{A}$ represent matrices.
- When defining a matrix, the scripts $\mathbb{C}^{b\times c}$ and $\mathbb{R}^{b\times c}$ will be used to denote a complex or real matrix with dimensions $b \times c$, respectively.
- The superscript operator $\mathbf{A}^{<i>}$ of a matrix corresponds to the i^{th} column of $\mathbf{A}$.
- The superscript symbols $\cdot^*$ denotes the complex conjugate of a variable, $\cdot^T$ denotes the transpose of a vector or matrix, and $\cdot^\dagger$ denotes the complex conjugate transpose or Hermitian of a vector or matrix.
- The matrix $\mathbf{I}_N \in \mathbb{R}^{N\times N}$ refers to an identity matrix and the vector $\mathbf{1}_B \in \mathbb{R}^{B\times 1}$ refers to an all-ones vector.
- The matrix operators $tr\{\cdot\}$, $blkdiag(\mathbf{A} \ \cdots \ \mathbf{Z})$, $\odot$ and $\otimes$ refer to the trace, block diagonalization, component-wise product and Kronecker product, respectively.
- The overline of a matrix $\overline{\mathbf{A}}$ refers to the Kronecker product with $\mathbf{I}_{N_R}$, that is, $\mathbf{I}_{N_R} \otimes \mathbf{A}$
- The operators $E[\cdot]$ and $\overline{a_n}^n$ refer to the statistical expectation and arithmetic average with respect to index n, respectively.

2.4.1 Data Model

To measure the effect of channel impairments on the capacity efficiency of the CMBMU downlink, the ZF beamformer is used as an example. The signal model defined here is used in Chapter 3 to form an expression for the sum-rate capacity of the ZF beamformer.

For the data frame, the transmitter assumes that the channel is quasi-static, frequency-flat, and that the BSs and MSs are perfectly synchronized. The actual channel may exhibit any of the impairments listed above.

At the n^{th} symbol time, the N_U data bits destined for the k^{th} MS are stored in the vector $\mathbf{b}_k[n] \in \mathbb{C}^{N_U\times 1}$. These symbols are weighted and transmitted from all BN_T BS antennas; the weighted symbol is defined in the vector $\mathbf{s}_k[n] \in \mathbb{C}^{BN_T\times 1}$ as

$$\mathbf{s}_k[n] = \mathbf{W}_k\sqrt{\mathbf{P}_k}\mathbf{b}_k[n], \tag{2.23}$$

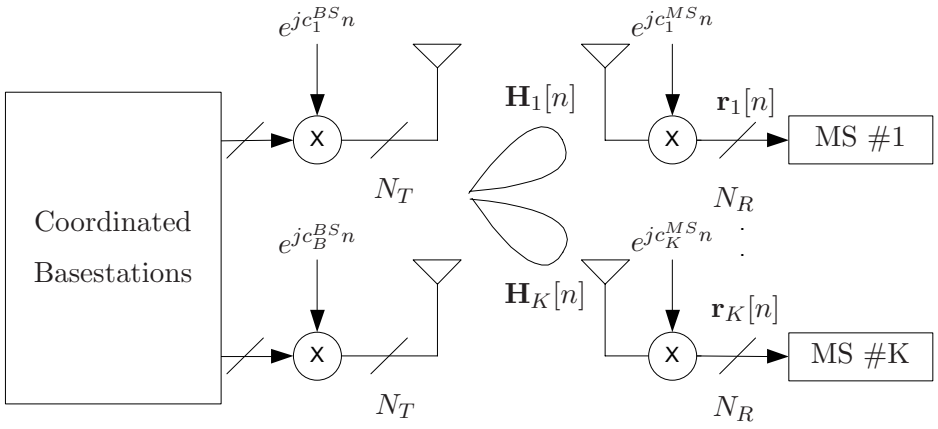

Figure 2.5: Coordinated multibase/multiuser downlink model.

where $\mathbf{W}_k \in \mathbb{C}^{BN_T \times N_U}$ is the unitary matrix that holds the complex transmit weights, $\mathbf{P}_k \in \mathbb{R}^{N_U \times N_U}$ is the diagonal matrix that holds the transmit power for each symbol, and $N_U = BN_T - (K-1)N_R$. With this definition and the assumption that the data bits are independent, we can define the covariance matrix of the transmit symbols to be

$$\mathbf{Y}_k = \mathbf{W}_k \mathbf{P}_k \mathbf{W}_k^{\dagger}. \tag{2.24}$$

We refer to $\mathbf{W}_k$ as the transmit filter, which we will define later. The symbol that is transmitted from all BSs is then defined as

$$\mathbf{s}[n] = \sum_{k=1}^{K} \mathbf{s}_k[n]. \tag{2.25}$$

Since the BSs are transmitting information to all MSs simultaneously, one MS may receive a signal that contains information meant for another MS. As discussed in Section 2.2.2, the ZF transmit filter is designed to prevent this multiuser interference, provided that perfect channel state information is available. At the k^{th} MS, the received signal $\mathbf{r}_k[n] \in \mathbb{C}^{N_R \times 1}$ after matched filtering and symbol rate sampling is found using (2.25) to be

$$\begin{aligned} \mathbf{r}_k[n] &= \mathbf{H}_k[n]\mathbf{D}(\mathbf{c}_k n)\mathbf{s}[n] + \mathbf{z}_k[n] \\ &= \sum_{i=1}^{K} \mathbf{H}_k[n]\mathbf{D}(\mathbf{c}_k n)\mathbf{s}_i[n] + \mathbf{z}_k[n], \end{aligned} \tag{2.26}$$

where

$$\mathbf{H}_k[n] = \begin{bmatrix} \mathbf{h}_{k,1}[n] & \cdots & \mathbf{h}_{k,N_R}[n] \end{bmatrix}^T \in \mathbb{C}^{N_R \times BN_T}$$

$$\begin{aligned}\mathbf{h}_{k,q}[n] &= \left[h_{1,1,k,q}[n] \;\; h_{1,2,k,q}[n] \;\; \cdots \;\; h_{B,N_T,k,q}[n]\right]^T \in \mathbb{C}^{BN_T \times 1} \\ \mathbf{D}\left(\mathbf{c}_k n\right) &= blkdiag\left(e^{jc_{1,k}n}\mathbf{I}_{N_T} \;\; \cdots \;\; e^{jc_{B,k}n}\mathbf{I}_{N_T}\right) \in \mathbb{C}^{BN_T \times BN_T},\end{aligned} \tag{2.27}$$

and $c_{b,k} = c_b^{BS} - c_k^{MS}$. The channel gains are assumed to be quasi-static and known to the BSs. We define $\mathbf{H} = stack\left(\mathbf{H}_1 \;\; \cdots \;\; \mathbf{H}_K\right) \in \mathbb{C}^{KN_R \times BN_T}$ as the complete channel state matrix, and $\mathbf{H}_k^{(-)} \in \mathbb{C}^{(K-1)N_R \times BN_T}$ as $\mathbf{H}$ with all rows from user k removed. The unitary transmit filter $\mathbf{W}_k$ can then be defined as having columns that span the nullspace of $\mathbf{H}_k^{(-)}$.

For the ZF beamformer, the transmit energy allocated to each MS through $\mathbf{P}_k$ is defined in two ways: equal power transmission (EPT) and waterfilling. For EPT, the transmit power allocated to each MS is equal, so that the power allocation matrix $\mathbf{P}_k$ becomes

$$\mathbf{P}_k = (N_0\Gamma_K/T_s)\mathbf{I}_{N_U}, \tag{2.28}$$

where

$$\Gamma_K = \frac{E_K}{N_0} = \frac{E_{BS}}{N_0 K\left(BN_T - (K-1)N_R\right)} \tag{2.29}$$

is the transmit SNR per symbol and N_U denotes the number of available spatial subchannels. If we transmit to the k^{th} MS on all available spatial subchannels, then we can define $N_U = BN_T - (K-1)N_R$, so $\Gamma_K = E_{BS}/KN_UN_0$. The total energy allocated to all BSs E_{BS} is used to maintain a constant transmit energy from each BS to each MS. The sum of the trace of each transmit covariance matrix then reveals the total transmit power, and takes the value

$$\begin{aligned}\sum_k trace(\mathbf{Y}_k) &= \sum_k trace\left(\mathbf{W}_k\mathbf{P}_k\mathbf{W}_k^\dagger\right) \\ &= \frac{KN_0\Gamma_K}{T_s} trace(\mathbf{I}_{N_U}\mathbf{W}_k^\dagger\mathbf{W}_k) \\ &= \frac{KN_UN_0\Gamma_K}{T_s} \\ &= E_{BS}T_s.\end{aligned} \tag{2.30}$$

For waterfilling, the capacity is optimized by allocating the optimum power to each MS given the predetermined maximum energy allocation E_{BS} for all MSs. Since waterfilling is done over the spatial subchannels, $\mathbf{W}_k$ is re-defined as a non-unitary matrix. For example, $\mathbf{W}_k$ could be the pseudo-inverse of $\mathbf{H}_k^{(-)}$. The restriction on the transmit covariance matrix is still the same as for the unitary $\mathbf{W}_k$. The optimum $\mathbf{P} = diag\left(\mathbf{P}_1, \;\; \cdots \;\; , \mathbf{P}_K\right) \in \mathbb{R}^{KN_U \times KN_U}$ is found jointly for all MSs by using the waterfilling algorithm [75], such that (2.30) is satisfied.

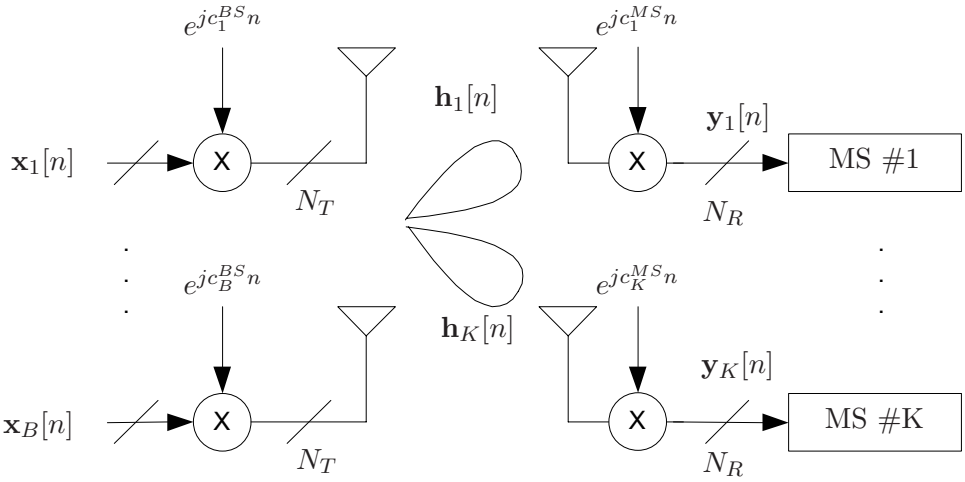

Figure 2.6: Coordinated multibase/multiuser CFO estimate model.

2.4.2 Training Model

The signal model presented in this section introduces the main area of study for this thesis: synchronization in CMBMU systems. Due to the specific structure of the CMBMU system, the way in which channel impairments influence channel estimation are different than in other communication systems. Variants of the signal model defined here are used in Chapters 4 and 6.

Training Sequences

During channel parameter estimation, each BS antenna transmits a different set of N training symbols. Each MS uses the received samples, along with knowledge of each training sequence (TS), to estimate system parameters such as channel impulse response, timing offset, and carrier frequency offset. The TSs used are either orthogonal or quasi-orthogonal, as suggested by [73]. The orthogonal sequences are taken from the set of $N = 2^q$ Hadamard sequences of length-N, where q is an integer. These TSs are of fixed length by design. The quasi-orthogonal TSs are found from a random search, with the constraint that any two TSs cannot have a cross-correlation that exceeds $1/N$.

We refer to the n^{th} training symbol from the m^{th} transmit antenna of the b^{th} BS as $x_{b,m}[n]$. In matrix form, the training symbols form the $N \times BN_T$ matrix $\mathbf{X}$. For the n^{th} symbol time, the N_T symbols transmitted simultaneously from the b^{th} BS is represented as

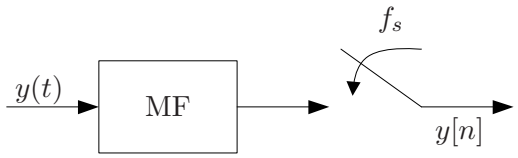

Figure 2.7: Matched filtering at the receiver.

the length-N_T row vector $\mathbf{x}_b[n]$.

Each symbol is pulse-shaped, upconverted with a frequency of $f_c + f_b^{BS}$, transmitted through the mobile fading channel, downconverted with a frequency of $f_c + f_k^{MS}$, and matched filtered. Note that f_b^{BS} and f_k^{MS} are the CFOs defined earlier.

Signal Model

In Chapters 4 and 5, a frequency-flat, static channel model is used to introduce the estimation and correction techniques. For the q^{th} antenna of the k^{th} MS, the channel response is represented by $\mathbf{h}_{k,q} \in \mathbb{C}^{BN_T \times 1}$. After processing by a MF and sampling at the optimum rate $1/T_s$ (Figure 2.7), the received samples are placed in the vector

$$\mathbf{y}_{k,q} = \mathbf{V}(\mathbf{c}_k)\mathbf{h}_{k,q} + \mathbf{z}_{k,q} \in \mathbb{C}^{N \times 1}, \tag{2.31}$$

where $\mathbf{V}(\mathbf{c}_k) \in \mathbb{C}^{N \times BN_T}$ is a CFO rotated version of the TS matrix and $\mathbf{z}_{k,q} \in \mathbb{C}^{N \times 1}$ is the vector of AWGN noise terms. The rotated TS matrix is formed as

$$\mathbf{V}(\mathbf{c}_k) = (\mathbf{X} \odot \mathbf{D}(\mathbf{c}_k)) \sqrt{\mathbf{P}_k}, \tag{2.32}$$

where $\odot$ refers to an element-by-element product,

$$\mathbf{D}(\mathbf{c}_k) = \left[\begin{bmatrix} 1 \\ e^{jc_{1,k}} \\ \vdots \\ e^{jc_{1,k}(N-1)} \end{bmatrix} \otimes \mathbf{1}_{N_T}^T \quad \cdots \quad \begin{bmatrix} 1 \\ e^{jc_{B,k}} \\ \vdots \\ e^{jc_{B,k}(N-1)} \end{bmatrix} \otimes \mathbf{1}_{N_T}^T \right] \in \mathbb{C}^{N \times BN_T}, \tag{2.33}$$

and

$$\mathbf{P}_k = [P_{1,k}\mathbf{I}_{N_T} \quad \cdots \quad P_{B,k}\mathbf{I}_{N_T}] \in \mathbb{R}^{BN_T \times BN_T} \tag{2.34}$$

is a diagonal matrix that holds the symbol transmit powers. The values in $\mathbf{P}_k$ are also used to portray path loss. For example, with a transmit power from the b^{th} BS of $P_{b,k}^{tx}$ and a path loss of $\Gamma_{b,k}^{loss}$, the power received at the k^{th} MS is $P_{b,k} = P_{b,k}^{tx} - N_0\Gamma_{b,k}^{loss}/T_s$.

As there are N_R receive antennas at each MS, the received samples are stacked in $\mathbf{y}_k$

$$\mathbf{y}_k = \overline{\mathbf{V}}(\mathbf{c}_k)\mathbf{h}_k + \mathbf{z}_k \in \mathbb{C}^{NN_R \times 1}, \tag{2.35}$$

where the stacked channel gains are $\mathbf{h}_k = \begin{bmatrix}\mathbf{h}_{k,1}^T & \cdots & \mathbf{h}_{k,N_R}^T\end{bmatrix}^T \in \mathbb{C}^{BN_RN_T \times 1}$, the stacked noise samples are $\mathbf{z}_k = \begin{bmatrix}\mathbf{z}_{k,1}^T & \cdots & \mathbf{z}_{k,N_R}^T\end{bmatrix}^T$, and $\overline{\mathbf{V}}(\mathbf{c}_k) = \mathbf{I}_{N_R} \otimes \mathbf{V}(\mathbf{c}_k)$.

In Chapter 6, the model is further assumed to be time-selective. The model is changed so that the received samples from (2.31) become

$$\mathbf{y}_{k,q} = \mathbf{V}^{(t)}(\mathbf{c}_k)\mathbf{h}_{k,q}^{(t)} + \mathbf{z}_{k,q}, \tag{2.36}$$

where $\cdot^{(t)}$ refers to the 'time-selective' version of the array. The time-selective versions of $\mathbf{V}(\mathbf{c}_k)$, $\mathbf{P}$ and $\mathbf{h}_{k,q}$ are defined as

$$\begin{aligned}
\mathbf{V}^{(t)}(\mathbf{c}_k) &= \mathbf{D}^{(t)}(\mathbf{c}_k)\mathbf{X}^{(t)}\sqrt{\mathbf{P}_k^{(t)}} \in \mathbb{C}^{N \times BNN_T} \\
\mathbf{P}_k^{(t)} &= blkdiag\left(P_{1,k}\mathbf{I}_{NN_T} \;\cdots\; P_{B,k}\mathbf{I}_{NN_T}\right) \in \mathbb{R}^{BNN_T \times BNN_T} \\
\mathbf{h}_{k,q}^{(t)} &= \left[h_{1,1,k,q}[1] \;\cdots\; h_{1,1,k,q}[N] \;\; h_{1,2,k,q}[1] \;\cdots\; h_{B,N_T,k,q}[N]\right]^T \in \mathbb{C}^{BNN_T \times 1}
\end{aligned} \tag{2.37}$$

where

$$\begin{aligned}
\mathbf{D}^{(t)}(\mathbf{c}_k) &= \left[\mathbf{1}_{N_T}^T \otimes \mathbf{D}_1^{(t)}(c_{1,k}) \;\cdots\; \mathbf{1}_{N_T}^T \otimes \mathbf{D}_B^{(t)}(c_{B,k})\right] \in \mathbb{C}^{N \times BNN_T} \\
\mathbf{D}_b^{(t)}(c_{b,k}) &= diag\left(1 \;\; e^{jc_{b,k}} \;\cdots\; e^{jc_{b,k}(N-1)}\right) \in \mathbb{C}^{N \times N} \\
\mathbf{X}^{(t)} &= blkdiag\left(\mathbf{X}_{1,1}^{(t)} \;\; \mathbf{X}_{1,2}^{(t)} \;\cdots\; \mathbf{X}_{B,N_T}^{(t)}\right) \in \mathbb{C}^{BNN_T \times BNN_T} \\
\mathbf{X}_{b,m}^{(t)} &= diag\left(x_{b,m}[1] \;\cdots\; x_{b,m}[N]\right) \in \mathbb{C}^{N \times N},
\end{aligned} \tag{2.38}$$

and $\mathbf{1}_{N_T}$ is a length-N_T vector of all 1's.

Asynchronicity and Frequency Selectivity

In Chapter 4, the training model is extended to account for frequency selectivity. To begin with, the model is modified to account for an $L+1$ tap frequency-selective channel. The signal portion is represented as a linear combination of time-shifted arrays of the frequency-shifted signals. Symbol-spaced ISI is inherently included in this model.

To further include arbitrary tap spacing and arrival times that are not an integer multiple of T_s, oversampling by a factor of N_{ss} can be accommodated by using appropriately shifted

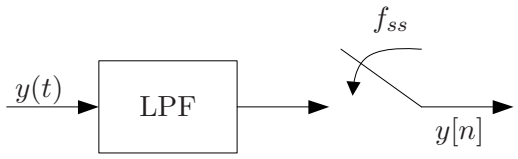

Figure 2.8: Oversampling at the receiver.

pulse waveforms. To this end, the initial MF sampling procedure is altered as depicted in Figure 2.8. At each receive antenna, the signal is first sent through a lowpass filter, with a bandwidth $W_{LO} > W$. Samples are taken at the Nyquist rate of $f_{ss} = 2W_{LO}$, with the n^{th} sample stored in $y[n]$; f_{samp} is chosen so that the sampled noise $z[n]$ is independent from sample to sample. The samples in the new $y[n]$ are spaced apart by $T_{ss} = T_s/N_{ss} = 1/f_{ss}$, where T_s is the symbol rate, and $N_{ss} = f_{ss}T_s$. To guarantee optimality for any pulse shape $p(t)$, it can be incorporated into the matrix $\mathbf{V}(\mathbf{c})$. The n^{th} training symbol from the m^{th} antenna of the b^{th} BS can be re-defined as

$$x_{b,m}^{(ss)}[n] = \sum_{i=-T_f}^{T_b} x_{b,m}[n-i]p\left((n-i)\,T_{ss}\right), \tag{2.39}$$

where T_f and T_b define the domain of the pulse shape in oversamples.

For the k^{th} MS, $NN_{ss} + L$ samples of the received training signal are taken at the q^{th} antenna and stored in $\mathbf{y}_{k,q}^{(ss)}$, where

$$\mathbf{y}_{k,q}^{(ss)} = \mathbf{V}^{(ss)}(\mathbf{c}_k)\mathbf{h}_{k,q}^{(ss)} + \mathbf{z}_{k,q}^{(ss)} \in \mathbb{C}^{(NN_{ss}+L)\times 1}, \tag{2.40}$$

and $\cdot^{(ss)}$ refers to the oversampled version of the array. The rotated TS matrix becomes

$$\begin{aligned}
\mathbf{V}^{(ss)}(\mathbf{c}_k) &= \left[\mathbf{V}^{(ss,0)}(\mathbf{c}_k) \;\cdots\; \mathbf{V}^{(ss,L)}(\mathbf{c}_k)\right] \in \mathbb{C}^{(NN_{ss}+L)\times B(L+1)NN_{ss}N_T} \\
\mathbf{V}^{(ss,l)}(\mathbf{c}_k) &= \left[\mathbf{0}_{BN_T\times l} \;\; \mathbf{U}^{(ss)T}(\mathbf{c}_k, l) \;\; \mathbf{0}_{BN_T\times(L-l)}\right]^T \in \mathbb{C}^{(NN_{ss}+L)\times BNN_{ss}N_T} \\
\mathbf{U}^{(ss)}(\mathbf{c}_k, l) &= \mathbf{D}^{(ss)}(\mathbf{c}_k)\mathbf{X}^{(ss)}\sqrt{\mathbf{P}_{k,l}^{(ss)}} \in \mathbb{C}^{NN_{ss}\times BNN_{ss}N_T}.
\end{aligned} \tag{2.41}$$

The oversampled CFO matrix $\mathbf{D}^{(ss)}(\mathbf{c}_k) \in \mathbb{C}^{NN_{ss}\times BNN_{ss}N_T}$ is defined as

$$\begin{aligned}
\mathbf{D}^{(ss)}(\mathbf{c}_k) &= \left[\mathbf{D}^{(ss)}(c_{1,k}) \;\cdots\; \mathbf{D}^{(ss)}(c_{1,k}) \;\; \mathbf{D}^{(ss)}(c_{2,k}) \;\cdots\; \mathbf{D}^{(ss)}(c_{B,k})\right] \\
\mathbf{D}^{(ss)}(c_{b,k}) &= diag\left(1 \;\; e^{jc_{b,k}\frac{1}{N_{ss}}} \;\cdots\; e^{jc_{b,k}\frac{NN_{ss}-1}{N_{ss}}}\right) \in \mathbb{C}^{NN_{ss}\times NN_{ss}},
\end{aligned} \tag{2.42}$$

while the oversampled TS matrix $\mathbf{X}^{(ss)}$ is

$$\begin{aligned}\mathbf{X}^{(ss)} &= blkdiag\left(\mathbf{X}_{1,1}^{(ss)} \;\; \mathbf{X}_{1,2}^{(ss)} \;\; \cdots \;\; \mathbf{X}_{B,N_T}^{(ss)}\right) \in \mathbb{C}^{BNN_{ss}N_T \times BNN_{ss}N_T} \\ \mathbf{X}_{b,m}^{(ss)} &= diag\left(x_{b,m}^{(ss)}[1] \;\; x_{b,m}^{(ss)}[1] \;\; \cdots \;\; x_{b,m}^{(ss)}[N]\right) \in \mathbb{C}^{NN_{ss} \times NN_{ss}}. \end{aligned} \tag{2.43}$$

The power of the l^{th} tap to the k^{th} MS is defined in the diagonal oversampled $\mathbf{P}_{k,l}^{(ss)}$ matrix,

$$\mathbf{P}_{k,l}^{(ss)} = blkdiag\left(P_{1,k,l}\mathbf{I}_{NN_{ss}N_T} \;\; \cdots \;\; P_{B,k,l}\mathbf{I}_{NN_{ss}N_T}\right) \in \mathbb{R}^{BNN_{ss}N_T \times BNN_{ss}N_T}. \tag{2.44}$$

Lastly, the channel gain vector $\mathbf{h}_{k,q}^{(ss)}$ is defined as

$$\begin{aligned}\mathbf{h}_{k,q}^{(ss)} &= \left[\mathbf{h}_{k,q}^{(ss,0)T} \;\; \cdots \;\; \mathbf{h}_{k,q}^{(ss,L)T}\right] \in \mathbb{C}^{B(L+1)NN_{ss}N_T \times 1} \\ \mathbf{h}_{k,q}^{(ss,l)} &= \left[\mathbf{h}_{1,1,k,q}^{(ss,l)T} \;\; \mathbf{h}_{1,2,k,q}^{(ss,l)T} \;\; \mathbf{h}_{B,N_T,k,q}^{(ss,l)T}\right]^T \in \mathbb{C}^{BNN_{ss}N_T \times 1} \\ \mathbf{h}_{b,m,k,q}^{(ss,l)} &= \left[h_{b,m,k,q}^{(l)}[1] \;\; \cdots \;\; h_{b,m,k,q}^{(l)}[NN_{ss}]\right]^T \in \mathbb{C}^{NN_{ss} \times 1}. \end{aligned} \tag{2.45}$$

Again, for conciseness, the $\mathbf{y}_k^{(ss)}$ vector is used to represent the concatenation of the N_R $\mathbf{y}_{k,q}^{(ss)}$ vectors. The vector $\mathbf{y}_k^{(ss)}$ is then

$$\begin{aligned}\mathbf{y}_k^{(ss)} &= \overline{\mathbf{V}}^{(ss)}(\mathbf{c})\mathbf{h}_k^{(ss)} + \mathbf{z}_k^{(ss)} \in \mathbb{C}^{(NN_{ss}+L)N_R \times 1} \\ &= \left[\mathbf{y}_{k,1}^{(ss)T} \;\; \cdots \;\; \mathbf{y}_{k,N_R}^{(ss)T}\right]^T \\ \mathbf{h}_k^{(ss)} &= \left[\mathbf{h}_{k,1}^{(ss)T} \;\; \cdots \;\; \mathbf{h}_{k,N_R}^{(ss)T}\right]^T \in \mathbb{C}^{B(L+1)NN_RN_{ss}N_T \times 1} \\ \mathbf{z}_k^{(ss)} &= \left[\mathbf{z}_{k,1}^{(ss)T} \;\; \cdots \;\; \mathbf{z}_{k,N_R}^{(ss)T}\right]^T \in \mathbb{C}^{(NN_{ss}+L)N_R \times 1}. \end{aligned} \tag{2.46}$$

2.4.3 Feedback Model

In Chapter 5, the CFO estimates made at the MSs are fed back to the coordinated BSs. The MS-side estimates are used by both the BSs and MSs to reduce the CFO spread. This model, shown in Figure 2.9, summarizes the signals that are used in multibase and multiuser CFO estimation and correction.

To prevent confusion between the CFOs and their estimates, we will use the following convention: the terms "BS CFO estimate" and "MS CFO estimate" refer to estimates of the BS and MS CFOs c_b^{BS} and c_k^{MS}, where $\hat{\mathbf{c}}^{BS}$ and $\hat{\mathbf{c}}^{MS}$ are vectors with components $\hat{c}_b^{BS}$ and $\hat{c}_k^{MS}$, respectively. The term MS-side CFO estimate (MCE) refers to the initial estimate

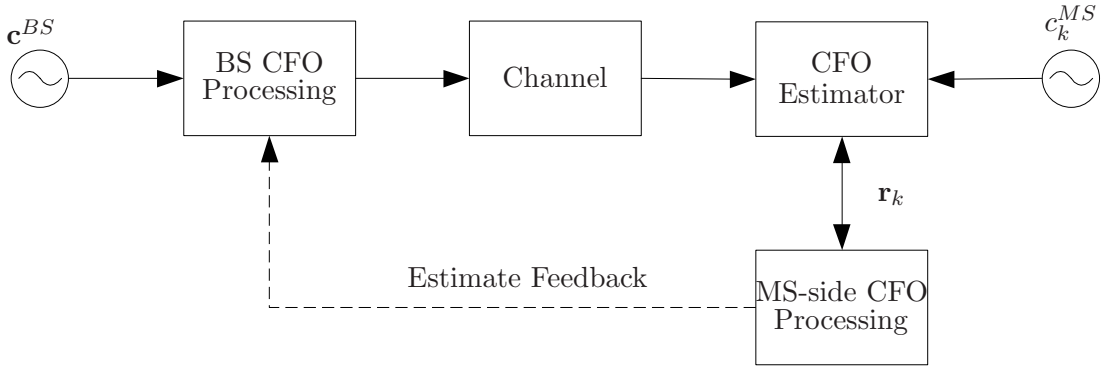

Figure 2.9: CFO feedback model for the k^{th} MS.

made at the MS of the apparent BS CFO prior to any separation into BS and MS CFO contributions; this is the CFO estimate $\hat{c}_{b,k}$ made in Chapter 4. The vector

$$\mathbf{r}_k = [\hat{c}_{1,k} \quad \cdots \quad \hat{c}_{B,k}]^T \in \mathbb{R}^{B\times 1} \tag{2.47}$$

in Chapter 5 is comprised of the k^{th} MSs MS-side CFO estimates.

Chapter 3

Obstacles for CMBMU Systems

In communication system research, engineers routinely make assumptions that neglect channel impairments in order to simplify the MCS model. These assumptions allow the engineer to ignore certain real-world challenges that might otherwise stifle innovation. However, in order to understand if and how a technology can be implemented in a real-world system, these impairments must be accounted for. This is the motivation behind our analysis of the coordinated multibase/multiuser MCS in the presence of channel impairments.

Since CFO has been identified as a particular problem in CMBMU systems, it forms the main focus of this chapter. In Sections 3.1 and 3.2, LO-induced CFO and Doppler-induced CFO are treated, respectively. The effects of time selectivity will be examined in Section 3.3. Results are presented in Section 3.4, with a chapter summary presented in Section 3.5. The work presented in this chapter provides motivation for further investigation into compensation and correction for channel impairments in CMBMU systems.

3.1 Carrier Frequency Offset Due to Independent Local Oscillators

Each transceiver in a communication system includes an independent local oscillator (LO) which is used to convert the baseband signal to and from the desired carrier frequency f_c. Synchronization of the carrier frequency among all radios in the communication system is necessary to prevent large phase errors [57]. In the downlink of a CMBMU system, these phase errors would lead to beamformers that are improperly matched to the channel state,

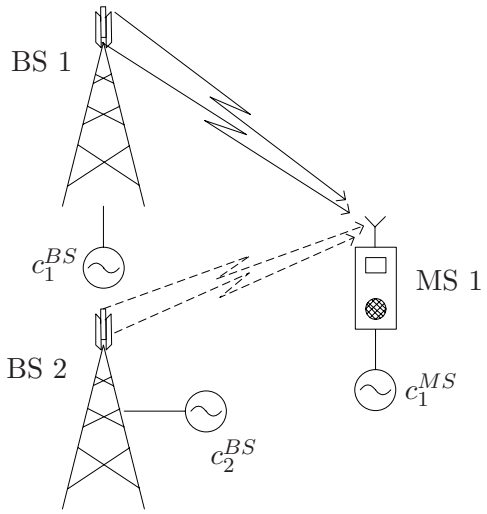

Figure 3.1: LO-induced CFO model. Each oscillator block refers to the carrier frequency offset at a specific BS or MS.

resulting in a decrease of beamformer gain to desired MSs and an increase in undesired interference. Due to impairments or irregularities in the LO crystal or the tuning circuit, the carrier frequency as witnessed by the receiver is offset from the nominal f_c by an initially unknown amount: this is referred to as LO-induced CFO. For the purposes of this work, we neglect any LO phase drift other than that associated with frequency offset.

3.1.1 LO-induced CFO

In the CMBMU systems considered in this thesis, multiple CFOs result from the multiple independent LOs at each BS and MS. Figure 3.1 depicts a system with two BSs and one MS, with the normalized CFOs (detailed in the following Section 3.1.2) labeled as c_1^{BS}, c_2^{BS}, and c_1^{MS}. For CFO resulting from LO offset, manufacturers report a deviation in the form of a maximum limit [18]. The magnitude of the LO CFO is referred to as ϵ_0 in units of parts per million (ppm). This offset is assumed to remain constant once the LO is operational, with long term variations due to aging and changes in temperature. While phase noise will cause short term carrier frequency variation, it is not considered in this model; it is assumed that, over the time scale of interest, the dynamic variation of the CFO will average to the static offset.

The LO manufacturers report the offset deviation as a function of temperature and aging. Croven crystals [18] report a maximum CFO as low as $\epsilon_0 = 1.5$ ppm, with aging contributions in the parts per billion per year. For BSs, a maximum CFO of $\epsilon_0 = 1.5$ ppm for analog systems, and $\epsilon_0 = 0.05$ ppm for CDMA systems is considered the standard [50]. The LO-induced normalized CFO c_{max} is defined as

$$c_{max} = 2\pi f_c \epsilon_0 T_s. \tag{3.1}$$

The result of CFO caused by LO offset is a progressive rotation of the received signal. Physically, this rotation can be thought of as a rotation of the channel state. Over time, this rotation can cause significant increase to bit error rate (BER), especially for higher order constellations; the rotation can cause incorrect detection of constellation symbols by moving the decision boundaries relative to the symbol.

3.1.2 Effects on Sum-Rate Capacity

In this section, the effect of CFO on the sum-rate capacity of a zero-forcing beamformer is investigated. In the following, analysis on the effects of multiple CFOs is done by parameterizing the capacity expression. The capacity will be found as a function of the channel state and the CFO. As the capacity is independent of modulation technique or symbol constellation, it provides a good overall view of the effects of CFO on the sum-rate capacity of a CMBMU system.

As opposed to using a more accurate measurement of throughput that includes the discrete effects of modulation and coding, the work presented here uses the more tractable theoretical expression for capacity assuming Gaussian channel inputs.

The system model used for this chapter is presented in Section 2.4.1. Specifically, it denotes the set of received samples $\mathbf{r}_k[n]$ for the n^{th} symbol time at the k^{th} MS as

$$\mathbf{r}_k[n] = \sum_{i=1}^{K} \mathbf{H}_k[n]\mathbf{D}(\mathbf{c}_k n)\mathbf{s}_i[n] + \mathbf{z}_k[n], \tag{3.2}$$

where $\mathbf{H}_k[n]$ is the channel gain matrix, $\mathbf{D}(\mathbf{c}_k n)$ is the rotation matrix based on the CFOs of the system, $\mathbf{s}_i[n]$ is the vector of transmitted symbols from all antennas destined for the i^{th} MS, and $\mathbf{z}_k[n]$ is the receiver noise.

To begin, the normalized CFO $c_{b,k} = c_b^{BS} - c_k^{MS}$ is used from Section 2.4. The normalized CFO can be interpreted as inducing a phase offset (PO) $p_{b,k}$ that is time accumulative.

That is, by symbol time n, we have $p_{b,k} = c_{b,k}n$. The POs degrade the ZF beamformer by weakening the signal strength and by reducing the depth of nulls, thereby increasing interference. The vector $\mathbf{p}_k = \mathbf{c}_k n \in \mathcal{R}^{B\times 1}$ contains the PO values for the BSs, so we can redefine the CFO matrix $\mathbf{D}(\mathbf{c}_k n)$ from (2.26) as $\mathbf{D}(\mathbf{p}_k)$.

Some investigation has been done into the capacity of the downlink of a ZF system in [87]. By using (2.14), an expression for the capacity of each user can be derived as

$$C\left(\mathbf{H}, \tilde{\mathbf{H}}\right) = \sum_{k=1}^{K} \log_2 \left| \mathbf{I}_{N_R} + \tilde{\mathbf{H}}_k \mathbf{Y}_k \tilde{\mathbf{H}}_k^{\dagger} \left(\sum_{i\neq k}^{K} \tilde{\mathbf{H}}_k \mathbf{Y}_i \tilde{\mathbf{H}}_k^{\dagger} + \mathbf{I}_{N_R} \right)^{-1} \right|, \tag{3.3}$$

where $\mathbf{Y}_k$ is the covariance of the transmitted signal from Section 2.4.1 and

$$\tilde{\mathbf{H}}_k = \mathbf{H}_k \mathbf{D}(\mathbf{p}_k) \tag{3.4}$$

is a CFO rotated version of the channel gain matrix. Ideally, the zero-forcing interference product located within the $(\cdot)^{-1}$ of (3.3) is

$$\mathbf{H}_k \mathbf{Y}_i \mathbf{H}_k^{\dagger} = \mathbf{0} \;\; \forall k \neq i, \tag{3.5}$$

and the capacity collapses to

$$C\left(\mathbf{H}, \mathbf{H}\right) = \sum_{k=1}^{K} \log_2 \left| \mathbf{H}_k \mathbf{Y}_k \mathbf{H}_k^{\dagger} + \mathbf{I}_{N_R} \right|. \tag{3.6}$$

However, because of the CFO rotation of the channel gains, this is no longer true.

3.2 Carrier Frequency Offset Due to Doppler Shift

This section examines Doppler-induced CFO, for the special case of a single scatterer and no line of sight path between BSs and MSs. Although this model is limited in scope, it provides a look at alternative sources of CFO. Additionally, this section provides a comparison of Doppler CFO to LO CFO. The results suggest that for a CMBMU system, where mobile speeds are generally assumed to be low, the Doppler CFO is much smaller in magnitude and can therefore be ignored.

3.2.1 Doppler-induced CFO

Another source for CFO in a CMBMU system is that of Doppler shift. In Figure 3.2, a model consisting of two BSs, one MS, and a cluster of scatterers is shown. The CFO c_1^{DOP}

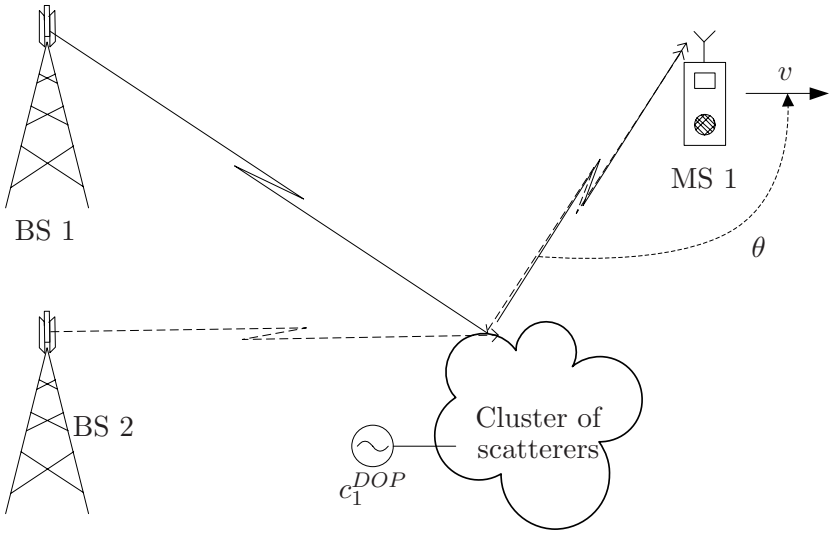

Figure 3.2: LO-induced CFO model. Each oscillator block refers to the carrier frequency offset at a specific BS or MS.

is attached to the cluster of scatterers, which results from the relative motion between the scatterers and the MS. As detailed for the mobile channel in Section 2.1.2 and [1, 6, 13], the Doppler effect causes a frequency shift on the impinging signal, and can be interpreted as a CFO. As opposed to [1, 6], this model does not consider a separate CFO for each antenna to antenna channel. The scatterer will incur a Doppler frequency shift

$$f = \frac{v}{\lambda} cos(\theta) = f_d cos(\theta), \tag{3.7}$$

where v is the relative velocity between the scatterer and the MS in m/s and λ is the wavelength of the carrier frequency f_c in Hz. θ is the angle of arrival of the reflected signal in rad, with 0 being the direction of travel for the mobile [12]. For example, a communications system will exhibit the minimal Doppler contribution to the CFO if all received signals impinge on the receive antenna perpendicular to the direction of motion. Note that if the scatterer is mobile, than there exists a different CFO for each BS signal. The model presented here considers a static scatterer and a mobile MS.

The above model is fairly limited in scope, as it assumes only a single scatterer and no line of sight component. However, because of the model's simplicity, it is used in the following section to compare Doppler CFO to LO CFO.

3.2.2 LO versus Doppler CFO

In this section, it is proposed that Doppler CFO can be disregarded in the presence of LO CFO, since CMBMU systems target users that have low or nomadic mobility (due to the initial set-up time for the beamformers). The consequence of disregarding Doppler CFO is that a simplified model can be used; instead of combining the two models in Figure 3.1, only the LO model is used.

To further illustrate the rationale behind disregarding the Doppler CFO, the ratio R is first defined to compare the severity of the two CFOs,

$$R = \frac{f_{cfo}}{f_d} = \frac{3 \times 10^8 \epsilon_0}{v}, \tag{3.8}$$

where $f_{cfo} = f_c \epsilon_0$ is the effective LO frequency offset, f_d is found from (3.7), and v is in units of m/s. Although this ratio is not a definitive criterion for a realistic mobile fading channel, it provides a reasonable approximation for a small number of BSs and scatterers, and where there is no line of sight between the BSs and the MS; in Section 3.3, the capacity comparison takes a more general fading model into account. Comparing a system containing LOs with an accuracy of $\epsilon_0 = 1$ ppm to a system with Doppler resulting from a relative velocity of 50 km/h (or $v = 13.\overline{8}$ m/s), the ratio is $R = 21.6$. In other words, the effect of the LO CFO is more than 20 times greater than the Doppler CFO. Alternatively, to achieve the same magnitude CFO of Doppler shift with the LO would require a LO with $\epsilon_0 = 0.05$ ppm. Note that this comparison is independent of carrier frequency. From the perspective of the best performing LO with $\epsilon_0 = 0.05$ ppm [50], this means the only time the Doppler CFO effect will surpass the LO CFO effect is when $v > 13.\overline{8}$ m/s; given that the CMBMU will operate in low or nomadic mobility situations, this is unlikely to happen.

The next section considers the case where there are multiple scatterers in the mobile channel. The capacity effects of the resulting time-selective channel are examined. In light of the evidence presented above that Doppler CFO can be ignored in the presence of LO CFO, it is assumed that a similar result will be found for time-selective channels.

3.3 Time-selective Fading Channel

In Section 3.2, the effect of Doppler CFO resulting from a single scatterer is presented. In the presence of multiple scatterers, the single Doppler CFO model must be modified to consider multiple CFOs. Further, these CFOs will also be time variable if changes in θ are

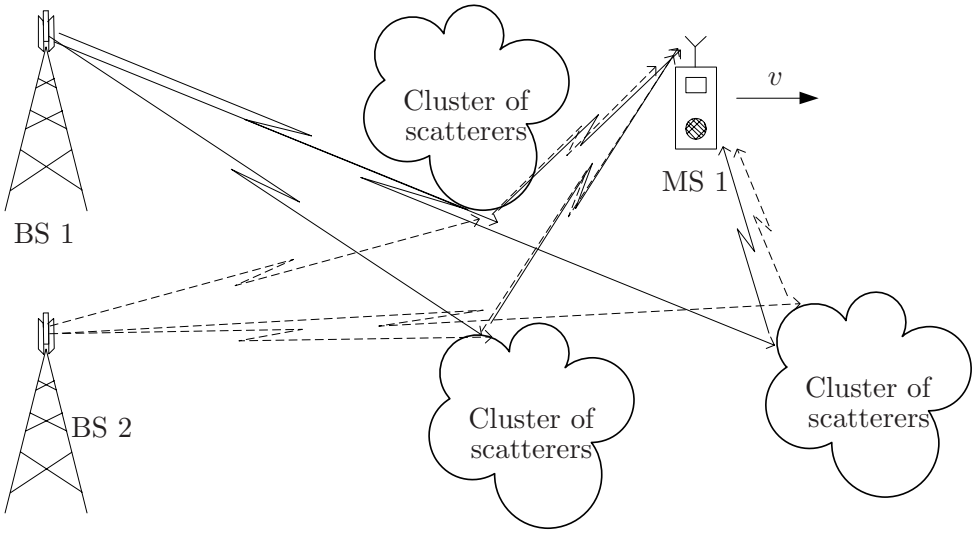

Figure 3.3: Time selective model. There are sufficient incoming multipath from the scatterers to consider the arriving plane waves as Gaussian.

considered as a result of mobility. Instead of analyzing this inherently complex system, a more straightforward and simple model is used. That is, if there are sufficient scatterers, the incoming plane waves can be approximated as Gaussian distributed. Then, if the distribution of power in the plane waves is uniform around the MS, the Jakes model from Section 2.1.3 can be used, with the Bessel function autocorrelation in (2.13). Thus, the Doppler CFOs are replaced with a time-selective channel. As a result, the CFO matrix in (2.26) becomes $\mathbf{D} = \mathbf{I}_{BN_T}$.

3.3.1 Time Selectivity

As detailed in Section 2.1.3, time-selective channels result from the relative speed between MSs and scatterers. In fact, even if there are just two scatterers, the system will exhibit both amplitude and phase changes over time, and not the simple Doppler shift presented by the model in Section 3.2. Figure 3.3 shows the time-selective channel model, in the absence of a line of sight path.

The effects of time selectivity on channel estimates are well documented. The correlation between the current channel gain estimate and the actual channel gain drops in the oscillating manner predicted by the Jakes model in (2.13). As a result, the capacity of a ZF

beamformer drops, since the actual channel gains will not match the older gain estimates used to calculate the beamformer weights. To model time selectivity for capacity analysis, the channel gain matrix $\tilde{\mathbf{H}}_k$ from (3.4) can be rewritten as

$$\tilde{\mathbf{H}}_{k,d} = \rho[n]\mathbf{H}_k + \sqrt{1-\rho^2[n]}\boldsymbol{\Upsilon}_k, \tag{3.9}$$

where $\rho[n] = J_0\left(2\pi n f_d T_s\right)$ and $\boldsymbol{\Upsilon}_k \in \mathcal{C}^{BN_T \times N_R}$ contains complex Gaussian random variables with zero mean and unit variance. This time-selective model depicts the channel gain for symbol n as being correlated with the channel gain for symbol 0 with the correlation coefficient $\rho[n]$.

3.3.2 Effects on Sum-Rate Capacity

To measure the effect that a time selective channel has on the CMBMU sum-rate capacity, the loss in capacity due to channel gain mismatch is quantified. The mismatch occurs due to the quasi-static channel assumption made for beamforming transmission; that is, the channel is assumed to be static after initial channel gain estimation. It is assumed that the transmit weights used at the BSs are calculated using $\mathbf{H}$, and that the actual channel conditions are depicted in $\tilde{\mathbf{H}}_d$. The expression for the CFO-induced capacity loss in (3.3) is rewritten as

$$C\left(\mathbf{H}, \tilde{\mathbf{H}}_d\right) = \sum_{k=1}^{K} \log_2 \left| \mathbf{I}_{N_R} + \tilde{\mathbf{H}}_{k,d}\mathbf{Y}_k\tilde{\mathbf{H}}_{k,d}^{\dagger} \left(\sum_{i \neq k}^{K} \tilde{\mathbf{H}}_{k,d}\mathbf{Y}_i\tilde{\mathbf{H}}_{k,d}^{\dagger} + \mathbf{I}_{N_R} \right)^{-1} \right|. \tag{3.10}$$

This expression is similar to that for CFO, in that the time variation of the channel gains causes degradation in the sum-rate capacity.

3.4 Numerical Results

To find the average capacity of a CMBMU ZF system in the presence of LO CFO, the average of the sum-rate capacity expression in (3.3) was taken over $\mathbf{H}$ and $\mathbf{p}$ using 10^4 Monte Carlo realizations. The channel gain matrix components were set to zero mean, unit variance, complex Gaussian random variables. A maximum PO p_{max} was used to determine the effect of absolute phase offset on the sum-rate capacity. We used this on (3.3), setting

$$\mathbf{D}(\mathbf{p}_k) = blkdiag\left(e^{jp_{max}\theta_{1,k}}\mathbf{I}_{N_T} \quad \cdots \quad e^{jp_{max}\theta_{B,k}}\mathbf{I}_{N_T} \right), \tag{3.11}$$

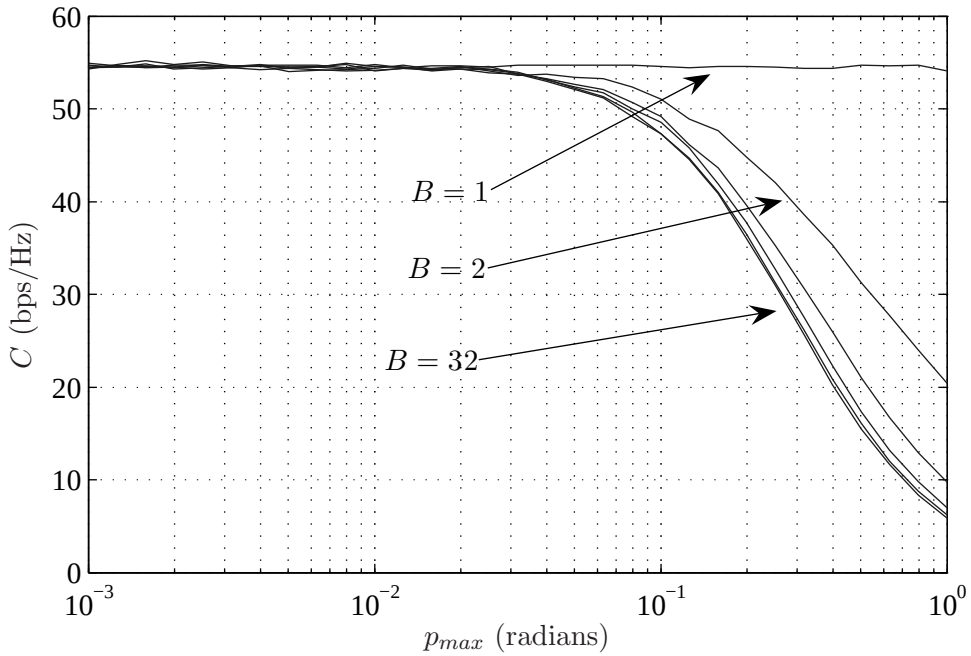

Figure 3.4: Effect of CFO on average sum-rate capacity, using ZF beamformer with EPT; $\Gamma_{BS} = 20$ dB, $B = 1, 2, 4, 8, 16, 32$, $K = 32$, $N_R = 1$, $BN_T = 32$.

where θ_b is a uniform random variable with a range of $[-1, +1]$. Note that p_{max} could be replaced with $c_{max}n$ if parameterization on symbol time nT_s were desired.

Figure 3.4 shows the effect of CFO on average capacity for a total system transmit SNR of $\Gamma_{BS} = E_{BS}/N_0 = 20$dB and equal power transmission; the power is divided using EPT. The fixed system parameters are $K = 32$ and $N_R = 1$. For all curves, the degrees of freedom $BN_T - (K-1)N_R = 1$, so we have the ZF system with one stream per user (i.e., unit rank gain matrices $\mathbf{H}_k$). The total number of transmit antennas BN_T was kept constant at 32, so the curves demonstrate the effect of independent LOs as the number of BSs, B, varies. The capacity drops as B increases. This demonstrates the effect of the random PO. The loss of capacity as the PO increases can be viewed as the cumulative effect of the CFO over time. Given an initially accurate channel estimate, which subsumes the CFO phase error at the moment of the estimate, the orthogonality between the transmitted streams degrades as time increases. For example, for the $B = 32$ system, the capacity drops by about 10% when the PO is 0.1 radians. For a 500 symbol frame, $f_c = 2.4$ Gigahertz (GHz) and $T_s = 1\mu$s, this means a maximum allowable CFO of 0.013 ppm. For many communication systems, this is

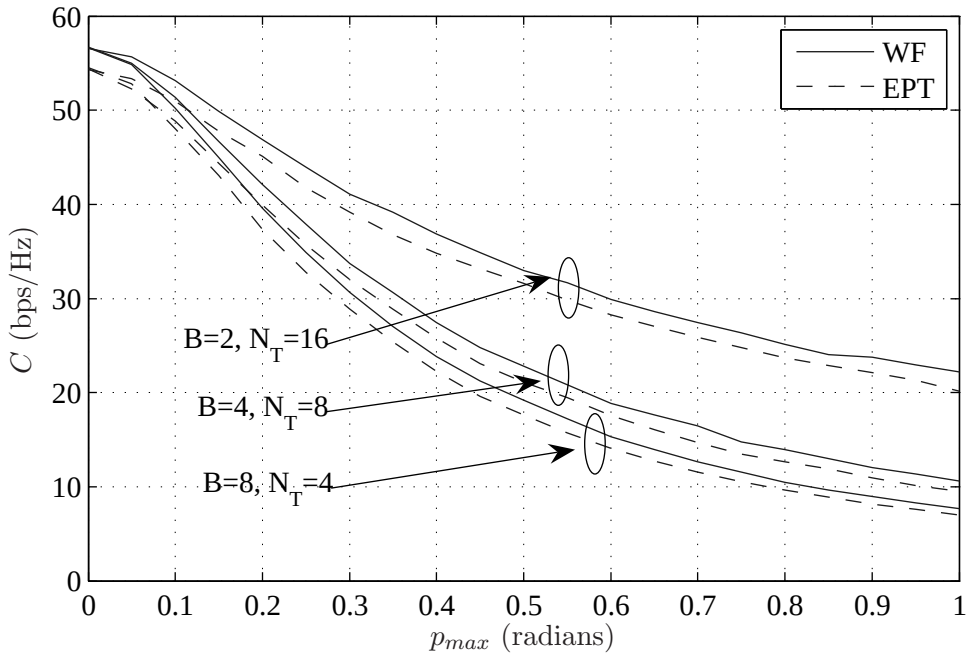

Figure 3.5: Effect of CFO on average sum-rate capacity, using ZF beamformer with EPT and WF; $\Gamma_{BS} = 20$ dB, $B = 2, 4, 8$, $K = 32$, $N_R = 1$, $BN_T = 32$.

an optimistic value, and is probably only feasible for expensive BS LOs. Additionally, we can use the value of 0.1 radians as a benchmark or threshold for determining the onset of capacity degradation. Also, if we were to include the CSI feedback delay, the system would start at a slightly reduced capacity level before transmitting even a single data bit.

Using similar values for K, B and N_T as in Figure 3.4, the capacity is compared over p_{max} with a linear scale to compare the effect of power allocation. This is done for EPT and WF in Figure 3.5. Both exhibit similar degradations with respect to p_{max}, making it clear that different power allocation schemes are effected by CFO to the same degree.

Figure 3.6 shows the range of the capacity in the presence of CFO by plotting the complementary cumulative distribution function (ccdf). The maximum PO is set to $p_{max} =$ 0.01, 0.05 0.1 and 0.5 radians, which are equivalent to rotation of the constellation by 0.16%, 0.80%, 1.59% and 7.96% of a unit circle, respectively, in every symbol time. Of particular interest in this figure is the degradation of the ccdf near $p_{max} = 0.1$, which is the PO previously identified as the point where capacity degradation is limited to less than 10%. At this point, $Pr\left(C > 50 | p_{max} = 0.1\right) \approx 0.5$. This is only a minor change compared

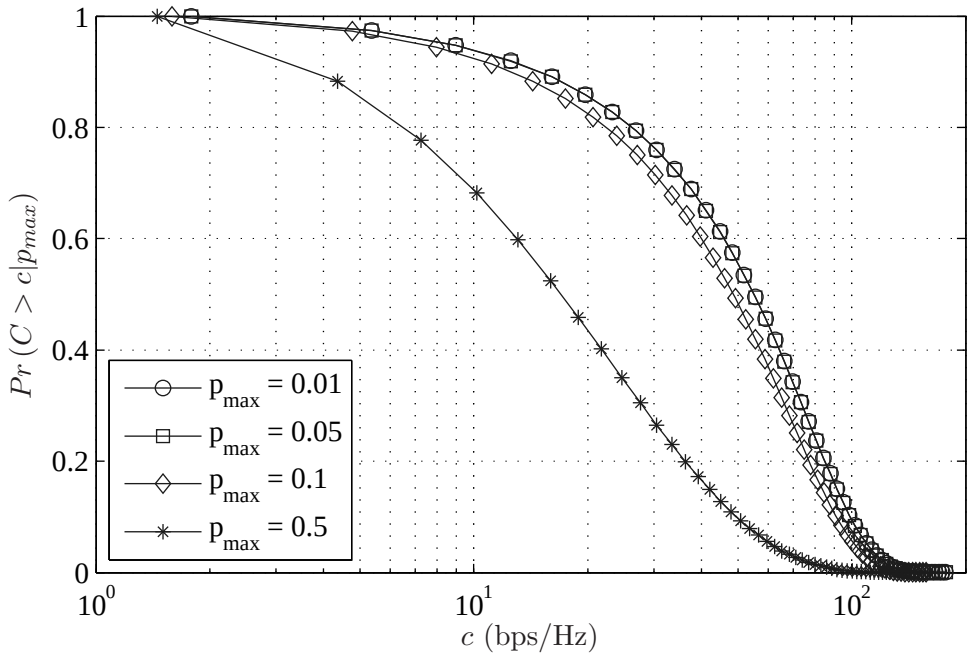

Figure 3.6: Effect of CFO on sum-rate capacity ccdf, using ZF beamformer with EPT; $\Gamma_{BS} = 35$ dB, $B = 4$, $K = 32$, $N_R = 1$, $N_T = 8$.

to $Pr\,(C > 50|p_{max} = 0.01)$. However, with $p_{max} = 0.5$, the $Pr\,(C > 50|p_{max} = 0.5) \approx 0.1$. Along with the visible collapse of the ccdf in Figure 3.4, these results are consistent with the results seen in Figure 3.4.

Simulations were also run to compare the capacity degradation caused by CFO to that caused by time selectivity. Monte Carlo simulations were run using the sum-rate capacity expression in (3.10). Figure 3.7 compares the effect of a time varying channel to that of LO-induced CFO on the sum-rate CMBMU capacity by presenting capacity loss as a function of time. The total transmit SNR is set to $\Gamma_{BS} = 20$ dB and EPT is used. The fixed system parameters are $B = 4$, $K = 32$, $N_R = 1$, and $N_T = 8$. For the variable channel resulting from a high vehicular velocity of 100 km/h (or $v = 27.\overline{7}$ m/s), the capacity degradation is slightly more than that of the moderate LO CFO of $\epsilon_0 = 1$ ppm. For these values of v and ϵ_0, the ratio R in Section 3.2.2 is $R = 10.8$. Thus, it could be roughly interpreted that a time-selective channel with numerous scatterers has approximately 10 times the impact on the sum-rate capacity than a single scatterer. In either case, since the CMBMU system is more suited to low or medium mobility usage, it is more likely that the relative speed v will

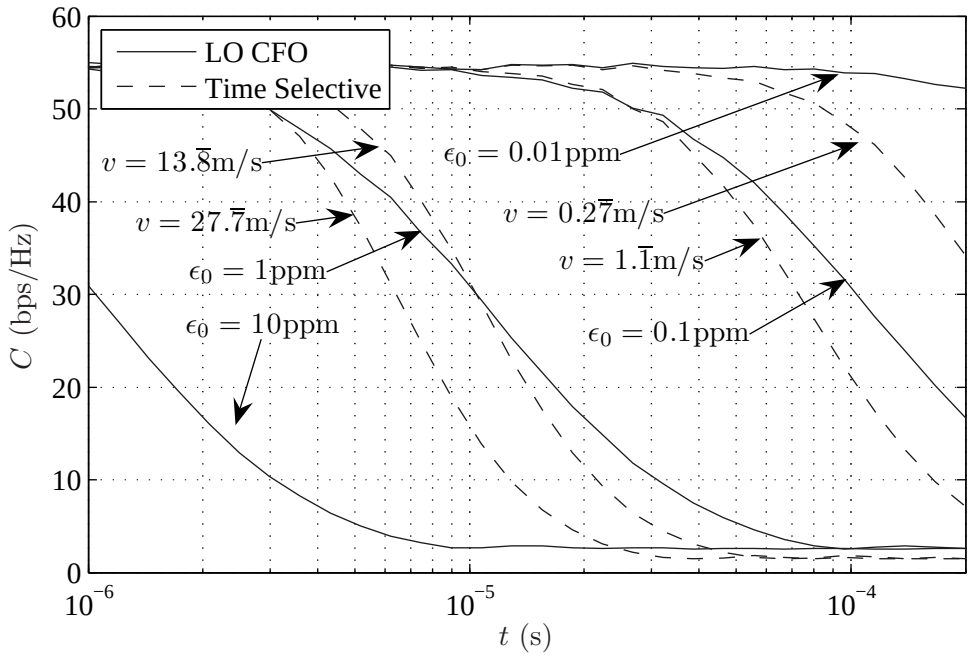

Figure 3.7: Effect of time varying channel on average sum-rate capacity compared to LO CFO, using ZF beamformer with EPT; $\Gamma_{BS} = 20$ dB, $B = 4$, $K = 32$, $N_R = 1$, $N_T = 8$.

be low enough to assume that LO CFO will remain the dominant obstacle. This is seen in Figure 3.7 for the curves for 4 km/h ($v = 1.\overline{1}$ m/s) and 1 km/h ($v = 0.2\overline{7}$ m/s), where LO CFO curves for $\epsilon_0 = 0.1$ ppm, $\epsilon_0 = 1$ ppm, and $\epsilon_0 = 10$ ppm are of equal or greater detriment to the sum-rate capacity; the R values for these values of v and ϵ_0 range from 27 to 10800.

3.4.1 Maximum Acceptable Carrier Frequency Offset

Figure 3.4 demonstrates that a threshold for maximum PO can be defined after which capacity begins to degrade. This section provides a discussion on how a MCS can be designed around the limitations posed by CFO.

In Figure 3.4, as long as $B > 2$, the number of independent LOs appears to have little effect on the onset of CFO-induced capacity degradation. To provide a complete picture, the effect of SNR and K on the system capacity should be determined. Simulations based on the capacity expression from (3.3) are shown in Figures 3.8 and 3.9, for a variety of SNRs and values of K, respectively. The normalized sum-rate capacity is used to provide a

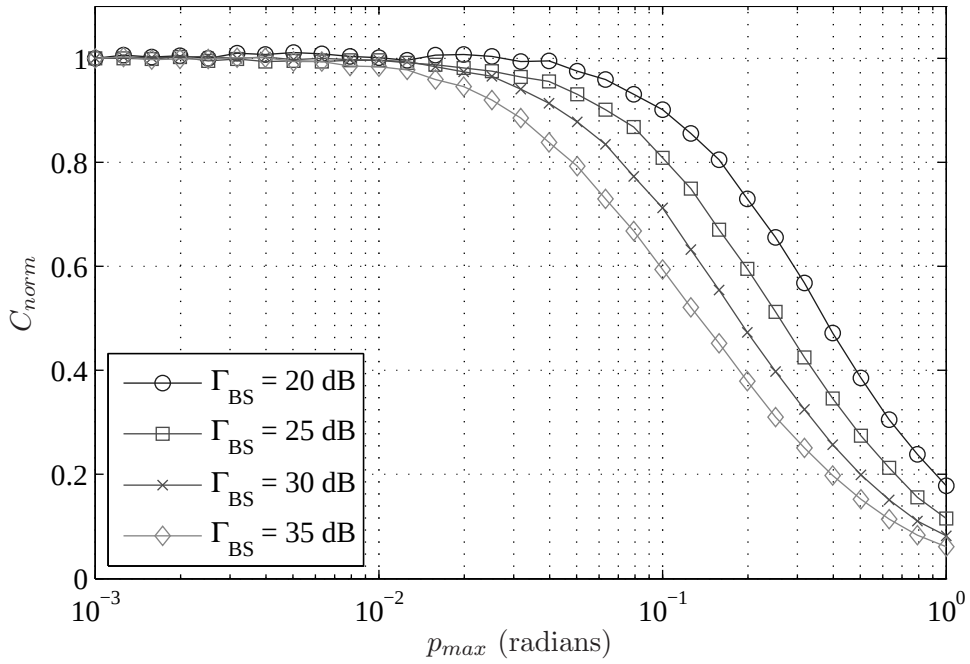

Figure 3.8: Effect of SNR on sum-rate capacity with LO CFO degradation, for equal power allocation with CSI; $B = 4$, $K = 32$, $N_R = 1$, $N_T = 8$.

comparison, and is defined as

$$C_{norm}(\tilde{\mathbf{H}}) = \frac{C(\tilde{\mathbf{H}})}{C(\mathbf{H})}. \tag{3.12}$$

Transmit power is distributed evenly to all K MSs using the zero-forcing beamformer with EPT.

In Figure 3.8, the effect of the SNR is shown. A shift in the capacity curves is evident: as noted for Figure 3.4, the 10% reduction in capacity that occurs when $\Gamma_{BS} = 20$ dB happens at $p_{max} \approx 0.1$ radians, and shifts to $p_{max} \approx 6.3 \times 10^{-2}$, 4.5×10^{-2}, and 2.9×10^{-2} radians for $\Gamma_{BS} = 25$, 30, and 35 dB, respectively. Note however that this figure displays the normalized sum-rate capacity; by increasing the SNR, the true sum-rate capacity increases as expected. The goal of this figure is to show the relative loss in capacity. Systems with higher capacity levels suffer a larger percentage loss due to CFO than those with lower capacity.

In Figure 3.9, the effect of the number of MSs, K, is shown. For smaller K, the slope of the capacity curves change: as more MSs are added to the system, the larger the slope. This is due to the additional interference in the system, where the BSs must now provide

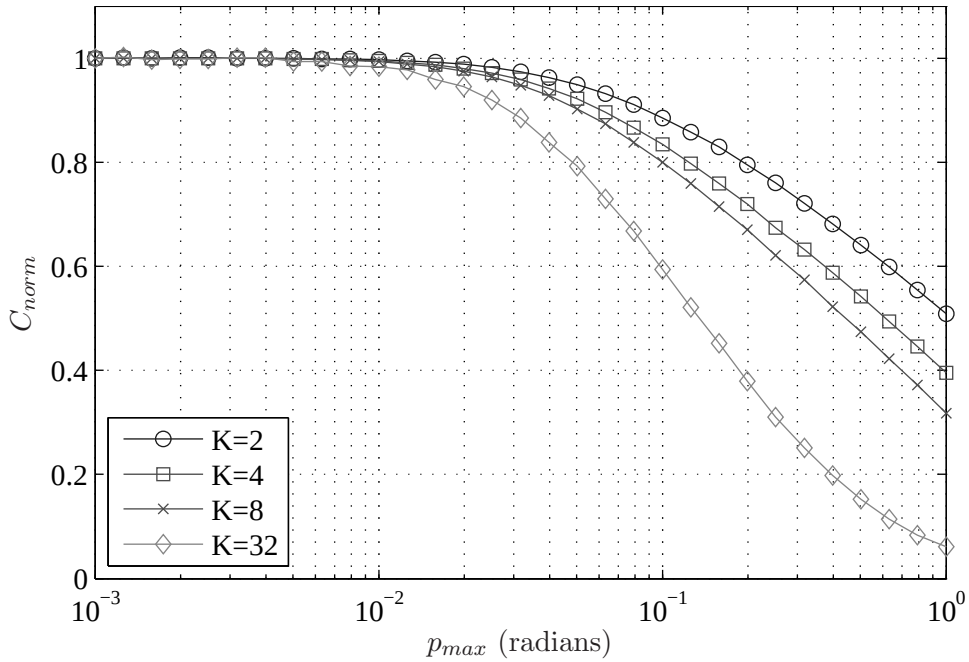

Figure 3.9: Effect of K on sum-rate capacity with LO CFO degradation, for equal power allocation with CSI; $\Gamma_{BS} = 35$ dB, $B = 4$, $N_R = 1$, $N_T = 8$.

additional orthogonal channels. For larger K, the degradation is more pronounced. Comparing the curves for $K = 2$ and $K = 32$, the inter-user interference reduces the value of p_{max} that limits capacity loss to 10% by a factor of 5.

After consideration of the above simulations, a general rule of thumb can be defined for a given SNR Γ_{BS} and number of MSs K: for example, when $\Gamma_{BS} = 20$ dB and $K = 32$, by limiting the PO to less than a threshold of $p_{th} = 0.1$ radians, capacity degradation can be limited to less than 10% regardless of the number of BSs. By defining the data frame size as N_f, an estimate of the worst-case normalized CFO that can be used without violating the above rule of thumb can be defined as

$$c_{th}(\Gamma_{BS} = 20 \text{ dB}) = 0.1/N_f. \tag{3.13}$$

The system parameters of f_c, ϵ_0, and T_s can be used to calculate an appropriate c_{max} in (3.1).

As an example, the following gives upper and lower limits in a hypothetical system, assuming that no feedback or estimation delay exists. For a CMBMU MCS with $f_c = 5$ GHz and $T_s = 1$ μs, and with the CFO accuracy in the range from 0.01 ppm to 10 ppm,

the worst-case CFO, c_{max}, is in the range

$$3.14 \times 10^{-4} \leq c_{max} \leq 3.14 \times 10^{-1}. \tag{3.14}$$

For $\Gamma_{BS} = 20$ dB and $K = 32$, $p_{th} = 0.1$ radians, and the range of c_{max} translates to data frame sizes of $0.1/3.14 \times 10^{-4} \approx 318$ symbols down to 0 symbols, respectively, since $3.14 \times 10^{-1} > p_{th}$. It is evident that CMBMU systems that suffer from moderate to high levels of LO CFO cannot operate without some sort of CFO compensation.

For comparison, the single scatterer model of Section 3.2 with a relative velocity in the range of 4 km/h to 50 km/h has a c_{max} in the range

$$1.16 \times 10^{-4} \leq c_{max} \leq 1.50 \times 10^{-3}, \tag{3.15}$$

which translates to data frame sizes of 862 down to 68 symbols, respectively. With an appropriate frame size, it is possible to operate the system by re-estimating the channel gains at the beginning of each frame. This would have the effect of resetting the phase offset to zero.

3.5 Summary

This chapter considered the effects of channel impairments on the sum-rate capacity of a zero-forcing CMBMU beamformer. The effects of LO-induced CFO and time selectivity were compared. The special case of single scatterer Doppler-induced CFO was also considered.

It was verified that the performance degradation due to multiple LO CFOs is not strongly dependent on the number of BSs (provided that there are at least two), but primarily on the SNR, the number of MSs and the magnitude of the CFOs. The results suggest that, compared to a time-selective channel with low to moderate fade rates, LO CFOs on the order of 0.1 ppm to 10 ppm are more detrimental to the sum-rate capacity.

Also, it was demonstrated that a CMBMU system can operate with a time-selective channel, as long as the channel is re-estimated within a certain time window. However, the magnitude of the LO CFOs makes some form of correction necessary. In other words, CMBMU systems with unsynchronized BS and MS LOs require some level of CFO estimation and correction. This provides motivation for investigation into compensation for multiple LO-induced CFOs in CMBMU systems, presented in the following chapters.

Chapter 4

Multi-CFO Estimation

In Chapter 3, the effects of CFO and time selectivity were demonstrated on the sum-rate capacity of a coordinated multibase/multiuser (CMBMU) system. It was shown that LO-induced CFO has the most detrimental effect on capacity. Since capacity degradation caused by LO CFOs is considered to be one of the largest barriers to implementation of CMBMU systems, efficient techniques for CFO estimation and subsequent correction provide the major focus for this thesis. In this chapter, the focus is on multi-CFO estimation at the MS.

In this chapter, the training model from Section 2.4.2 will be used, with the Doppler rate set to zero (i.e., a quasi-static channel). To begin with, the symbol-spaced matched filter training model will be used (i.e., $N_{ss} = 1$ and $L = 0$). This restriction will be relaxed when dealing with symbol synchronization and frequency selectivity in Section 4.6. Since this work considers CFO estimation at an individual MS, the MS notation will be dropped; for example, compared to the original model, $c_{b,k} = c_b$ and $\mathbf{y}_k = \mathbf{y}$.

A brief review of existing works is given in Section 4.1, followed by the introduction of a group of novel convex CFO estimators in Section 4.2. Section 4.3 derives a new ML metric after marginalization of the channel gains from the pdf of the received samples. In Section 4.4, TS length limitations for the convex estimators are discussed, followed by the presentation of a successive approximation technique that overcomes the length restrictions. Complexity of existing and proposed CFO estimators are discussed in Section 4.5. The channel issues of symbol synchronization and frequency selectivity are addressed by a simple modification to the ML metric in Section 4.6. Simulation results for the multi-CFO estimators are given in Section 4.7.

4.1 Prior Work

The multiple CFO estimation schemes considered in this work require a reference signal to be transmitted. For systems with multiple transmit antennas, orthogonal TSs are sent from each antenna. The receiver, in this case the MS, uses the orthogonal TSs and the received samples to estimate channel and system parameters. In this section, previous work on the design of MIMO channel TSs, optimal CFO estimators, and reduced complexity multi-CFO estimators are summarized.

4.1.1 Training Sequences for CFOs

Training sequences are used in MCSs to provide a reference signal for identification of the channel gains. As modeled in Section 2.4.2, TSs can also be used in the estimation of other system parameters, such as CFO. For estimation of either channel gains or CFOs, two of the most important parameters for TS design are TS length and correlation coefficients. The following gives a brief review of work done in the optimization of these parameters.

First, a brief overview is given of MIMO channel gain estimate quality using orthogonal TSs. In can be shown that the MSE of the channel gain estimate is dependent on the TS length, N. Applying the pseudo-inverse of the TS matrix $\mathbf{X}$ results in the LS channel estimate

$$\begin{aligned} \hat{\mathbf{h}}(\mathbf{c}) &= \mathbf{X}^{PINV}\left(\mathbf{V}(\mathbf{c})\mathbf{h}+\mathbf{z}\right) \\ &= \sqrt{P}\mathbf{X}^{PINV}\left(\mathbf{X}\odot\mathbf{D}(\mathbf{c})\right)\mathbf{h}+\mathbf{X}^{P}\mathbf{z}, \end{aligned} \tag{4.1}$$

where $\mathbf{X}^{PINV}=\left(\mathbf{X}^T\mathbf{X}\right)^{-1}\mathbf{X}^T$ refers to the pseudo-inverse of $\mathbf{X}$, $\mathbf{V}(\mathbf{c})=\left(\mathbf{X}\odot\mathbf{D}(\mathbf{c})\right)\sqrt{\mathbf{P}}$ from (2.32), and $\mathbf{P}=P\mathbf{I}_{BN_T}$ is the diagonal transmit power matrix with transmit power P Watts. After weighting the estimates by the transmit power to remove the bias term of $\sqrt{P}$ in (4.1), the MSE of the channel gain estimate is found as

$$E_{h,z}\left[\left|\mathbf{h}-\frac{1}{\sqrt{P}}\hat{\mathbf{h}}(\mathbf{c})\right|^2\right]=E_h\left[\mathbf{h}^\dagger\left|\mathbf{I}_{BN_T}-\mathbf{X}^{PINV}\left(\mathbf{X}\odot\mathbf{D}(\mathbf{c})\right)\right|^2\mathbf{h}\right]+\frac{1}{P}E_z\left[\left|\mathbf{X}^P\mathbf{z}\right|^2\right], \tag{4.2}$$

where we use the fact that the channel gains and the noise terms are independent. If the CFOs in $\mathbf{c}$ were zero, then $\mathbf{D}(\mathbf{c})=\mathbf{I}_{BN_T}$, and the first term would disappear. Otherwise, (4.2) shows that the CFO contributes to the MSE of the channel gains. If $\mathbf{c}$ is set to zero,

then the MSE is solely dependent on the noise variance, so

$$E_z\left[\left|\mathbf{h}-\frac{1}{\sqrt{P}}\hat{\mathbf{h}}(\mathbf{0})\right|^2\right] = \frac{1}{P}E_z\left[\left|\mathbf{X}^{PINV}\mathbf{z}\right|^2\right] \quad (4.3)$$

$$= \frac{1}{PN^2}E_z\left[trace\left(\mathbf{X}\mathbf{X}^T\mathbf{z}\mathbf{z}^\dagger\right)\right]$$

$$= \frac{BN_TN_0}{PN}. \quad (4.4)$$

The above assumes orthogonal TSs, so that the TS autocorrelation is $\mathbf{X}^T\mathbf{X} = N\mathbf{I}_{BN_T}$, and uses the relation $E_z\left[trace\left(\mathbf{X}\mathbf{X}^T\mathbf{z}\mathbf{z}^\dagger\right)\right] = N_0 \cdot trace\left(\mathbf{X}\mathbf{X}^T\mathbf{I}_N\right)$ for a zero-mean random variable [66]. Note that the MSE of the channel gain estimate is inversely proportional to N, and that this analysis is made simple because of the use of orthogonal TSs.

Since increasing N results in better channel estimates, if the MSE were to be optimized with no consideration for system throughput, then the frame would consist solely of training symbols; i.e., if $N_f = N + N_d$ is the total number of symbols per frame and N_d is the total number of data symbols per frame, $N \rightarrow N_f$. Of course, this would reduce the system throughput to zero. In [31], the trade-off between the TS length N and the system throughput is considered. Hassibi and Hochwald in [31] solve this problem by using an expression for system capacity that includes the contribution of the known TS data. For $N_f = 200$, the work in [31] reports optimum values of N for the ratio N/N_f being anywhere from 19.5% for a symbol SNR of 0 decibels (dB) to 9.0% for a symbol SNR of 18 dB.

The TS autocorrelation becomes much more important in the presence of CFO, as the orthogonality of the TSs is compromised. The autocorrelation properties of the TSs were considered by Stoica and Besson in [73] and by Ghogho and Swami in [25]. The work in [73] considers a single antenna system using the asymptotic Cramer-Rao lower bound (CRLB), while that in [25] considers a multiple antenna system using the exact CRLB. Both use the joint CFO/CSI CRLB to define the autocorrelation properties of the training sequences. Stoica and Besson report that TSs with a diagonal autocorrelation matrix satisfy the criteria for the optimum asymptotic CRLB. A diagonal autocorrelation matrix is attained by ensuring that all TSs used for training are orthogonal to each other. The work by Ghogho and Swami proposes channel-independent performance training (CIPT), which manipulates the CRLB to be independent of the channel gains. The modified CRLB is then used to design TSs, which also have a diagonal autocorrelation matrix. The benefits of the CIPT method include improved MSE for both channel gain and CFO estimates.

Optimum design of TSs in the presence of CFO, but without considering explicit CFO estimation, has been looked at by Schellman and Stanczak in [63]. As the techniques in [63] are solely concerned with CSI estimation, they do not solve the degradation of the sum-rate capacity due to CFO covered in Section 3.1. Schellman and Stanczak propose the use of Golay sequence pairs to improve the TS cross-correlation properties in the presence of CFO. By utilizing Golay sequence pairs composed of two short sequences, and by extending these codes with periodic repetition of Hadamard codes, the MSE is reduced by a order of magnitude. After successful CSI estimation, these codes could be used to identify the CFO in much the same way as in [13]. However, the structure of the TSs necessitates zero-padding during training, which would result in higher per-symbol transmit energy or longer TSs. This limitation is similar to the time orthogonal techniques that will be introduced in Section 4.1.4.

In this thesis, orthogonal or quasi-orthogonal TSs are used depending on the length N, as mentioned in Section 2.4.2. The orthogonal Hadamard sequences, used when $N = 2^q$ and q is a positive integer, provide the diagonal covariance matrix required by [73]. In the following section, the details of CFO estimation using these TSs are presented.

4.1.2 Maximum Likelihood CFO Estimation

In this section, a brief overview of the optimum ML estimation metric for multiple CFOs is given. This is followed by a description of existing sub-optimal single- and multi-CFO estimation techniques that are based on the optimum ML solution.

Optimum Multi-CFO Estimation

Using the training model shown in Section 2.4.2, the CFO estimation problem is stated as follows: given a vector of received and sampled training symbols $\mathbf{y}$ and *a priori* knowledge of $\mathbf{h}$, the optimum CFO estimates $\hat{\mathbf{c}}$ satisfy

$$\hat{\mathbf{c}} = \arg\max_{\mathbf{c}} p\left(\mathbf{y}|\mathbf{h},\mathbf{c}\right), \tag{4.5}$$

where $p\left(\mathbf{y}|\mathbf{h},\mathbf{c}\right)$ is the conditional probability density function (pdf) of $\mathbf{y}$.

The maximum likelihood criterion is used throughout the multi-CFO estimation literature, and provides the optimal but exponentially complex starting point for the techniques mentioned in the following. Starting with (2.32), the conditional pdf of the MF outputs at

the MS as a function of the channel gains $\mathbf{h}$ and the CFOs $\mathbf{c}$ is

$$p(\mathbf{y}|\mathbf{h},\mathbf{c}) = \frac{1}{(2\pi)^N N N_0} \exp\left(-\frac{\left|\left|\mathbf{y} - \overline{\mathbf{V}}(\mathbf{c})\mathbf{h}\right|\right|^2}{2N_0} \right) \tag{4.6}$$

and can be reduced to the metric equivalent log-likelihood

$$\Sigma(\mathbf{h},\mathbf{c}) = \left|\left|\mathbf{y} - \overline{\mathbf{V}}(\mathbf{c})\mathbf{h}\right|\right|^2. \tag{4.7}$$

Note that (4.7) no longer assumes an *a priori* CSI pdf, since only the TSs $\mathbf{X}$ are known at the MSs. It is the goal of the ML estimator to select values for $\mathbf{h}$ and $\mathbf{c}$ that minimize $\Sigma(\mathbf{h},\mathbf{c})$, or

$$\left(\hat{\mathbf{h}},\hat{\mathbf{c}}\right) = \arg\min_{\mathbf{h},\mathbf{c}} \Sigma(\mathbf{h},\mathbf{c}). \tag{4.8}$$

In [1], [6], and for most of Chapter 4, the joint CFO/CSI ML estimate is based on a least squares (LS) solution for the CSI. It is modified here to suit the CMBMU system. By substituting the LS solution for the CSI, the estimation metric is made dependent only upon the CFOs, as will be shown in the following. A CSI estimate can be made with the resulting CFO estimates.

The first solution step is to replace the CSI $\mathbf{h}$ with its LS estimate

$$\hat{\mathbf{h}} = \left(\overline{\mathbf{V}}^\dagger(\mathbf{c})\overline{\mathbf{V}}(\mathbf{c})\right)^{-1}\overline{\mathbf{V}}^\dagger(\mathbf{c})\mathbf{y}. \tag{4.9}$$

After substituting (4.9) into (4.7) and simplifying, we get a new metric

$$\Lambda(\mathbf{c}) = \mathbf{y}^\dagger\overline{\mathbf{V}}(\mathbf{c})\left(\overline{\mathbf{V}}^\dagger(\mathbf{c})\overline{\mathbf{V}}(\mathbf{c})\right)^{-1}\overline{\mathbf{V}}^\dagger(\mathbf{c})\mathbf{y}. \tag{4.10}$$

Using this expression, the CFO estimation problem that was initially stated as the minimization of $\Sigma(\mathbf{h},\mathbf{c})$ can be stated as a maximization

$$\hat{\mathbf{c}} = \arg\max_{\mathbf{c}} \Lambda(\mathbf{c}). \tag{4.11}$$

Once the CFO $\hat{\mathbf{c}}$ has been estimated, it can be used in (4.9) to calculate the CSI.

Because there are B BSs each with its own CFO, the length of $\hat{\mathbf{c}}$ is B. Consequently, the complexity of an exhaustive search over discrete CFO values would increase exponentially with B. This provides justification for work on the reduced-complexity techniques presented in the following.

Single-CFO Estimation

Two examples of single-CFO estimation techniques are given in the following. Although single-CFO techniques are not useful for CMBMU systems, they provide insight into CFO estimation strategies. The benefits of multiple receive antennas for CFO estimation was discussed in [11] by Cavers, for a time-selective, flat-fading channel using a pair of complex tones as a reference. It is shown that the CFO estimation error variance decreases inversely with the number of receive antennas. In [69], Simoens and Moeneclaey consider data- and code-aided joint CFO/CSI estimation in flat-fading MIMO systems, with the assumption of a single CFO. Similar to Section 3.2, Simoens and Moeneclaey assume that the Doppler-induced CFOs that result from each scatterer are equivalent since the angle of arrival for the paths are the same. This situation is similar to the case of the downlink of the CMBMU system, where a single BS may have a relatively narrow set of arrival angles.

Multi-CFO Estimation

For the CMBMU system, more complex multi-CFO estimation schemes are necessary. While the estimation problem of multiple CFOs resulting from independent LOs in the downlink has not been considered before, there are a number of estimators based on multiple Doppler-induced CFOs. Since the optimum ML solution for joint estimation of the multiple CFOs is computationally prohibitive, the following techniques are suboptimum.

In [54], Oh et al. present a time division multiplexing (TDM) scheme for estimating multiple CFOs in the uplink of a wireless sensor network. The use of TDM allows each individual CFO to be estimated sequentially by the BS, since the TSs remain orthogonal regardless of the CFOs. In a paper by Besson and Stoica [6], the Doppler-induced multi-CFO problem is addressed in similar TDM fashion. The TDM training symbols from each BS are also interleaved to preserve the time aperture of the full training duration. That is, for B BSs, each BS will transmit a training symbol every B^{th} symbol time. In addition, Besson and Stoica analyzed the CRLB of the multi-CFO problem, and identified that the CFOs correlate the TSs, where the original TSs are drawn from an orthogonal set. Since TS correlation increases the MSE, the TDM scheme effectively avoids the correlation problem. Ahmed et al. in [1] assume that this correlation can be neglected. Specifically, this can be done for the case when the Doppler-induced CFOs are small enough, or the TS length N is short enough, that the correlations are very small. Most recently, Zeng et al. in [94]

use a blind technique to estimate a composite channel that includes both CFOs and time asynchronicity. However, the TSs are made time orthogonal to avoid implicit multiple CFO estimation, similar to [6] and [54].

Below, we provide expressions for the estimators of [1] and [6], which will be used in a comparison to the proposed estimators of Sections 4.2 and 4.4 in the simulations presented in Section 4.7.

4.1.3 ST-AO Estimator

In [1], Ahmed et al. exploit the fact that in certain cases, the covariance matrix off-diagonals will be very small compared to the diagonals. This approximation, that $\mathbf{V}^{\dagger}(\mathbf{c})\mathbf{V}(\mathbf{c}) \approx \mathbf{I}_{BN_T}$, allows each CFO to be estimated independently. In practice, this approximation could be valid when the sequences are short enough to avoid accumulation of sufficient phase difference to alter the correlations between the TSs. We will refer to this technique as simultaneous training - assumed orthogonality (ST-AO).

With this approximation, (4.10) can be rewritten as is

$$\begin{aligned} \Lambda_{ST-AO}(c_b) &= \mathbf{y}^{\dagger}\overline{\mathbf{V}}_b(c_b)\overline{\mathbf{V}}_b^{\dagger}(c_b)\mathbf{y} \\ &= \sum_{m=1}^{N_T}\sum_{q=1}^{N_R}\left|\sum_{n=0}^{N-1} y_q^*[n]x_m[n]e^{jc_bn}\right|^2 \end{aligned} \tag{4.12}$$

where $y_q[n]$ refers to the received sample at the q^{th} antenna at time n and $x_m[n]$ refers to the training symbol transmitted from antenna m at time n. The second line of (4.12) is rewritten to demonstrate that the fast Fourier transform (FFT) can be used to solve for $\hat{c}_b$.

Since the performance of the ST-AO estimator is contingent on $\mathbf{V}^{\dagger}(\mathbf{c})\mathbf{V}(\mathbf{c})$ being diagonal, it is very sensitive to accumulation of the CFO. As N or the maximum CFO c_{max} increase and the off-diagonals of $\mathbf{V}^{\dagger}(\mathbf{c})\mathbf{V}(\mathbf{c})$ grow, the sequences will be long enough to allow accumulation of the CFO. The result is an error floor at high SNR, which is dependent upon the TS length N and the normalized CFO c_{max}.

4.1.4 TO Estimator

The value of orthogonality is evident in comparison of (4.12) and (4.10). Orthogonality can be forced in spite of the CFOs by allowing only one BS to transmit in any symbol time. One such format is bunching, e.g., [54], in which each BS in turn sends its TS of length

N/B. This reduces computation to BN_TN_R FFTs, as in (4.12), followed by B independent searches. However, the method has two serious disadvantages. First, the time span, or aperture, of any TS has been reduced by a factor of B, compared to the total duration of TS transmissions, with a proportional increase in the variance of the frequency estimates. Second, to maintain the same energy as a TS of the original length N, the peak power must be B times greater. For radio systems with several BSs, this means more expensive power amplifiers. An alternative is to keep the original length N of each TS and increase the total duration of TS transmissions by a factor B, but this in turn will reduce the total throughput of the channel.

Another format that maintains orthogonality with only one BS transmitting at a time is interleaving, e.g., [6], in which BSs transmit single symbols of their length-N/B TSs in round-robin fashion. The duration of each TS remains N symbol times, so the method does not experience the loss of aperture suffered by the bunching format. It has been shown [6] to meet the CRLB. We will refer to this method as time orthogonal (TO). Like the bunching format, TO requires B times the peak power of simultaneously transmitted TSs. It has another even more serious defect: lack of time synchronization among the BSs symbols as received by the MS destroys the orthogonality. In a CMBMU system with a variety of propagation delays, this symbol-synchronous reception is virtually impossible to achieve. Delay spread in the channel has a similar effect. The format may not be appropriate for realistic channels.

4.2 Convex Methods for Multiple CFO Estimation

This section presents work on novel convex methods for multi-CFO estimation. The techniques herein provide a bridge between the computationally intensive optimum ML technique from Section 4.1.2 and the low complexity ST-AO and TO techniques from Section 4.1.3 and 4.1.4, respectively. The main benefits of the convex methods over the ST-AO and TO methods include compensation for TS correlation and a reduction in training symbol transmit power which results in lower peak power for RF amplifiers.

The design goals for multi-CFO estimators in a CMBMU system are to use simultaneous TSs, which maximize data throughput, while compensating for any correlation that is caused by the CFOs themselves. The cause of the TS correlation was introduced in Section 4.1.2. An example that quantifies the TS correlation is shown in Figure 4.1; the curves correspond

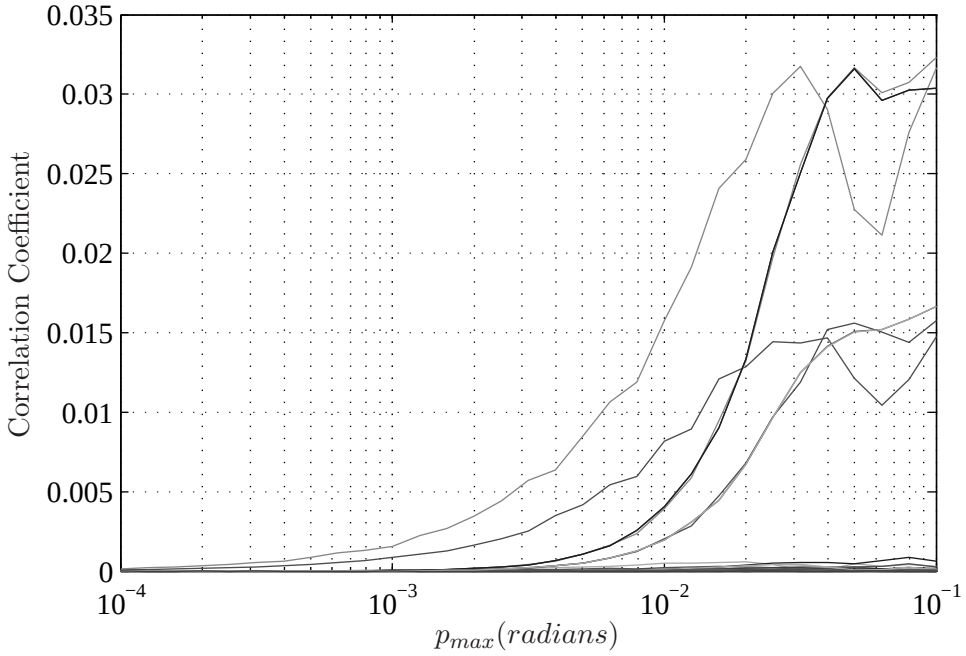

Figure 4.1: TS correlation coefficient versus PO p_{max}, demonstrating the increase in TS correlation as the severity of the CFO increases, where each curve represents the correlation coefficient between two TSs; $N = 64$, $\Gamma_b = 40$ dB, $B = 4$, $N_R = 2$, $N_T = 2$.

to the $BN_T(BN_T-1)/2$ correlation coefficients of the TSs, and were generated with 10^4 Monte Carlo realizations of a CMBMU system with $B=4$, $N=80$, $N_T=N_R=2$, $\Gamma_b=40$ dB, with random TSs. The x-axis depicts a linear increase to the maximum phase offset $p_{max}=Nc_{max}$ caused by the CFOs; the general trend of an increasing correlation coefficient due to increasing p_{max} is obvious.

For simultaneous multi-CFO estimation, the lack of orthogonality is accounted for in the maximization of the log-likelihood (4.10). This maximization is performed by either the Gradient descent or Newton's method. The estimators are referred to as simultaneous training - gradient step (ST-G) and simultaneous training - Newton step (ST-N), respectively, and are described in Sections 4.2.1 and 4.2.2. The performance of both are assessed by simulation in Section 4.7, with the CRLB derived for the LO-based CFO in Appendix A.

As in ST-AO, all TSs are transmitted simultaneously from all BS antennas. However, in contrast to ST-AO, ST-G and ST-N account for the TS correlation introduced by the CFOs, while maintaining a reduced computational complexity compared to the optimal ML solution. The trade-off between the use of simultaneous TSs versus time orthogonal TSs is between sequence length and symbol power. For example, to ensure equal TS energy with B BSs, a time orthogonal system would have to use TSs that are B times shorter with a per-symbol power B times higher than with simultaneous training. This trade-off favours simultaneous training, given that power amplifiers are usually one of the most expensive parts of a BS. Simultaneous training has the problem that TS orthogonality is degraded by the CFOs; however, we show that proper accounting of the TS correlation in ST-G and ST-N compensates for this effect.

The estimators in Section 4.2.1 and 4.2.2 are presented with symbol-synchronous arrivals and no delay spread. Straightforward extensions accommodate asynchronicity and delay spread, as discussed in Section 4.6.

4.2.1 Gradient Method

The gradient descent technique is used to search for the zero-gradient point [9] on the surface of the space defined by (4.10). Defining N_{ITER} as the number of iterations, t as the step size, and $\hat{\mathbf{c}}(i)$ as the CFO estimate at the i^{th} iteration step, the gradient descent algorithm

is

$$\begin{aligned}
&\text{initialize } \hat{\mathbf{c}}(0) = \mathbf{0} \\
&\text{for } i = 1 : N_{ITER} \\
&\quad \hat{\mathbf{c}}(i) = \hat{\mathbf{c}}(i-1) - \boldsymbol{\mu}_g\left(\hat{\mathbf{c}}(i-1)\right) \\
&\text{end,}
\end{aligned} \tag{4.13}$$

where the Gradient step is defined as

$$\boldsymbol{\mu}_g\left(\hat{\mathbf{c}}\right) = t \bigtriangledown \Lambda\left(\hat{\mathbf{c}}\right). \tag{4.14}$$

We can find the gradient of $\Lambda(\mathbf{c})$ with a combination of analytical and numerical evaluation. Using (4.10), define $\mathbf{G}(\mathbf{c}) = \mathbf{V}(\mathbf{c})\left(\mathbf{V}^{\dagger}(\mathbf{c})\mathbf{V}(\mathbf{c})\right)^{-1}\mathbf{V}^{\dagger}(\mathbf{c})$, so that $\Lambda(\mathbf{c}) = \mathbf{y}^{\dagger}\overline{\mathbf{G}}(\mathbf{c})\mathbf{y}$, where $\overline{\mathbf{G}(\mathbf{c})} = \mathbf{I}_{N_R} \otimes \mathbf{G}(\mathbf{c})$ The b^{th} component of the $\bigtriangledown\Lambda(\mathbf{c}) \in \mathbb{R}^{B\times 1}$ vector can be expressed as

$$\frac{\partial}{\partial \hat{c}_b}\Lambda(\hat{\mathbf{c}}) = \mathbf{y}^{\dagger}\overline{\mathbf{G}}_b'(\hat{\mathbf{c}})\mathbf{y}, \tag{4.15}$$

where

$$\begin{aligned}
\mathbf{G}_b'(\hat{\mathbf{c}}) &= \frac{\partial}{\partial \hat{c}\, b}\mathbf{G}(\hat{\mathbf{c}}) \qquad (4.16)\\
&= \mathbf{A}_b(\hat{c}_b)\mathbf{F}(\hat{\mathbf{c}})\mathbf{V}^{\dagger}(\hat{\mathbf{c}}) + \mathbf{V}(\hat{\mathbf{c}})\mathbf{F}(\hat{\mathbf{c}})\mathbf{A}_b^{\dagger}(\hat{c}_b) - \\
&\quad \mathbf{V}(\hat{\mathbf{c}})\mathbf{F}(\hat{\mathbf{c}})\mathbf{B}_b(\hat{\mathbf{c}})\mathbf{F}(\hat{\mathbf{c}})\mathbf{V}^{\dagger}(\hat{\mathbf{c}}), \\
\mathbf{A}_b(\hat{c}_b) &= [\mathbf{0}_{N\times(b-1)N_T}\ j\mathbf{Z}\mathbf{X}_b \odot \boldsymbol{\Omega}_b(\hat{c}_b)\ \mathbf{0}_{N\times(B-b)N_T}] \in \mathbb{C}^{N\times BN_T} \\
\mathbf{B}_b(\hat{\mathbf{c}}) &= \mathbf{A}_b^{\dagger}(\hat{c}_b)\mathbf{V}(\hat{\mathbf{c}}) + \mathbf{V}^{\dagger}(\hat{\mathbf{c}})\mathbf{A}_b(\hat{c}_b) \in \mathbb{C}^{BN_T\times BN_T} \\
\mathbf{F}(\hat{\mathbf{c}}) &= \left(\mathbf{V}^{\dagger}(\hat{\mathbf{c}})\mathbf{V}(\hat{\mathbf{c}})\right)^{-1} \in \mathbb{C}^{BN_T\times BN_T} \\
\mathbf{Z} &= diag(0, 1, 2\cdots N-1) \in \mathbb{R}^{N\times N}
\end{aligned}$$

and the matrix $\mathbf{0}_{N_1\times N_2} \in \mathbb{R}^{N_1\times N_2}$ is an all zero matrix.

The convergence of the algorithm in (4.13) is controlled by the step size t. The optimized t is defined as the value that allows convergence in the fewest iterations, and can be found through simulation; a larger t ensures faster convergence, so a discrete brute force method reduces t in steps until convergence is observed. Since the gradient step in (4.15) is dependent on the channel state from $\mathbf{y}$, the optimized value of t fluctuates due to channel fades and may be different for each BS (i.e., each CFO). A method to account for this is to allow each BS CFO gradient its own step size. This can be done with the assumption that the CFO

estimates are uncorrelated so that their convergences are uncoupled (verified by simulation of $\Lambda(\hat{\mathbf{c}}_k)$). The new CFO-specific weights, t_b for the b^{th} CFO, include the term $||\mathbf{h}_b||$, where $||\cdot||$ refers to the Euclidean norm of the zero-mean channel gain matrix. Since the channel gains are not available, an estimate must be calculated. Simulations show that the LS estimate for $\hat{\mathbf{h}}_b$ in (4.17) is satisfactory, even in the presence of CFO.

$$\hat{\mathbf{h}}_b = \left(\mathbf{X}_b^{\dagger}\mathbf{X}_b\right)^{-1}\mathbf{X}_b^{\dagger}\mathbf{y}, \tag{4.17}$$

This estimate is calculated using $\mathbf{X}_b$, which is the TS matrix transmitted from the b^{th} BS. Note that $\hat{\mathbf{h}}_b$ is already available from the channel estimation process, and proceeds in parallel with the CFO estimation. The improved update to the CFO estimate in (4.13) now becomes

$$\hat{\mathbf{c}}(i) = \hat{\mathbf{c}}(i-1) - \mathbf{T} \bigtriangledown \Lambda\left(\hat{\mathbf{c}}(i-1)\right), \tag{4.18}$$

where $\mathbf{T} \in \mathbb{R}^{B\times B}$ is a diagonal matrix with components $t_b = a/||\hat{\mathbf{h}}_b||$ and a is a constant.

4.2.2 Newton Method

The Newton method uses the Hessian of the ML CFO metric to find the zero-gradient point [9]. The Newton method has the form [9]

$$\begin{aligned}
&\text{initialize } \ \hat{\mathbf{c}}(0) = \mathbf{0} \\
&\text{for } \ i = 1 : N_{ITER} \\
&\quad \hat{\mathbf{c}}(i) = \hat{\mathbf{c}}(i-1) - \boldsymbol{\mu}_{ns}\left(\hat{\mathbf{c}}(i-1)\right) \\
&\text{end}
\end{aligned} \tag{4.19}$$

where the Newton step is

$$\boldsymbol{\mu}_{ns}(\hat{\mathbf{c}}) = \left[\bigtriangledown^2\Lambda(\hat{\mathbf{c}})\right]^{-1} \bigtriangledown \Lambda(\hat{\mathbf{c}}). \tag{4.20}$$

The expression $\bigtriangledown^2\Lambda(\hat{\mathbf{c}}) \in \mathbb{R}^{B\times B}$ refers to the Hessian of $\Lambda(\hat{\mathbf{c}})$.

The expression for $\bigtriangledown\Lambda(\hat{\mathbf{c}})$ is the same as in (4.15), so the expression for the Hessian of the joint metric must be derived for a given $\hat{\mathbf{c}}$. The Hessian has diagonals with a slightly different form than the off-diagonals. For $b \neq l$, the (b^{th}, l^{th}) entry of the $B \times B$ matrix $\bigtriangledown^2\Lambda(\hat{\mathbf{c}})$ is

$$\frac{\partial^2}{\partial\hat{c}_b\partial\hat{c}_l}\Lambda(\hat{\mathbf{c}}) = \mathbf{y}^{\dagger}\left[\overline{\mathbf{G}}''_{b,l}(\hat{\mathbf{c}})\right]\mathbf{y}, \tag{4.21}$$

where $\overline{\mathbf{G}}''_{b,l}(\hat{\mathbf{c}}) = \mathbf{I}_{N_R} \otimes \mathbf{G}''_{b,l}(\hat{\mathbf{c}})$ and

$$\begin{aligned} \mathbf{G}''_{b,l}(\hat{\mathbf{c}}) &= \frac{\partial^2}{\partial \hat{c}_b \partial \hat{c}_l} \mathbf{G}(\hat{\mathbf{c}}) \\ &= \mathbf{\Phi}_{b,l}(\hat{\mathbf{c}}) + \mathbf{\Phi}^{\dagger}_{b,l}(\hat{\mathbf{c}}) \;=\; \mathbf{G}''_{l,b}(\hat{\mathbf{c}}) \end{aligned} \tag{4.22}$$

and

$$\begin{aligned} \mathbf{\Phi}_{b,l}(\hat{\mathbf{c}}) &= \mathbf{A}_b(\hat{c}_b)\mathbf{F}(\hat{\mathbf{c}})\mathbf{A}^{\dagger}_l(\hat{c}_l) - \mathbf{V}(\hat{\mathbf{c}})\mathbf{F}(\hat{\mathbf{c}})\mathbf{B}_b(\hat{\mathbf{c}})\mathbf{F}(\hat{\mathbf{c}})\mathbf{A}^{\dagger}_l(\hat{c}_l) \\ &\quad -\mathbf{A}_b(\hat{c}_b)\mathbf{F}(\hat{\mathbf{c}})\mathbf{B}_l(\hat{\mathbf{c}})\mathbf{F}(\hat{\mathbf{c}})\mathbf{V}^{\dagger}(\hat{\mathbf{c}}) \\ &\quad -\mathbf{V}(\hat{\mathbf{c}})\mathbf{F}(\hat{\mathbf{c}})\mathbf{A}^{\dagger}_b(\hat{c}_b)\mathbf{A}_l(\hat{c}_l)\mathbf{F}(\hat{\mathbf{c}})\mathbf{V}^{\dagger}(\hat{\mathbf{c}}) \\ &\quad -\mathbf{V}(\hat{\mathbf{c}})\mathbf{F}(\hat{\mathbf{c}})\mathbf{B}_b(\hat{\mathbf{c}})\mathbf{F}(\hat{\mathbf{c}})\mathbf{B}_l(\hat{\mathbf{c}}k)\mathbf{F}(\hat{\mathbf{c}})\mathbf{V}^{\dagger}(\hat{\mathbf{c}}). \end{aligned} \tag{4.23}$$

For the diagonals $b = l$, the expression for $\mathbf{\Phi}_{b,b}(\hat{\mathbf{c}})$ is

$$\begin{aligned} \mathbf{\Phi}_{b,b}(\hat{\mathbf{c}}) &= \mathbf{A}_b(\hat{c}_b)\mathbf{F}(\hat{\mathbf{c}})\mathbf{A}^{\dagger}_b(\hat{c}_b) - \mathbf{V}(\hat{\mathbf{c}})\mathbf{F}(\hat{\mathbf{c}})\mathbf{B}_b(\hat{\mathbf{c}})\mathbf{F}(\hat{\mathbf{c}})\mathbf{A}_b(\hat{c}_b) \\ &\quad -\mathbf{A}_b(\hat{c}_b)\mathbf{F}(\hat{\mathbf{c}})\mathbf{B}_b(\hat{\mathbf{c}})\mathbf{F}(\hat{\mathbf{c}})\mathbf{V}^{\dagger}(\hat{\mathbf{c}}) \\ &\quad -\mathbf{V}(\hat{\mathbf{c}})\mathbf{F}(\hat{\mathbf{c}})\mathbf{A}^{\dagger}_b(\hat{c}_b)\mathbf{A}_b(\hat{c}_b)\mathbf{F}(\hat{\mathbf{c}})\mathbf{V}^{\dagger}(\hat{\mathbf{c}}) \\ &\quad -\mathbf{V}(\hat{\mathbf{c}})\mathbf{F}(\hat{\mathbf{c}})\mathbf{B}_b(\hat{\mathbf{c}})\mathbf{F}(\hat{\mathbf{c}})\mathbf{B}_b(\hat{\mathbf{c}})\mathbf{F}(\hat{\mathbf{c}})\mathbf{V}^{\dagger}(\hat{\mathbf{c}}) \\ &\quad +j\Big(\mathbf{Z}\mathbf{A}_b(\hat{c}_b)\mathbf{F}(\hat{\mathbf{c}})\mathbf{V}^{\dagger}(\hat{\mathbf{c}}) + \mathbf{V}(\hat{\mathbf{c}})\mathbf{F}(\hat{\mathbf{c}})\mathbf{A}^{\dagger}_b(\hat{c}_b)\mathbf{Z} \\ &\quad -\mathbf{V}(\hat{\mathbf{c}})\mathbf{F}(\hat{\mathbf{c}})\mathbf{V}^{\dagger}(\hat{\mathbf{c}})\mathbf{Z}\mathbf{A}_b(\hat{c}_b)\mathbf{F}(\hat{\mathbf{c}})\mathbf{V}^{\dagger}(\hat{\mathbf{c}}) \\ &\quad -\mathbf{V}(\hat{\mathbf{c}})\mathbf{F}(\hat{\mathbf{c}})\mathbf{A}^{\dagger}_b(\hat{c}_b)\mathbf{Z}\mathbf{V}(\hat{\mathbf{c}})\mathbf{F}(\hat{\mathbf{c}})\mathbf{V}^{\dagger}(\hat{\mathbf{c}})\Big). \end{aligned} \tag{4.24}$$

The complexity of these expressions for the Hessian arises from the presence of an inverse matrix in $\mathbf{G}(\mathbf{c})$ and the nature of the dependence of $\mathbf{V}(\mathbf{c})$ itself on $\mathbf{c}$. The difference between the diagonals and off-diagonals is due to the partial derivative of $\frac{\partial}{\partial \hat{c}_b}\mathbf{A}_b(\hat{c}_b) = j\mathbf{Z}\mathbf{A}_b(\hat{c}_b)$, whereas $\frac{\partial}{\partial \hat{c}_l}\mathbf{A}_b(\hat{c}_b) = \mathbf{0}$. The actual computation load is smaller than (4.16)-(4.24) suggest, since only a fraction $1/B$ of the columns of $\mathbf{A}$ are non-zero, and many partial computations can be saved and re-used. Further, as covered in Section 4.5, the Hessian does not vary much in the convex space, and can be pre-calculated for a range of CFO values without sacrificing estimator performance.

The following section covers an alternative metric that relies on channel marginalization instead of LS channel gain estimation.

4.3 Marginalization of CSI

In this section, a channel gain marginalized version of the ML metric is formed in the presence of CFO. Channel marginalization is used as an alternative to the LS channel estimation and back substitution that is used in (4.8) to (4.10). The resulting metric is more robust than (4.10), in that it can operate with linearly dependent TSs at each BS.

The channel gain marginalization can be stated as follows. Starting with the pdf from (4.6), the optimum joint ML solution is found as

$$\arg\max_{\mathbf{h},\mathbf{c}} p(\mathbf{y}|\mathbf{h},\mathbf{c}). \tag{4.25}$$

However, if the channel pdf can be expressed as $p(\mathbf{h})$, the marginalized pdf can be formed as

$$p(\mathbf{y}|\mathbf{c}) = E_h\left[p(\mathbf{y}|\mathbf{h},\mathbf{c})\right], \tag{4.26}$$

with the CFO estimation problem becoming

$$\max_{\mathbf{c}} p(\mathbf{y}|\mathbf{c}). \tag{4.27}$$

There has been some previous work on channel marginalization of the conditional pdf for the single CFO case. Hebley and Taylor in [34] present a single CFO estimator in a single-input/multiple-output (SIMO) system that relies upon marginalization of the channel gains. As in [11], Hebley and Taylor focus on the effect of antenna diversity. Also, in [20], Deng et al. deal with marginalization of correlated MIMO channels.

The novelty of the channel marginalization presented here lies in the inclusion of the multiple CFOs of a MIMO system. The full details of the channel gain marginalization are found in Appendix B. The pdf of the received samples after marginalization of the channel gains is

$$p\left(\mathbf{y}|\mathbf{c}\right) = \frac{|\mathbf{B}|}{(2\pi)^{NN_R}\, NN_R} \exp\left(-\frac{\mathbf{y}^\dagger\left(\mathbf{I}_{NN_R} - \overline{\mathbf{V}}(\mathbf{c})\mathbf{B}\mathbf{B}^\dagger\overline{\mathbf{V}}^\dagger(\mathbf{c})\right)\mathbf{y}}{2N_0}\right), \tag{4.28}$$

where $\mathbf{B} = \left(\mathbf{\Xi}\mathbf{Q}^\dagger\right)^{-1}$ and $\mathbf{\Xi}$ and $\mathbf{Q}$ come from the eigendecomposition of $\overline{\mathbf{V}}^\dagger(\mathbf{c})\overline{\mathbf{V}}(\mathbf{c}) + N_0\mathbf{I}_{BN_RN_T}$.

The ML metric can be found as follows. First, the log of (4.28) is taken. Discarding any constant terms, and noting that $2N_0 \log\left|\mathbf{\Xi}\mathbf{Q}^\dagger\right| = N_0 \log\left|\overline{\mathbf{V}}^\dagger(\mathbf{c})\overline{\mathbf{V}}(\mathbf{c}) + N_0\mathbf{I}_{BN_RN_T}\right|$, the new

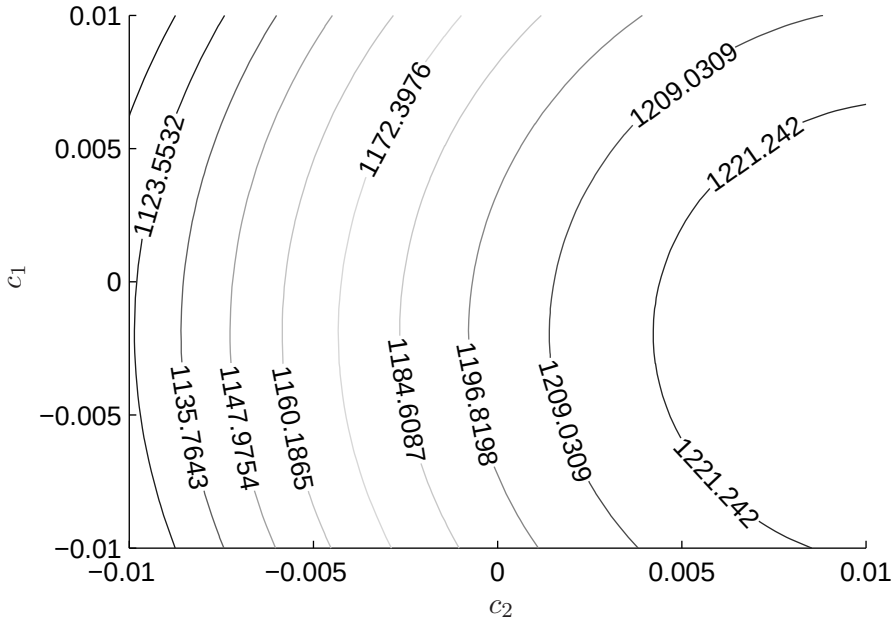

Figure 4.2: $\Lambda(\mathbf{c})$ contours, from (4.10); $c_1 = -0.0001$, $c_2 = 0.0080$, $N = 64$, $\Gamma_{BS} = 10$dB, $B = 2$, $c_{max} = 10^{-2}$, $N_R = 2$, $N_T = 2$.

CSI marginalized ML metric is

$$\begin{aligned}\Lambda_{marg}(\mathbf{c}) &= \mathbf{y}^{\dagger}\overline{\mathbf{V}}(\mathbf{c})\left(\overline{\mathbf{V}}^{\dagger}(\mathbf{c})\overline{\mathbf{V}}(\mathbf{c}) + N_0\mathbf{I}_{BN_RN_T}\right)^{-1}\overline{\mathbf{V}}^{\dagger}(\mathbf{c})\mathbf{y} \\ &\quad -N_0\log\left|\overline{\mathbf{V}}^{\dagger}(\mathbf{c})\overline{\mathbf{V}}(\mathbf{c}) + N_0\mathbf{I}_{BN_RN_T}\right|,\end{aligned} \tag{4.29}$$

with the ML solution

$$\hat{\mathbf{c}} = \arg\max_{\mathbf{c}} \Lambda_{marg}(\mathbf{c}). \tag{4.30}$$

The difference between the marginalized metric in (4.29) and the original metric in (4.10) lies in the addition of the log-determinant term and the noise PSD N_0 in the inverse matrix. Considering the log-determinant term, observation of the metric surface for $B = 2$ shows that the log-determinant addition does not significantly alter the search space, as it has very little dynamic range across all CFO values. This is seen by comparing $\Lambda(\mathbf{c})$, which converges asymptotically to the first term of $\Lambda_{marg}(\mathbf{c})$ in high SNR, to $N_0\log\left|\overline{\mathbf{V}}^{\dagger}(\mathbf{c})\overline{\mathbf{V}}(\mathbf{c}) + N_0\mathbf{I}_{BN_RN_T}\right|$ in Figures 4.2 and 4.3, respectively. In these simulations for $\Gamma_{BS} = 10$dB, the range of $\Lambda(\mathbf{c})$ is ≈ 97.69 compared to $N_0\log\left|\overline{\mathbf{V}}^{\dagger}(\mathbf{c})\overline{\mathbf{V}}(\mathbf{c}) + N_0\mathbf{I}_{BN_RN_T}\right|$ where the range is ≈ 0.0008. As for the addition of the noise term in the inverse, note that the marginalized metric does not

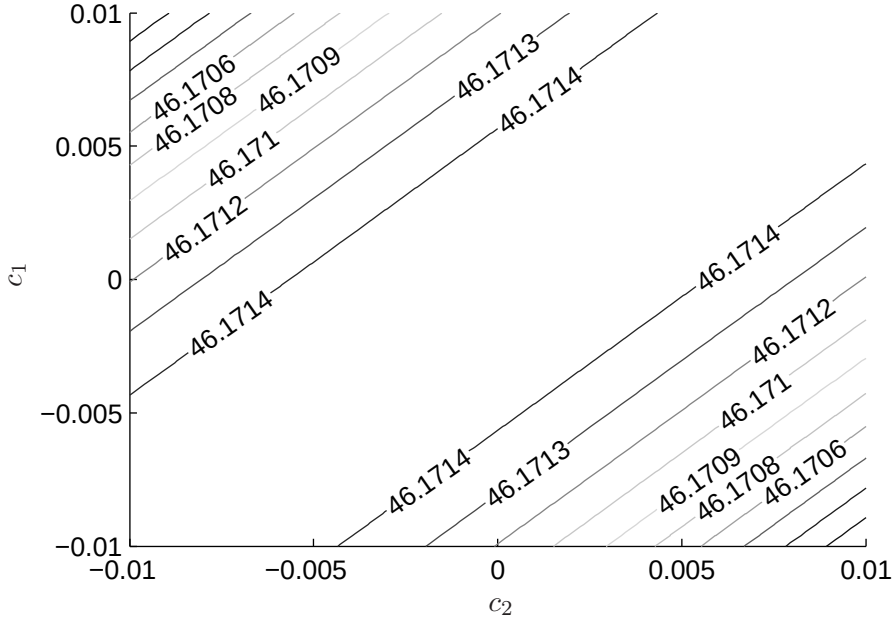

Figure 4.3: $N_0 \log \left| \overline{\mathbf{V}}^{\dagger}(\mathbf{c})\overline{\mathbf{V}}(\mathbf{c}) + N_0 \mathbf{I}_{BN_T} \right|$ contours; $c_1 = -0.0001$, $c_2 = 0.0080$, $N = 64$, $\Gamma_{BS} = 10$dB, $B = 2$, $c_{max} = 10^{-2}$, $N_R = 2$, $N_T = 2$.

require $\overline{\mathbf{V}}^{\dagger}(\mathbf{c})\overline{\mathbf{V}}(\mathbf{c})$ to be full rank as the original metric does. Specifically, CFO estimation is still possible even in the case that all N_T antennas at a single BS transmit identical TSs. In order to distinguish between BS CFOs, the TSs of different BSs must still be linearly independent.

This metric and its ability to cope with dependent TSs may prove useful for periodic CFO estimate updates. In systems where the number of downlink antennas BN_T is very high, the number of available TSs N_{TS} may not be adequate to provide a linear independent sequence for each antenna, as $N_{TS} \geq BN_T$. For the purposes of CFO estimation, the same TS can be used at each of the N_T antennas of a given BS, reducing the requirement to $N_{TS} \geq B$. However, for the purposes of CSI estimation, linear independence of all TSs is still required.

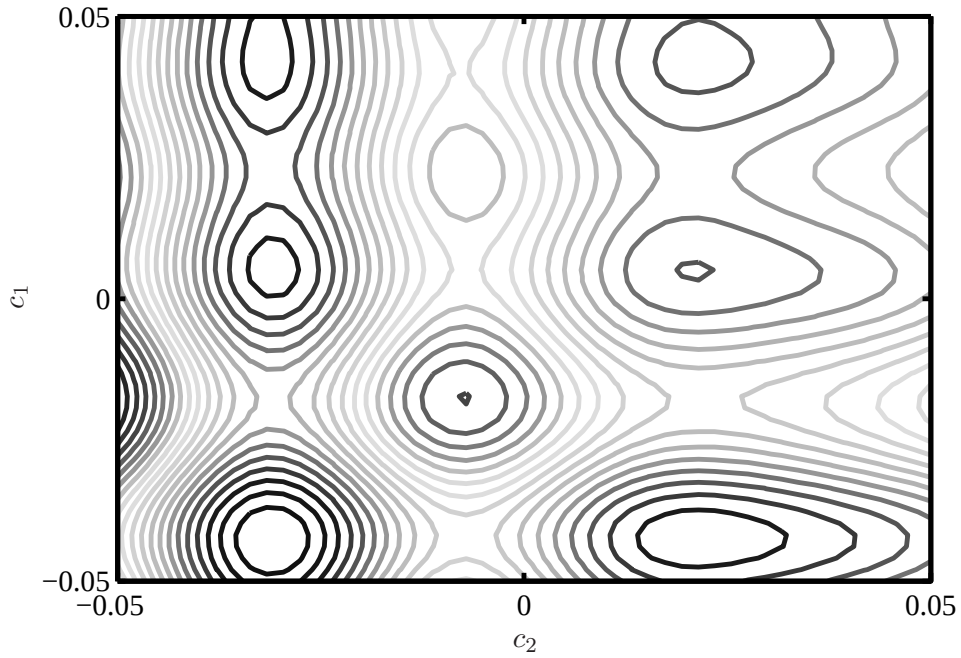

Figure 4.4: $\Lambda(\mathbf{c})$ contours; $N = 200$, SNR = 0 dB, $B = 2$, $N_R = 2$, $N_T = 2$.

4.4 Restrictions on Training Length

The prerequisite for reliable use of the Gradient descent or Newton method is assurance that $\Lambda(\mathbf{c})$ is convex over the search domain. The search domain is defined by the box constraints $|c_b| \leq c_{max}$. If the TS length N is large enough, aliasing of $\Lambda(\mathbf{c})$ could occur, causing loss of convexity and even allowing secondary maxima in the search domain. If the maximum CFO is known *a priori*, a limit can be imposed on N to avoid loss of convexity. With symbols drawn from a constant envelope constellation, the duration NT_s of a TS determines its frequency resolution. The Fourier transform of the TS can be well approximated as being proportional to $\text{sinc}(fNT_s)$, or $\text{sinc}(Nc/2\pi)$, for small arguments. The same is true of $\Lambda(\mathbf{c})$, which has been verified numerically. The first inflection point of $\text{sinc}(x)$ is 0.66, which we round down to 0.5 to be conservative, so $2Nc_{max}/2\pi \leq 0.5$. The factor of 2 in the numerator accounts for non-positive CFO, since $c_b \in [-c_{max}, +c_{max}]$. Solving for N results in

$$N < \pi/2c_{max}. \tag{4.31}$$

Ultimately, some situations may demand longer TSs in order to achieve a specific estimator variance, so that the bound (4.31) is violated. For such cases, the search space for

large values of N and c_{max} can be highly irregular. As shown in Figure 4.4 for a system with $B = 2$, $c_{max} = 0.05$ and a low SNR of 0 dB, several local maxima within the search region can result from exceeding the bound in (4.31). This poses problems to techniques that rely upon a convex objective function.

In the following, two extensions to the convex ST estimators from Sections 4.2.1 and 4.2.2 are presented, termed the telescoping estimator (TE) and the combining estimator (CE). Since both techniques rely upon breaking the length-N TS into shorter sections, they are referred to collectively as segmented estimators (SE). The segments are chosen to be just short enough to ensure convexity (i.e., to satisfy the constraint in (4.31)). The ST-G or ST-N estimators of Sections 4.2.1 and 4.2.2 can be used within each segment, although with different (shorter) sequences $\mathbf{X}$. In the rest of this Chapter, only the ST-N is treated, because of its superior rate of convergence; the ST-G technique could be substituted by replacing the appropriate step function. We assume that the shortened sequences in $\mathbf{V}(\mathbf{c})$, although not orthogonal, still have full column rank for the CSI estimation.

A brief overview of the SE techniques are as follows. Both SE techniques are iterative and thus have multiple stages. After each stage, the reduced standard deviation improves the knowledge of $\mathbf{c}$, and permits a reduced search space in $\Lambda(\hat{\mathbf{c}})$. This in turn allows longer segments in the next stage, until the segment in the final stage is the entire TS. In this way, the SEs can use long TSs, with their large aperture and energy, and still find the global maximum.

Within each segment, the TS fragments must be linearly independent to allow the matrix inversion in LS estimation of the CSI. This consideration may be avoided to some degree if the marginalized metric in Section 4.3 were used instead. Orthogonality within the segments is of lesser concern, since the full-length TSs, on which the final estimates are based, have low cross-correlation.

To illustrate the utility of the segmented estimators, the following example shows the surface of $\Lambda(\mathbf{c})$ and how it changes with the number of training symbols. Figures 4.5 and 4.6 show $\Lambda(\mathbf{c})$ for a system with $B = 2$ and $c_{max} = 0.02$. For the sake of example, we require $\Gamma_{TS} = 1024$, so for $N_0 = 1$, $E_{TS} = 1024$ J. Assuming a maximum per symbol transmit energy of $E_b = 1$ J as a result of amplifier restrictions, the required TS length will be $N = 512$. Applying the relation in (4.20), we get $N = 512 > \pi/2(0.02) = 79$, which means that $\Lambda(\mathbf{c})$ is not convex for the full TS. This can be seen in Figure 4.5 from the contour ledge in the centre-right of the graph. By only using the first 64 symbols of the TS,

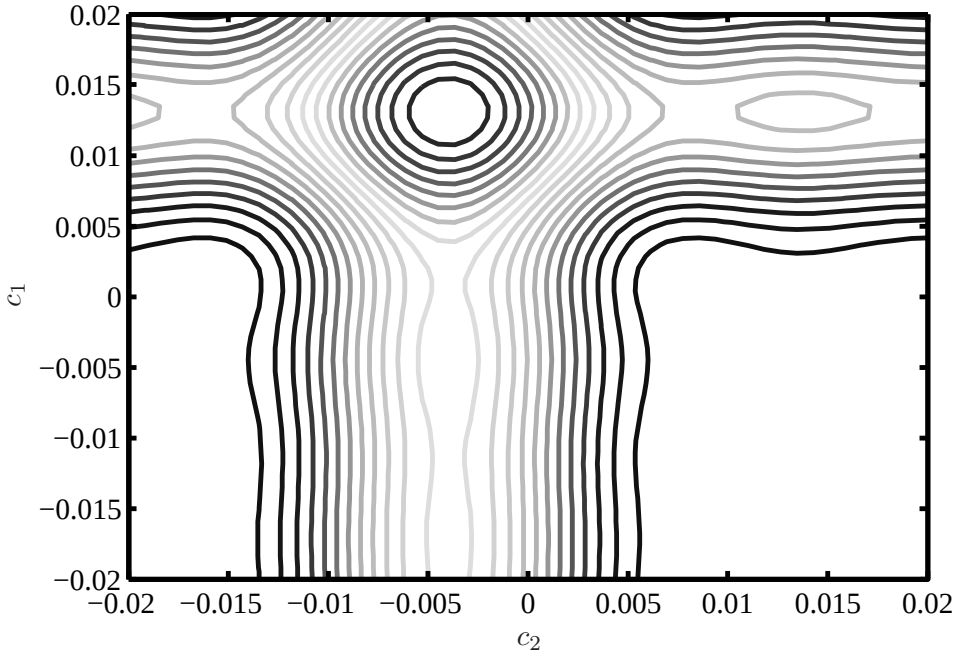

Figure 4.5: $\Lambda_{ST-TE-N}(\mathbf{c})$ contours; $N = 512$, $c_1 = 0.0131$, $c_2 = -0.0040$, SNR = 30 dB, $B = 2$, $N_R = 2$, $N_T = 2$.

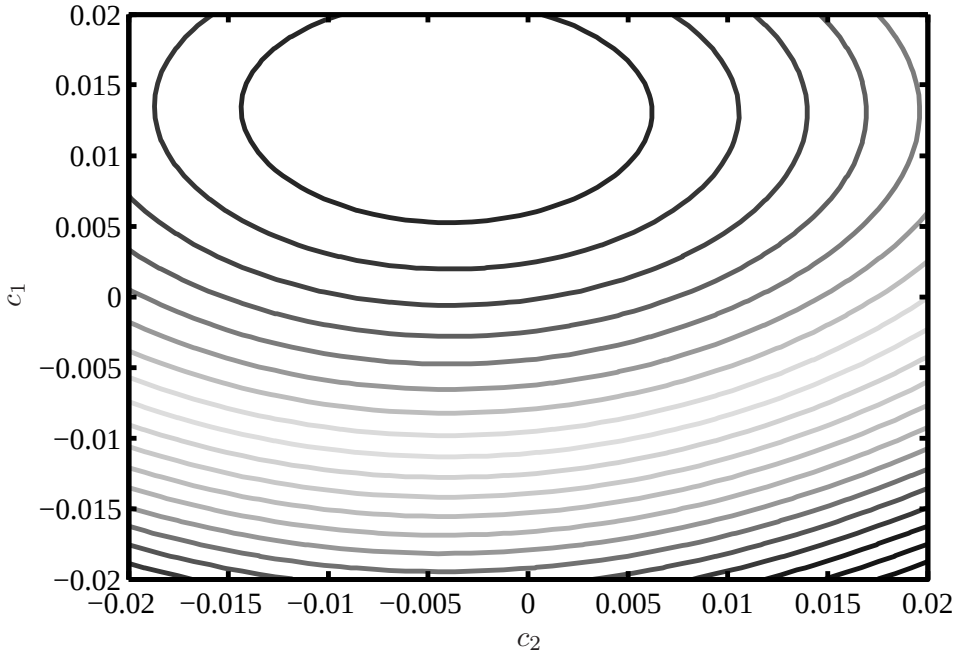

Figure 4.6: $\Lambda_{ST-TE-N}(\mathbf{c})$ contours for first 64 training symbols; $N = 512$, $c_1 = 0.0131$, $c_2 = -0.0040$, SNR = 30 dB, $B = 2$, $N_R = 2$, $N_T = 2$.

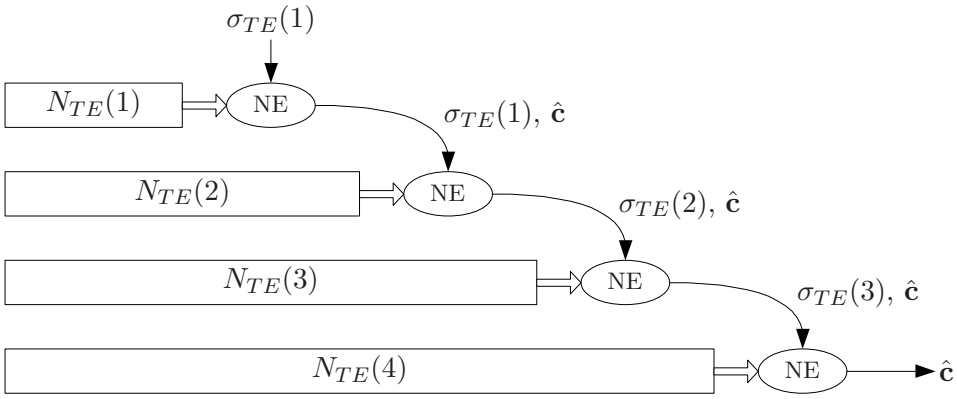

Figure 4.7: Telescoping estimator; NE = Newton estimator, 4 stages.

the problem is guaranteed to be convex. Figure 4.6 shows that the contours have effectively zoomed in on the global maximum by increasing the size of the main lobe. The trade-off is a loss in TS energy and resolution in return for convexity; these losses are made up for in later stages, as the segment lengths increase.

There are two main differences between the TE and CE estimators. First, for the CE estimator, the entire TS must be received before any processing can proceed. This is not necessary for the TE estimator, which can begin processing once a certain number of symbols have been received. Second, since the CE estimator makes use of the entire TS simultaneously for every stage, it will provide a higher quality estimate.

4.4.1 Telescoping Technique

The TE estimator is based on breaking the TS into successive segments of increasing length, as shown in Figure 4.7. For the s^{th} stage, $N_{TE}(s)$ training symbols are used by the ST-N technique. For the first stage, the number of training symbols used in the ST-N technique is based on the convexity constraint (4.20), so $N_{TE}(1) = \lfloor \pi/2c_{max} \rfloor$, where $\lfloor \cdot \rfloor$ represents the floor function. The CFO estimate $\hat{\mathbf{c}}(1)$ is made after convergence, followed by an estimate of the standard deviation of $\hat{\mathbf{c}}(1)$, calculated from the CRLB as in Section 4.4.3. This standard deviation, denoted $\sigma_{TE}(s)$ after stage s, is then used to reduce the CFO search range for the subsequent stage. To provide room for channel and noise variations, we use $5\sigma_{TE}$ to calculate N_{TE}, so $N_{TE}(s+1) = \pi/10\sigma_{TE}(s)$. During the second stage, the algorithm will calculate a second estimate using $N_{TE}(2)$ symbols, and so on, until the entire TS is received and processed as a whole. To ensure the search space remains convex, the range for $\hat{c}_b(i,s)$

Table 4.1: Telescoping estimator.

$\hat{\mathbf{c}}(0,1) = \mathbf{0}$
$s = 1$
$\sigma_{TE}(s) = c_{max}$
$N_{TE}(s) = \lfloor \frac{\pi}{2\sigma_{TE}(s)} \rfloor$
while $N_{TE}(s) \leq N$
  for $i = 1$ to N_{ITER}
    $\hat{\mathbf{c}}(i,s) = \hat{\mathbf{c}}(i-1,s) - \boldsymbol{\mu}_{TE}\left(\hat{\mathbf{c}}(i-1,s)\right)$
    if $|\hat{c}_b(i,s) - \hat{c}_b(0,s)| > \sigma_{TE}(s)$, $\hat{c}_b(i,s) = \hat{c}_b(i-1,s) \pm \sigma_{TE}(s) \ \ \forall b$
  end
  $s = s + 1$
  $\hat{\mathbf{c}}(0,s) = \hat{\mathbf{c}}(N_{ITER}, s-1)$
  $\sigma_{TE}(s) = 5\sigma_{\hat{\mathbf{c}}}(s,\Gamma)$
  $N_{TE}(s) = \lfloor \frac{\pi}{2\sigma_{TE}(s)} \rfloor$
end

at the s^{th} stage and i^{th} Newton iteration is restricted to $\hat{c}_b(0, s-1) \pm \sigma_{TE}(s)$. Table 4.1 details the algorithm. The process of determining the standard deviation of the estimate $\sigma_{TE}(s)$ will be explained in Section 4.4.3.

The TE Newton step is defined as

$$\boldsymbol{\mu}_{TE}(\mathbf{c}, s) = \left[\bigtriangledown^2 \Lambda_{TE}(\mathbf{c}, s)\right]^{-1} \bigtriangledown \Lambda_{TE}(\mathbf{c}, s). \tag{4.32}$$

The expression $\Lambda_{TE}(\mathbf{c}, s)$ refers to replacing the vector $\mathbf{y}$ and matrix $\mathbf{X}$ in (4.15)-(4.24) with

$$\mathbf{y}_{TE}\left(N_{TE}(s)\right) = \mathcal{I}\left(N_{TE}(s), N_R\right)\mathbf{y} \tag{4.33}$$

and

$$\mathbf{X}_{TE}\left(N_{TE}(s)\right) = \mathcal{I}\left(N_{TE}(s), 1\right)\mathbf{X}, \tag{4.34}$$

respectively, where $\mathcal{I}\left(N_{TE}(s), N_R\right) = \mathbf{I}_{N_R} \otimes \left[\mathbf{I}_{N_{TE}(s)} \ \mathbf{0}_{N-N_{TE}(s)}\right]$. This simply denotes selecting the first $N_{TE}(s)$ samples from each receive antenna. In Table 4.1, the line after the Newton update is used to ensure that $\hat{\mathbf{c}}$ stays within the boundaries of the convex search space.

The number of stages necessary to calculate an estimate is variable because $\sigma_{TE}(s)$ is dependent on the SNR, B, N_T, and N_R, as well as the TS sequences themselves. However,

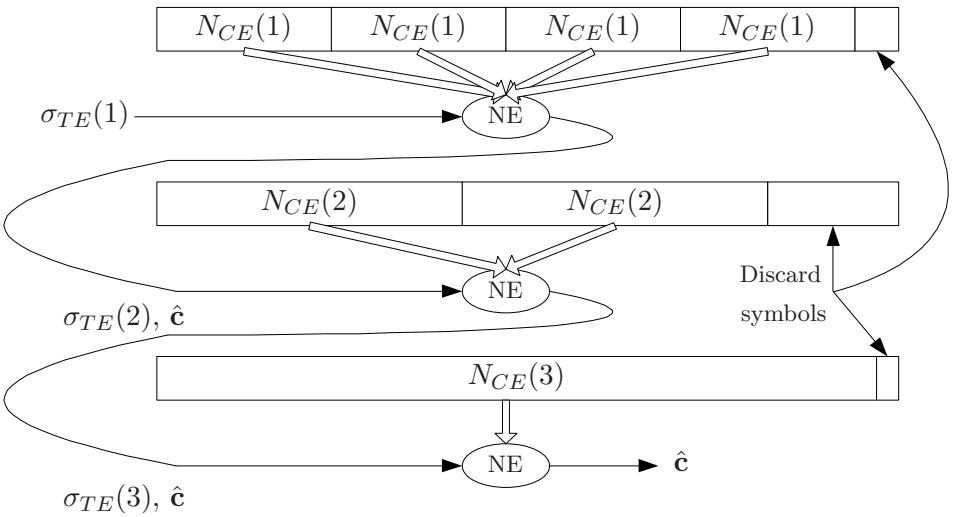

Figure 4.8: Combining estimator; NE = Newton estimator, 3 stages.

the complexity of the TE can be calculated, since an approximate $\sigma_{TE}(s)$ is pre-calculated and used from a look-up table (Section 4.4.3).

4.4.2 Combining Technique

The CE estimator uses the entire TS at each stage s by combining its $L_{CE}(s)$ equal-length segments incoherently, as illustrated in Figure 4.8. Because of this, the entire sequence must be received before starting the estimation process. As in the TE, the CE will begin with $N_{CE}(1) = \lfloor \pi/2c_{max} \rfloor$, where $N_{CE}(s)$ refers to the segment length for the s^{th} stage. This gives $L_{CE}(s) = \lfloor N/N_{CE}(s) \rfloor$ segments at stage s. Unlike the TE, which uses the first $N_{CE}(s)$ training symbols, the CE estimator adds the log-likelihoods from all segments of the TS to form an overall log-likelihood. Summing the segmented log-likelihoods follows from use of incoherent combining, by which we mean allowing different channel gains $\mathbf{h}_u$, $u = 1, \cdots, L_{CE}(s)$ in different segments. Then the log-likelihood equivalent to (4.7) is expressible as a sum, with the u^{th} term a function of $\mathbf{c}$ and $\mathbf{h}_u$. The joint optimization equivalent to (4.9) replaces each $\mathbf{h}_u$ with its LS estimate, resulting in an overall log-likelihood that is a sum of segmented log-likelihoods, each a function of $\mathbf{c}$. It remains convex in $\mathbf{c}$, since each of the terms is convex.

In effect, each segment is allowed its own set of amplitudes and phases in the CSI gains $\mathbf{h}$. The gradient and Hessian functions are the sum of the gradients and Hessians of the

Table 4.2: Combining estimator.

$\hat{\mathbf{c}}(0,1) = \mathbf{0}$
$s = 1$
$\sigma_{CE}(s) = c_{max}$
$N_{CE}(s) = \lfloor \frac{\pi}{2\sigma_{CE}(s)} \rfloor$
while $N_{CE}(s) \leq N$
  for $i = 1$ to N_{ITER}
    $\hat{\mathbf{c}}(i,s) = \hat{\mathbf{c}}(i-1,s) - \boldsymbol{\mu}_{CE}\left(\hat{\mathbf{c}}(i-1,s)\right)$
    if $|\hat{c}_b(i,s) - \hat{c}_b(0,s)| > \sigma_{CE}(s)$, $\hat{c}_b(i,s) = \hat{c}_b(i-1,s) \pm \sigma_{CE}(s)$, $\forall b$
  end
  $s = s + 1$
  $\hat{\mathbf{c}}(0,s) = \hat{\mathbf{c}}(N_{ITER}, s-1)$
  $\sigma_{CE}(s) = 5\sigma_{\hat{\mathbf{c}}}(s,\Gamma)$
  $N_{CE}(s) = \lfloor \frac{\pi}{2\sigma_{CE}(s)} \rfloor$
end

segments, and are used to calculate the CE Newton step. The segment sizes in $N_{CE}(s)$ are calculated in the same manner as for the TE estimator (Section 4.4.1).

The Newton step for the CE estimator is

$$\boldsymbol{\mu}_{CE}(\mathbf{c},s) = \left[\bigtriangledown^2 \Lambda_{CE}(\mathbf{c},s)\right]^{-1} \bigtriangledown \Lambda_{CE}(\mathbf{c},s). \tag{4.35}$$

The gradient of the s^{th} stage of the CE estimator is

$$\frac{\partial}{\partial c_b}\Lambda_{CE}(\mathbf{c},s) = \sum_{u=1}^{L_{CE}(s)} \mathbf{y}_u^\dagger \Big[\overline{\mathbf{G}}_b'(\mathbf{c},u)\Big]\mathbf{y}_u, \tag{4.36}$$

where $\mathbf{y}_u = \mathcal{I}(N_{CE}(s),1,u)\mathbf{y}$ is the u^{th} block of received samples and $\mathcal{I}(N_{CE}(s),N_R,u) = \mathbf{I}_{N_R} \otimes \left[\mathbf{0}_{(u-1)N_{CE}(s)}\ \mathbf{I}_{N_{CE}(s)}\ \mathbf{0}_{N-uN_{CE}(s)}\right]$. The modified $\mathbf{G}_b'(\mathbf{c},u)$ is created by replacing $\mathbf{X}$ with $\mathbf{X}_u = \mathcal{I}(N_{CE}(s),N_R,u)\mathbf{X}$. The (b^{th},l^{th}) Hessian is created in the same manner, with

$$\frac{\partial^2}{\partial c_b \partial c_l}\Lambda_{CE}(\mathbf{c},s) = \sum_{u=1}^{L_{CE}} \mathbf{y}_u^\dagger \Big[\overline{\mathbf{G}}_{b,l}''(\mathbf{c},u)\Big]\mathbf{y}_u, \tag{4.37}$$

where the modified $\mathbf{G}_{b,l}''(\mathbf{c},u)$ is also created by replacing the TS $\mathbf{X}$ with $\mathbf{X}_u$. Table 4.2 details the algorithm.

The CE is expected to have a lower estimator variance since it makes use of the entire sequence throughout the segmented process, unlike the TE estimator, which only uses information as it arrives. Also note that since we use the floor function on $L_{CE}(s)$, there are samples that are neglected. In our numerical results, we simply ignored any leftover symbols.

The following section provides a means to calculate approximate values for the estimator variance that are used for the SE techniques.

4.4.3 SE Accuracy

In this section, the CRLB for the MS-side estimator for multiple CFOs in a coordinated CMBMU system is derived. We use the CRLB in two ways. The first is as an analytical expression for the high-SNR performance of the ST-N method, as well as a check on the performance obtained in simulations. The second is as a way to approximate (or lower bound) the achieved standard deviation in each segment of the ST-N-TE and ST-N-CE segmented methods. As outlined previously, these standard deviations allow determination of the segment lengths for the subsequent stage.

In [6], the CRLB was found for multiple CFOs resulting from independent multipath. The system model allowed the Fisher information matrix (FIM) to consist of block diagonal components, one for each receive antenna. In the coordinated system presented here, the number of CFOs is independent of the number of receive antennas, and the CRLB must be reformulated.

The details of the derivation can be found in Appendix A. The estimate vector for the joint estimation of the channel states and the CFOs is defined as

$$\boldsymbol{\eta} = \left[\boldsymbol{\eta}_1^T \cdots \boldsymbol{\eta}_{N_R}^T \;\; \mathbf{c}^T\right]^T \in \mathcal{R}^{2BN_TN_R+B\times 1}, \tag{4.38}$$

where $\boldsymbol{\eta}_q = [Re(\mathbf{h}_q)^T \;\; Im(\mathbf{h}_q)^T]^T \in \mathcal{R}^{2BN_T\times 1}$ and $\mathbf{c} = [c_1 \cdots c_B]^T \in \mathcal{R}^{B\times 1}$. The vector of transmitted symbols after distortion by the CFOs, $\mathbf{u}$, is formed as

$$\mathbf{u}(\mathbf{c}) = [\mathbf{u}_1^T(\mathbf{c}) \cdots \mathbf{u}_{N_R}^T(\mathbf{c})]^T \in \mathcal{C}^{NN_R\times 1}, \tag{4.39}$$

where $\mathbf{u}_q(\mathbf{c}) = \mathbf{V}(\mathbf{c})\mathbf{h}_q$.

The FIM is defined as

$$\mathbf{F} = \begin{bmatrix} \mathbf{F}_H(1,1) & \cdots & \mathbf{0} & \mathbf{F}_{Hc}(1) \\ \vdots & \ddots & \vdots & \vdots \\ \mathbf{0} & \cdots & \mathbf{F}_H(N_R,N_R) & \mathbf{F}_{Hc}(N_R) \\ \mathbf{F}_{cH}(1) & \cdots & \mathbf{F}_{cH}(N_R) & \mathbf{F}_c \end{bmatrix}, \tag{4.40}$$

where $\mathbf{F}_H(k,k)$, $\mathbf{F}_{cH}(k)$, $\mathbf{F}_{Hc}(k)$, and $\mathbf{F}_c$ are shown in Appendix A. Using the matrix inversion lemma on the FIM in (4.40), the CRLB for the estimation error covariance matrix is

$$\mathbf{CRLB}_c = \left(\mathbf{F}_c - \mathbf{F}_{cH}\mathbf{F}_H^{-1}\mathbf{F}_{Hc}\right)^{-1}. \tag{4.41}$$

The success of the segmented estimators in Sections 4.4.1 and 4.4.2 at keeping the global maximum within the search domain is dependent upon the accuracy of the standard deviation, e.g. $\sigma_{TE}(s)$, estimated after each stage. For this, we set the standard deviation equal to the value obtained from the CRLB; from the trace of (4.41), we have $\sigma^2_{\hat{\mathbf{c}}} = trace\left(\mathbf{CRLB}_c\right)/B$. To be conservative, we then set the box constraints on the search domain as $|c_b - \hat{c}_b(s)| \leq 5\sigma_{\hat{\mathbf{c}}}$. This loose constraint maintains convexity of $\Lambda(\mathbf{c})$ with very high probability.

However, note that (4.41) depends on the channel $\mathbf{h}$, which in principle is unknown. We have two choices: we can substitute the ML estimate (4.9), or we can average (4.41) over many channel realizations in Monte Carlo simulation. For two antennas at each of the BSs and the MS, the latter turned out to be adequate. In addition, $\sigma_{\hat{\mathbf{c}}}$ will vary depending on the TS length. Therefore, a matrix of values of $N_{TE}(s)$ is pre-calculated based on SNR and TS length, as $\sigma_{\hat{\mathbf{c}}}(s,\Gamma)$, where Γ refers to the SNR. Table 4.3 shows an example of how $\sigma_{\hat{\mathbf{c}}}(s,\Gamma)$ is related to segment lengths $N_{TE}(s)$. The values for $N_{TE}(s)$ are calculated using the CRLB; first, $\sigma_{\hat{\mathbf{c}}}$ is found via simulation, then (4.31) is used to calculate $N_{TE}(s)$.

4.5 Complexity

The complexity of the techniques is estimated as the number of complex multiply and add (CMA) operations necessary for a single estimate of the B CFOs. The results are asymptotic in N, since the TS length is the limiting variable in complexity. Table 4.4 compares the CMAs for ST-AO, TO, ST-N, ST-N-TE, ST-N-CE and brute force. For ST-AO, TO and brute force, the domain of the CFOs is broken into N bins.

Table 4.3: Look-up table for $N_{TE}(s)$, where $N_{TE}(s)$ is chosen to ensure that convexity of $\Lambda(\mathbf{c}, s)$ is maintained; $B = 4$, $N = 128$ BPSK Hadamard TS, $c_{max} = 5 \times 10^{-2}$.

$\frac{E_{BS}}{N_T N_0}$	$s = 1$	$s = 2$	$s = 3$	$s = 4$
-20 dB	31	-	-	-
-15 dB	31	-	-	-
-10 dB	31	-	-	-
-5 dB	31	-	-	-
0 dB	31	-	-	-
5 dB	31	46	86	128
10 dB	31	83	128	-
15 dB	31	128	-	-
20 dB	31	128	-	-
25 dB	31	128	-	-
30 dB	31	128	-	-
35 dB	31	128	-	-
40 dB	31	128	-	-

Table 4.4: Complexity comparison.

Estimator	**Approx. CMA**
ST-AO	$BN_R N_T \left(2N + N\log_2(N)\right) + BN$
TO	$N_R N_T \left(2N + N\log_2(\frac{N}{B})\right) + BN$
ST-N	$N_{ITER}\left[B^3 + B^2 + BN^2\left(N_R^2 + 2BN_T\right)\right.$ $\left. + \frac{1}{2}B^2N^2N_R^2 + 5B^3N^2N_T + 4B^2N^2N_T\right]$
ST-N-TE	$\sum_{s=1}^{S} N_{ITER}\left[B^3 + B^2 + BN_{TE}^2(s)N_R^2\right.$ $+BN_{TE}^2(s)2BN_T + \frac{1}{2}B^2N_{TE}^2(s)N_R^2$ $\left. +5B^3N_{TE}^2(s)N_T + 4B^2N_{TE}^2(s)N_T\right]$
ST-N-CE	$\sum_{s=1}^{S} N_{ITER}\left[B^3 + B^2 + L_{CE}(s)BN_{CE}^2(s)N_R^2\right.$ $+L_{CE}(s)BN_{CE}^2(s)2BN_T + \frac{L_{CE}(s)}{2}B^2N_{CE}^2(s)N_R^2$ $\left. +L_{CE}(s)\left(5B^3N_{CE}^2(s)N_T + 4B^2N_{CE}^2(s)N_T\right)\right]$
Brute Force	$N^B\left(B^3N_R^3N_T^3 + 2N^2N_R^2\right) + N^B$

Table 4.5: Comparison of ST-N CFO MSE using pre-calculated Hessians, averaged over 100 Monte Carlo realizations; $B = 4$, $N_R = 2$, $N_T = 2$, $c_{max} = 10^{-2}$, $N = 128$ BPSK Hadamard TS, $N_{ITER} = 3$.

	$(N_{bins})^B$	$\frac{E_{BS}}{N_0} = 0$ **dB**	$\frac{E_{BS}}{N_0} = 20$ dB	$\frac{E_{BS}}{N_0} = 40$ dB
Hessian, $N_{bins} = \infty$	-	2.04×10^{-6}	2.07×10^{-8}	1.41×10^{-10}
Hessian, $N_{bins} = 10$	10^4	1.80×10^{-6}	1.71×10^{-8}	1.70×10^{-10}
Hessian, $N_{bins} = 4$	256	1.70×10^{-6}	2.02×10^{-8}	1.63×10^{-10}
Hessian, $N_{bins} = 2$	16	1.05×10^{-5}	2.49×10^{-8}	2.06×10^{-9}

The variable S used for ST-N-TE and ST-N-CE in Table 4.4 refers to the number of stages necessary for the algorithm to converge to $N_{TE}(s) = N$ and $N_{CE}(s) = N$. As explained in the Section 4.4 and Table 4.3, this is dependent on the SNR; medium SNR will require $S > 2$ while high SNR will require only $S = 2$. Note that in Table 4.3, the value of $N_{TE}(1)$ and $N_{CE}(1)$ is always set to $\lfloor \pi/2c_{max} \rfloor$ to ensure convexity for the Newton method.

The ST-N, ST-N-TE and ST-N-CE algorithms have a significant contribution from the calculation of the Hessian, which consists of the last two terms for each technique in Table 4.4. However, since the Hessian does not vary much in the convex space that is guaranteed in these estimators, this can be pre-calculated for a range of CFO values to reduce computations. To do this, the input CFO to the Hessian is approximated into one of N_{bins} discrete values. One of $(N_{bins})^B$ stored Hessian matrices is then used to calculate the Newton step. To show the effectiveness of this approximation, Table 4.5 lists the resulting ST-N CFO MSE for different values of N_{bins}. Even with as few as 4 bins across the domain $[-c_{max}, +c_{max}]$, requiring storage of 256 Hessian matrices for the case of $B = 4$, the effect on the performance of ST-N is negligible.

Also, matrix sparsity presents opportunities for further reduction to the number of CMAs, particularly with the $\mathbf{A}_b(\hat{c}_b)$ matrix and the Kronecker products.

4.6 Accounting for Symbol Asynchronous and Frequency Selective Channels

Modification of the metric presented in the previous section to accommodate asynchronous arrivals and frequency selectivity is straightforward. The oversampled model in (2.40) is

used, which has N_{ss} samples per symbol, which means a sample spacing T_s/N_{ss}. This sample spacing is applied to the arrays $\mathbf{y}^{(ss)}$, $\overline{\mathbf{V}}^{(ss)}(\mathbf{c})$ and $\mathbf{z}^{(ss)}$. With $N_{ss} > 1$, we are guaranteed Nyquist-rate sampling.

Interpolation, to account for asynchronicity, has the same form as delay spread, with a vector impulse response $\mathbf{h}_q^{(ss,l)}$ in (2.45), spanning LT_s/N_{ss} seconds. The expression for received samples is shown in (2.46). The CFO and CSI estimates can be performed in the same way as for synchronous, unspread signals. Also, any phase shifts incurred in the delayed $\overline{\mathbf{V}}^{(ss,l)}(\mathbf{c})$ will be absorbed into the channel estimates of $\mathbf{h}^{(ss)}$.

Note that for realistic channels, oversampling of the signals would require further modification of the pdf in (4.6). Since the pulse shapes used in the communication system (see Section 2.1.1) are non-zero at the sub-sampled intervals, sub-sampling will result in correlated noise. Any modifications to the pdf would be dependent on the specific pulse shape used for the training symbols, and would be reflected in the log-likelihood metric.

4.7 Results

In this section, the convex and segmentation methods developed above are compared to the existing methods of ST-AO and TO. The more qualitative metric of MSE is used to compare the techniques instead of an actual system BER. This is done to avoid dependence on a specific beamformer and modulation.

The simulation parameters are as follows. The components of the channel vector $\mathbf{h}$ and noise vector $\mathbf{z}$ are modeled as i.i.d. complex Gaussian random variable, with the channel gains assumed to be static over the entire TS. The TSs are BPSK Hadamard codes. The ST-AO and TO techniques rely upon a search over a range of CFO values, consisting of N frequency bins, suitable for the FFT. Monte Carlo simulations of 500 runs were used with a range of TS SNR levels. The CFO is random and uniformly distributed, with the CFO set to $c_b \in [-c_{max}, +c_{max}] \ \forall \ b$. The number of iterations used for ST-G was set to $N_{ITER} = 16$ and for ST-N was set to $N_{ITER} = 3$.

For TO, the TS length was reduced by B to keep the total length equal between the estimators. To keep the comparison between the techniques fair, the horizontal axis was chosen to be the energy of each TS over the noise, E_{TS}/N_0. The total transmit energy allocated to each BS per symbol is E_{BS}, so that the total transmit energy per symbol per antenna is E_{BS}/N_T. With this normalization, any additional transmit antennas at a

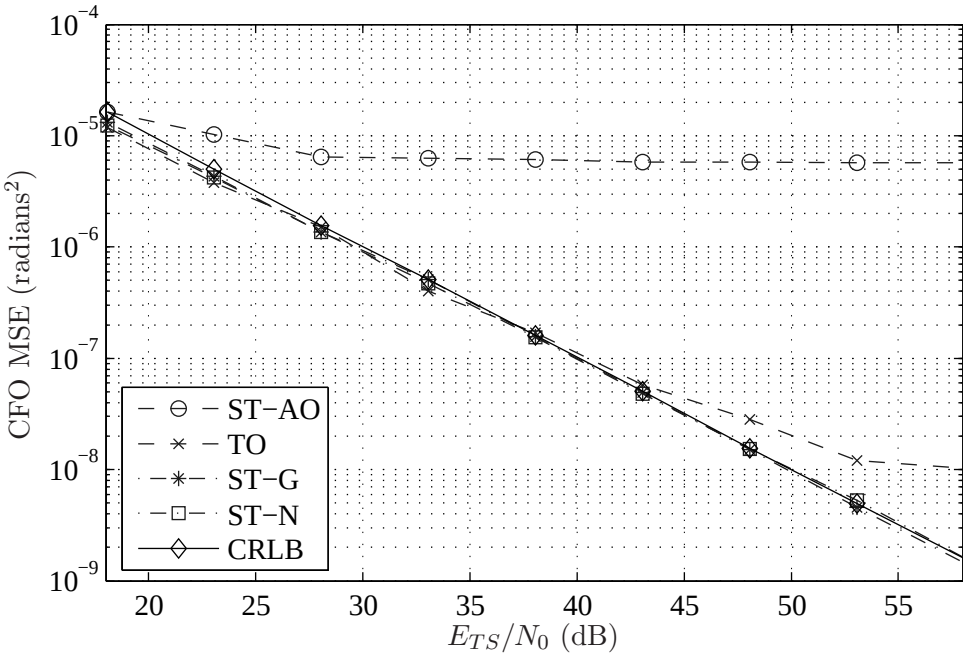

Figure 4.9: CFO MSE vs. TS energy; $B = 4$, $N_R = 2$, $N_T = 2$, $c_{max} = 10^{-2}$, $N = 64$ BPSK Hadamard TS, $a = 10^{-5}$ (for ST-G).

given BS will degrade the estimate quality. The TS SNR is then defined as $E_{TS}/N_0 = NE_{BS}/N_T N_0$. Since the TO sequence lengths are reduced by B, the energy per symbol must be increased by a factor of B to keep the same E_{TS}/N_0 value. As noted earlier, while this is a fair comparison of transmitted energy levels, the transmit amplifiers used for the TO technique are required to handle B times more power than in either the ST-AO or ST-N techniques.

In Figure 4.9, the MSE curves for a system where the $\Lambda(\mathbf{c})$ is guaranteed to be convex for the entire sequence is shown. Curves for the ST-AO, TO, ST-G and ST-N techniques and the CRLB are provided. The system parameters are $B = 4$, $N_T = 2$, and $N_R = 2$. For $c_{max} = 10^{-2}$, the maximum TS length is $N = 157$. A length of $N = 64$ was used to guarantee convexity. Note that the estimates make use of the fact that $\hat{c}_b \in [-c_{max}, +c_{max}]$, which is the reason why they outperform the CRLB at very low SNRs. The effect of the TS correlation is demonstrated in the curve for ST-AO, which has an error floor at an MSE of approximately 10^{-5} radians^2. The two convex techniques are shown to have equivalent performance. The ST-G and ST-N techniques from Section 4.2.2 are seen to achieve the

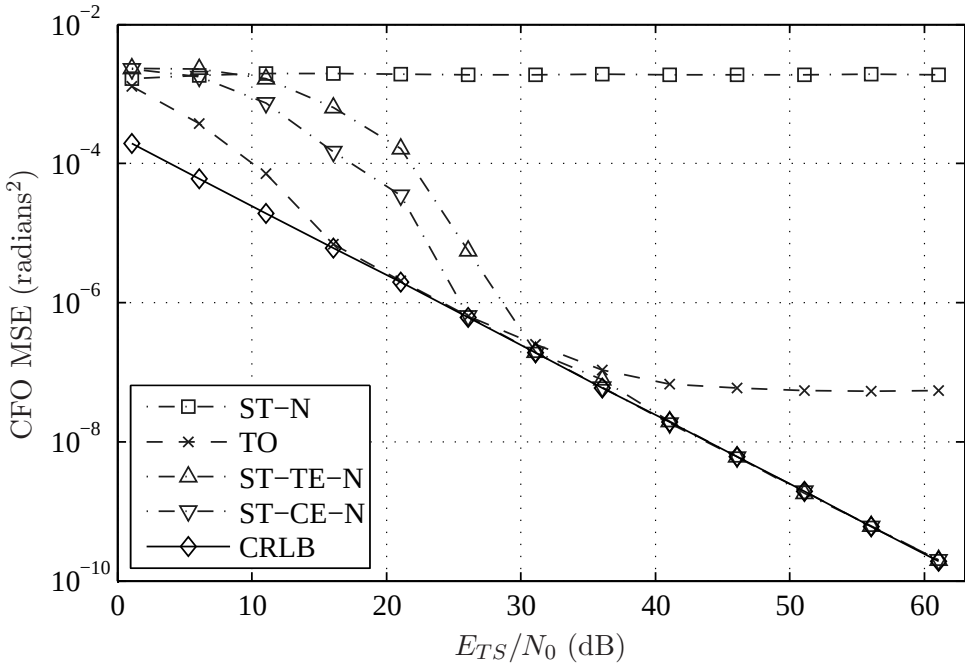

Figure 4.10: CFO MSE vs. TS energy; $B = 4$, $N_R = 2$, $N_T = 2$, $c_{max} = 5 \times 10^{-2}$, $N = 128$ BPSK Hadamard TS.

CRLB at moderate to high SNR; the effects at low E_{TS} are a result of the *a priori* knowledge of c_{max}. The error floor of the TO technique is a result of the FFT resolution being limited to N. By increasing the resolution, thus increasing the complexity, this floor can be reduced. Since the convex techniques do not rely on a discrete CFO search, a similar floor does not appear for ST-N.

In Figure 4.10, MSE curves are presented for a system with a high enough CFO to violate the convexity constraints. The system parameters are $B = 4$, $N_T = 2$, and $N_R = 2$. For $c_{max} = 5 \times 10^{-2}$, the maximum TS length is $N = 31$. To operate with such a short sequence would require very high peak transmit power in order to obtain enough TS energy, so a longer sequence is preferable; a TS length of $N = 128$ was used. The ST-N-TE and ST-N-CE techniques can correct for convexity violation by segmentation of the TS; note that ST-N cannot cope with such a long TS because of this violation. TO is operable in this system, but it requires 4 times the peak power of ST-N-TE and ST-N-CE. The error floor for TO is again the result of the FFT resolution. The performance of both the TO and the segmented simultaneous training techniques converges to the CRLB around an MSE of 10^{-6}. At low SNR, the TO performance is better than the others, probably because its

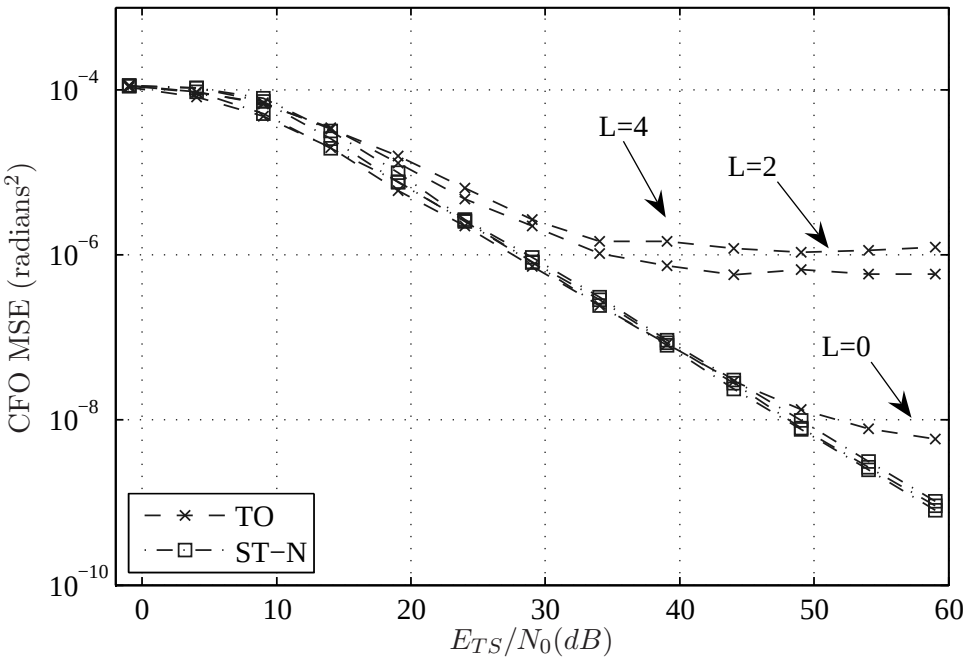

Figure 4.11: CFO MSE vs. TS energy; $B = 2$, $N_R = 2$, $N_T = 2$, $c_{max} = 10^{-2}$, $N = 80$ Random TS.

guaranteed orthogonality allows it to resolve the different TSs more easily. At high SNR, the simultaneous TS methods outperform TO. Between the two SE techniques, the ST-N-CE has the better low-SNR performance. Since the ST-N-CE uses more training symbols at each stage in the estimation process, it has better initial CFO estimates, and thus outperforms the ST-N-TE. In high SNR however, both techniques converge to the lower bound.

To demonstrate the value of the ST-N method in the presence of asynchronous transmission or delay spread, Figure 4.11 shows MSE curves for both ST-N and TO with different values of channel impulse response length L. Note that the TS are now generated randomly, with the constraint that the correlation between any two sequences does not exceed $1/N$. This is necessary since the cross-correlation of time-shifted Hadamard sequences can be quite high; some Hadamard sequences are simply time-shifted versions of others. As noted in Section 4.6, sub-sampling will result in correlated noise components. For these simulations, we will assume the number of sub-samples $N_{ss} = 1$. Impulse response lengths of L=0, 2, and 4 are shown. The delayed received samples experience channels that are also i.i.d. complex Gaussian random variables. The L-tap channel is modeled as having an exponential decay, with magnitude e^{-2l} for the l^{th} tap. The curves for ST-N clearly compensate for the

inter-symbol interference, with a slight shift in the estimator performance; this is attributed to the increase in the number of LS channel estimates. However, TO suffers from the ISI, with error floors in the high SNR region. In order for TO to deal with the multi-path, buffer times have to be introduced after every symbol, resulting in an increase from N to $(L+1)N$ in the length of the TSs; this increase to the TS length is clearly unacceptable in terms of the N/N_f ratio discussed in Section 4.1.1.

Table 4.3 shows the look-up data for $N_{TE}(s)$, for the same simulation parameters of Figure 4.10. An interesting observation is that the SNR where the SE techniques converge with the CRLB corresponds to the point where the total number of stages jumps from 1 to 4. At a per symbol per antenna SNR of 5 dB, the TS SNR is high enough to warrant decreasing the search range of CFOs; this results in an increase in the number of training symbols used in each stage, until the maximum is reached of $N = 128$. At higher SNR, the SE techniques both converge to the CRLB using only 2 stages, since the initial estimate is of high enough quality to permit the use of the entire sequence for the second stage. This corresponds to an SNR of 15 dB and higher.

The simulations show that all the techniques presented in Sections 4.3 and 4.5 converge asymptotically to the CRLB. The trade-off between the convex techniques of ST-G and ST-N lie in the complexity per iteration and the number of iterations until convergence. While ST-G has a simpler per iteration complexity, ST-N converges in fewer iterations in the convex region near the global maximum of $\Lambda(\mathbf{c})$.

The number of receive and transmit antennas are also factors in the MSE of the CFO estimates. Figures 4.12 and 4.13 demonstrate the effect of increasing N_R and N_T on the CRLB, with $\Gamma_b = 30$ dB, $c_{max} = 10^{-2}$, and various values for B. As seen in Figure 4.12, increasing N_R results in a monotonic reduction in CFO MSE, since the received power used for CFO estimation is increased. In fact, in the simulations, we see a log-linear decrease (a 3 dB decrease in the CFO MSE for every doubling of N_R), asymptotically with N_R. This is analytically verified in Section 5.3.2. The variability with respect to B is seen as minimal.

In Figure 4.13, it is shown that the relationship between CFO MSE and increasing N_T is non-monotonic, given a fixed transmit power per training sequence. This non-monotonic relation can be attributed to a trade-off between the diversity brought by additional transmit antennas and the resulting reduction in transmit power allocated to each antenna. For example, for the curve corresponding to simulations with $B = 2$, in the region of $N_T < 6$, the benefit of increasing N_T to the CFO estimates outweighs the degradation due to the

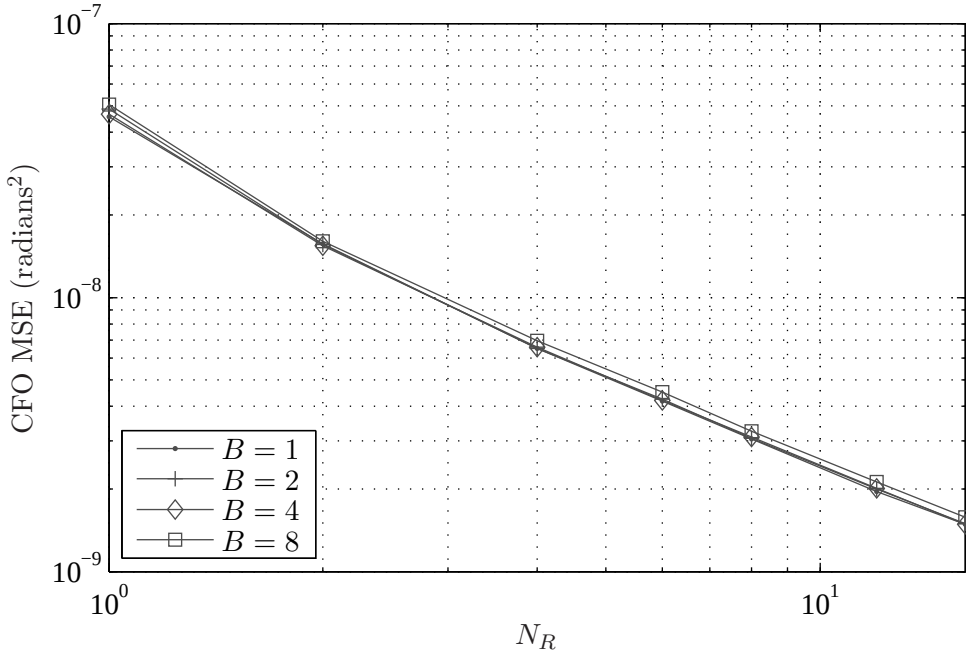

Figure 4.12: CFO MSE vs. N_R; $N_T = 2$, $E_{BS}/N_0 = 30$ dB, $c_{max} = 10^{-2}$, $N = 64$ Hadamard TS.

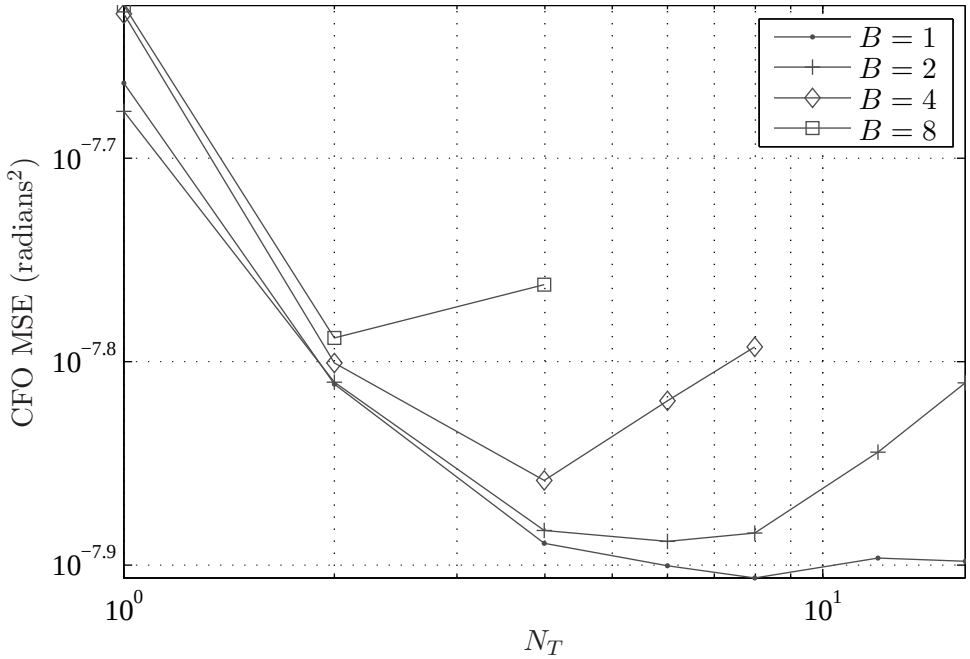

Figure 4.13: CFO MSE vs. N_T; $N_R = 2$, $E_{BS}/N_0 = 30$ dB, $c_{max} = 10^{-2}$, $N = 64$ Hadamard TS.

reduced quality CSI estimates. However, in the region where $N_T > 6$, the reduced transmit power from each antenna takes over.

4.8 Summary

In this chapter, the estimation of multiple CFOs in a CMBMU system is considered. Novel CFO estimation schemes capable of operation in diverse channel conditions and training scenarios are devised. An analytical expression for the Cramer-Rao lower bound for multiple CFOs due to independent LOs is also derived.

Two new convex estimation techniques that use the optimum ML metric are formulated. Both the ST-G and ST-N techniques can accommodate for simultaneously transmitted TSs without any loss in performance. Further, these techniques do not rely on a discrete set of CFO values and therefore do not require smaller bin sizes to mitigate an error floor. Also, both the ST-G and ST-N techniques are capable of achieving the Cramer-Rao lower bound. Compared to time orthogonal CFO estimators, the convex techniques benefit from a reduction in per-symbol transmit power; this translates to lower peak power requirements for RF amplifiers. Modifications to the ML metric that accommodate for frequency selectivity and asynchronous symbol arrivals are also presented. In terms of computational complexity, the convex estimators provide a significant reduction in the number of complex multiply/adds over the optimal ML metric. Although the gradient and Hessian matrix calculations appear to be excessively complex, matrix sparsity and approximation allows the complexity to be reduced even further.

A new ML metric is derived using a version of the MF output pdf that is marginalized over the channel gains. Compared to the original ML metric that is based on a LS estimate of the channel gains, the resulting channel-marginalized metric shows that it is not necessary to have independent TSs at each BS for strict CFO estimation.

Two segmented techniques are devised as extensions to the convex estimators. The segmented techniques guarantee that the convexity of the ML metric search space is maintained for all TS lengths and CFO magnitudes. It is shown that by breaking up the transmitted training symbols into smaller segments, the convexity constraints can be maintained as the accuracy of the estimates are refined.

Finally, the Cramer-Rao lower bound for multiple LO-induced CFOs is derived, and is used to provide variance estimates for each stage of the segmented techniques. The bound

is also used to show the effect of antenna diversity on the CFO MSE.

Chapter 5

Correction of Multibase CFOs

This chapter develops a two-step process for BS CFO estimation and correction. The LO-induced CFOs that cause the capacity degradation as detailed in Chapter 3 exist at all BSs and MSs in the system. Unfortunately, the MSs are incapable of using the CFO estimates from Chapter 4 for MS-side CFO correction, since they cannot alter the weights used for downlink beamforming at the BSs.

The two-step BS CFO estimation and correction process is as follows. First, the MS-side CFO estimates from Chapter 4 are made and fed back to the BSs. Second, the BSs must use the MS-side estimates to make CFO corrections that will minimize capacity degradation. Additionally, the MS CFO adds a bias term into the BS CFO estimates.

This work uses the feedback model presented in Section 2.4.3. The model assumes that initial CFO estimates are pre-calculated by the MSs, with the CMBMU channel impairments in this chapter limited to multiple CFOs only. In Section 5.1, the correlation properties of the MS-side CFO estimates are discussed. Section 5.2 introduces the BS and MS correction procedure, referred to as "CFO tightening" for the BS CFOs. Section 5.3 provides expressions for the analytical spread of the BS CFOs, Section 5.4 deals with the quality of the MS-side estimates, since their quality has consequences for the BS CFO tightening. Finally, Section 5.5 compares these analytical results to simulations.

5.1 Correlation Properties of MS-side CFO Estimates

The MS-side CFO estimates (MCEs) are found at each of the K MSs, using a multi-CFO estimation technique like those detailed in Chapter 4 and [1, 6, 54, 91]. Since these estimates

Table 5.1: Ratio of CFO- and channel-averaged estimator variance to largest covariance; $\Gamma_{b,k} = 30$ dB, $c_{max} = 10^{-2}$, $N = 128$, $N_R = 2$, $N_T = 4$.

B	2	3	4	5	6	7	8
$10\log_{10}\left(\sigma^2_{b,k}/\sigma^2_{b,k,l,k}\right)$	-45.89	-22.74	-19.24	-16.55	-16.30	-16.27	-16.24

are made over independent channel fades and receiver noise, it is obvious that the estimates made at different MSs are uncorrelated. For example, if we define $\sigma^2_{b,k,l,q}$ as the CFO-, channel-, and SNR-dependent covariance between the b^{th} estimate at the k^{th} MS and the l^{th} estimate at the q^{th} MS, then

$$\sigma^2_{b,k,l,q} = 0 \ \forall \ k \neq q. \tag{5.1}$$

However, the values of the covariances among the B estimates found at a single MS ($\sigma^2_{b,k,l,k}$) are not so simple to determine.

The CRLB for MS-side CMBMU CFO estimation that was calculated for the work in Chapter 4 is summarized in Appendix A. Table 5.1 shows the average of 10^6 Monte Carlo realizations of $CRLB_c$ from (A.18) with $\Gamma_{b,k} = 30$ dB, $c_{max} = 10^{-2}$, $N = 128$, $N_R = 2$, and $N_T = 4$. The table shows the ratio between the largest MCE covariance between any two MCEs $\left(max_{b\neq l}\left(\sigma^2_{b,k,l,k}\right)\right)$ and the CFO- and channel-averaged MCE variance $\left(\sigma^2_{b,k} = \sigma^2_{b,k,b,k}\right)$; the ratios for the $(B\,(B-1)\,/2) - 1$ remaining correlation values are less than the value reported. The results demonstrate that the maximum covariances of the MCEs are low enough that they can be considered to be uncorrelated. Even for $B = 4$, the largest correlation is still 19 dB down from the covariance of the estimates. These results suggest that the MCE covariance matrix can be approximated as diagonal.

Since the BS CFO estimator presented in Section 5.2 relies on the MCE variances, methods to find or approximate the MCE variances are also of interest. Section 5.3 builds on the observation that calculation of the MCE variances can be done independently to provide a parameterized and linear approximation to the CRLB. For now, the MCEs used in Section 5.2 can be considered to be known exactly.

5.2 BS CFO Estimation Using MS-side Feed-back

This section presents a detailed derivation of the BS CFO tightening procedure. As noted in the system model of Section 2.4.3, the MCEs $\hat{c}_{b,k}$ from Chapter 4 are used to form the BS

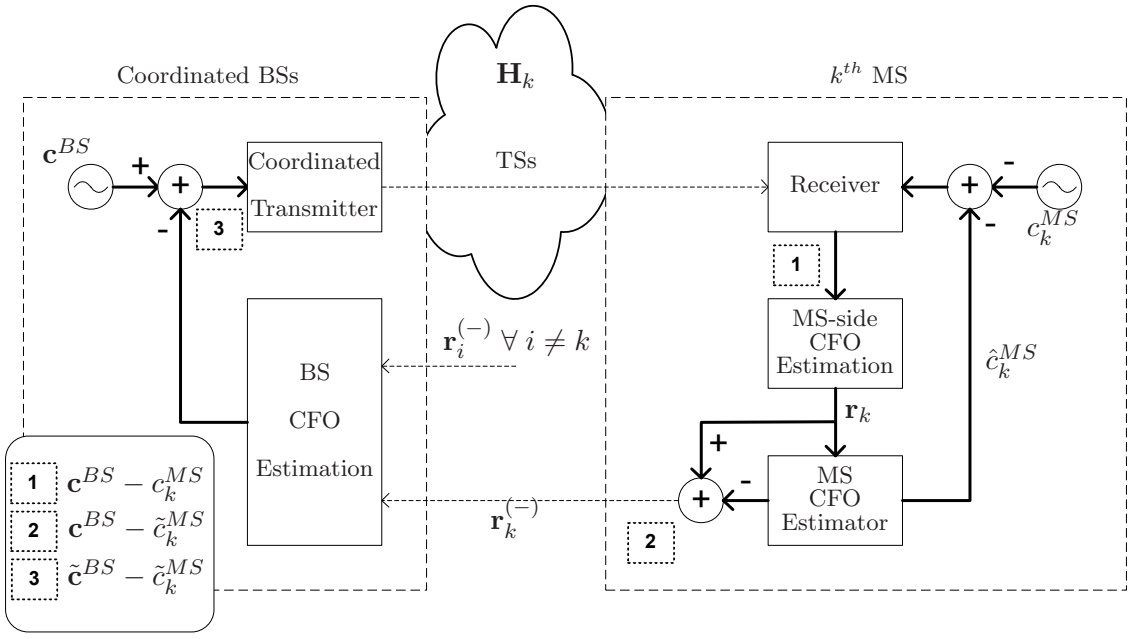

Figure 5.1: Coordinated multibase/multiuser CFO estimate feedback model.

and MS CFO estimates. The MCEs from the k^{th} MS are stored in the vector $\mathbf{r}_k \in \mathbb{R}^{B\times 1}$. The BS CFO tightening procedure proposed here involves the feedback of MCEs to the coordinated BSs, with CFO correction done at both the BSs and MSs. A flow diagram of the process is shown in Figure 5.1, from the perspective of the k^{th} MS.

For clarity, we develop the tightening procedure for the BS CFOs in three parts, the first two special cases, as illustrated in Figure 5.2. The first case treats MSs that form noisy CFO estimates, but have zero CFO themselves, and is used to derive the BS-side CFO estimator. The second case considers the MSs to form noise-free estimates, but to have non-zero CFOs themselves, in order to demonstrate that the bias presented by the MS CFOs can be virtually eliminated. The third case is the general one, with MSs that both produce noisy estimates and have their own non-zero CFOs.

The feedback channel from the MS to the basestation controller (BSC) is an integral part of this correction scheme. For CFO estimators presented in this section, the feedback information from each MS must include both the MCEs in $\mathbf{r}_k$ and the MIMO channel SNR estimates in $\mathbf{\Gamma}_k$. For the purposes of this study, the transmission of $\mathbf{r}_k$ and $\mathbf{\Gamma}_k$ is assumed to be error-free.

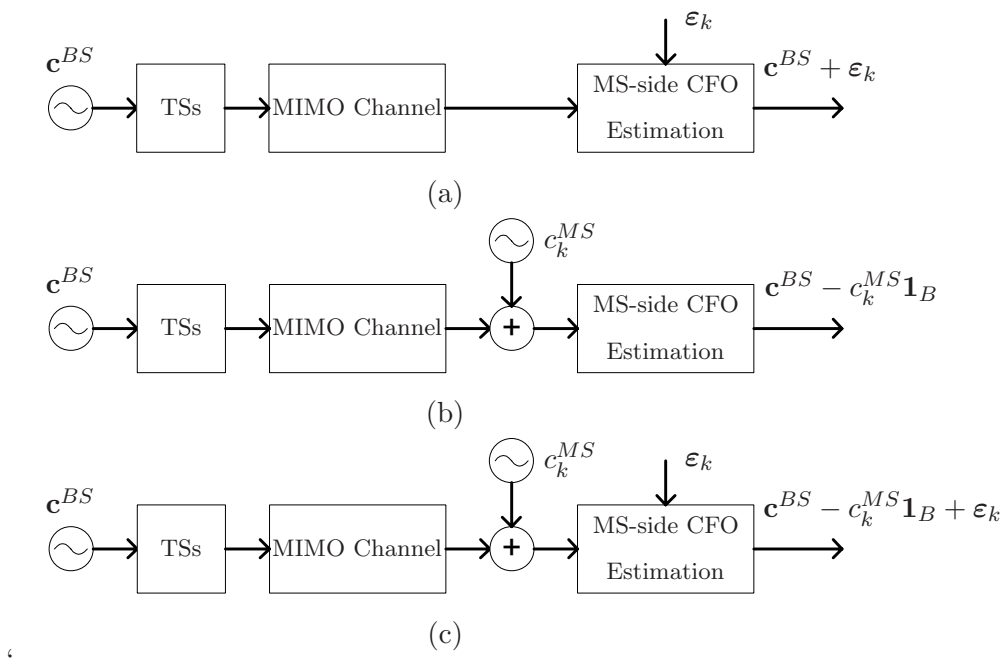

Figure 5.2: Three cases for BS CFO estimation.

At each BS and MS, CFO correction can be done by pre-multiplying each transmit symbol or receive symbol with the corresponding normalized LO CFO estimate using $\exp(-j\hat{c}n)$. The product of the actual CFO and the conjugate of the estimate becomes $\exp(j\tilde{c}n)$, where $\tilde{c} = c - \hat{c}$. From this point on, $\tilde{c}_b^{BS}$ is used to denote the value of the BS CFO after cancellation, where

$$\tilde{c}_b^{BS} = c_b^{BS} - \hat{c}_b^{BS}. \tag{5.2}$$

Similarly,

$$\tilde{c}_k^{MS} = c_k^{MS} + \hat{c}_k^{MS}. \tag{5.3}$$

The sign inversion in $\tilde{c}_k^{MS}$ is due to down-conversion at the MS. This is seen in the MS-side CFO $c_{b,k} = c_b^{BS} - c_k^{MS}$ from (2.21); since the MS CFO is negative in $c_{b,k}$, it requires the sign inversion of $\hat{c}_k^{MS}$ in (5.3).

5.2.1 Case 1: Imperfect MS-side CFO Estimates, No MS CFO Bias

In this case, it is assumed that the MS LOs are perfectly synchronized to the nominal carrier frequency, so $\mathbf{c}^{MS} = \mathbf{0}$. We focus on joint estimation of the BS CFOs using the BK noisy

MS-side estimates.

The k^{th} MS-side estimate is unbiased and can be modeled as the $\mathbb{R}^{B\times 1}$ vector $\mathbf{r}_k$

$$\mathbf{r}_k = \mathbf{c}^{BS} + \boldsymbol{\varepsilon}_k, \tag{5.4}$$

where $\mathbf{c}^{BS} \in \mathbb{R}^{B\times 1}$ contains the BS CFOs and $\boldsymbol{\varepsilon}_k \in \mathbb{R}^{B\times 1}$ is an error vector containing zero-mean random variables. The components $\varepsilon_{b,k}$ of $\boldsymbol{\varepsilon}_k$ each have variance $\sigma^2_{b,k}$. The variance of the MS-side CFO estimates is dependent on the second order statistics of the $(b,k)^{th}$ MIMO channel, as evident from analyzing the CRLB in Appendix A. Define the stack of all MS-side estimates as

$$\mathbf{r} = \left[\mathbf{r}_1^T \cdots \mathbf{r}_K^T\right]^T \tag{5.5}$$

and the stack of all MCE errors as

$$\boldsymbol{\varepsilon} = \left[\boldsymbol{\varepsilon}_1^T \cdots \boldsymbol{\varepsilon}_K^T\right]^T. \tag{5.6}$$

The mean and variance of the $[(k-1)\,K+b]^{th}$ component of $\mathbf{r}$ are c_b^{BS} and $\sigma^2_{b,k}$, respectively.

In matrix form, the expression in (5.5) can be rewritten as

$$\mathbf{r} = \tilde{\mathbf{I}}\mathbf{c}^{BS} + \boldsymbol{\varepsilon}, \tag{5.7}$$

where $\tilde{\mathbf{I}} \in \mathbb{R}^{BK\times B}$ is the stack of K $\mathbf{I}_B$ matrices and $\boldsymbol{\varepsilon}$ contains the estimation error. At this point, we will make the assumption that the distribution of the MCEs is Gaussian. A sample of channel averaged $\varepsilon_{b,k}$ passed the Chi-square test of goodness of fit. Using this Gaussian assumption, the pdf of $\mathbf{r}$ is then

$$p_r\left(\mathbf{r}|\mathbf{c}^{BS}\right) = \frac{1}{(2\pi)^{BK/2}\left|\mathbf{R}_r\right|} e^{-\left(\mathbf{r}-\tilde{\mathbf{I}}\mathbf{c}^{BS}\right)^T \mathbf{R}_r^{-1}\left(\mathbf{r}-\tilde{\mathbf{I}}\mathbf{c}^{BS}\right)}, \tag{5.8}$$

where $\mathbf{R}_r \in \mathbb{R}^{BK\times BK}$ is the covariance matrix of $\mathbf{r}$. The joint maximum likelihood (ML) estimate is the $\mathbf{c}^{BS}$ value that minimizes the exponent in (5.8), and is given by

$$\hat{\mathbf{c}}^{BS} = \left(\tilde{\mathbf{I}}^T\mathbf{R}_r^{-1}\tilde{\mathbf{I}}\right)^{-1}\tilde{\mathbf{I}}^T\mathbf{R}_r^{-1}\mathbf{r}. \tag{5.9}$$

The results from Section 5.1 suggest that the MCE covariances can be approximated as zero. Thus, the matrix $\mathbf{R}_r$ in (5.8) can be represented as a diagonal matrix with components $\sigma^2_{b,k} = E\left\{\left|\varepsilon_{b,k}\right|^2\right\}$. Note that $\sigma^2_{b,k}$ depends on the CFOs, channel gains, and SNR.

The b^{th} component of (5.9) can now be re-written as the weighted sum

$$\hat{c}_b^{BS} = \beta_b \sum_{k=1}^{K} \sigma_{b,k}^{-2} r_{b,k}, \tag{5.10}$$

where

$$\beta_b = \left(\sum_{k=1}^{K} \sigma_{b,k}^{-2} \right)^{-1} \tag{5.11}$$

is a normalization term for the b^{th} BS CFO. Note that the joint ML estimate of the b^{th} BS CFO (5.10) depends only on the MS estimates of its own value, and not on the MS estimates of CFOs at other BSs. With this decoupling, the BSs can estimate and correct their own CFO offsets independently of one another. However, coordination through the BSC is still necessary for downlink beamforming.

5.2.2 Case 2: Perfect MS-side CFO Estimates, MS CFO Bias

In Section 5.2.1, $\mathbf{c}^{MS}$ was set equal to zero to ease calculation of the BS CFO ML estimate. In an actual system, however, it is more probable that the variability of the MS CFOs is greater than that of the BS CFOs since it is more practical to have a high precision LO at the BS due to cost, power and space issues. In this section, we consider the case of non-zero MS CFO with perfect MS-side estimates.

To deal with the CFO bias introduced at the MSs, a cancellation technique is proposed here as a means to reduce the CFO scatter of the MCEs that are sent to the BSs. Also, since CMBMU capacity loss is caused by the *spread* of BS LO frequencies, not their average value, the cancellation technique is extended to the BSs in order to correct their CFOs. Reducing the difference between the BS CFOs is just as effective as reducing the CFO magnitude c_{max} in terms of system capacity.

The common BS CFO value, denoted as c_{common}^{BS}, is defined here as the remainder CFO after cancellation at the BSs; that is, due to the MS CFO bias, the BS CFOs have a non-zero average. The question remains as to whether c_{common}^{BS} could cause excessive adjacent channel interference to other communication systems. If c_{common}^{BS} is the same magnitude as the original CFOs however, this should not pose a problem.

To demonstrate how the MS CFO cancellation will result in the convergence of the BS CFOs, we consider a system with perfect MS-side estimates of the BS CFOs, so that

$$r_{b,k} = c_b^{BS} - c_k^{MS}. \tag{5.12}$$

Next, the MSs estimate their own offsets as the arithmetic average of their B MCEs. The resulting k^{th} MS CFO estimate can be expressed as

$$\begin{aligned} \hat{c}_k^{MS} &= \overline{(r_{b,k})}^b \\ &= -c_k^{MS} + \overline{\left(c_b^{BS}\right)}^b \\ &= -c_k^{MS} + c_{common}^{BS}, \end{aligned} \tag{5.13}$$

where $\overline{(\cdot)}^b$ refers to the arithmetic mean over the index b. Notice the bias term here of c_{common}^{BS}. The MS then subtracts its estimate of its own CFO from its estimates of the BS CFOs, and sends the difference back to the BSs as the modified feedback term, $r_{b,k}^{(-)}$,

$$\begin{aligned} r_{b,k}^{(-)} &= r_{b,k} - \hat{c}_k^{MS} \\ &= c_b^{BS} - c_{common}^{BS}. \end{aligned} \tag{5.14}$$

In essence, the MSs return the deviation of the b^{th} BS CFO from the centroid c_{common}^{BS}. This has the effect of removing the MS CFO bias term c_k^{MS} before BS CFO estimation. The subtraction is done at the MS so that it can also make a separate correction to its own CFO.

Since there is no noise present, the estimation of the BS CFOs at the BSC is very simple. We can choose $\hat{c}_b^{BS} = r_{b,k}^{(-)}$ with any value for k, since the K MCEs are all noise-free and identical (from (5.14)). Thus,

$$\hat{c}_b^{BS} = r_{b,k}^{(-)} \; \forall \; k. \tag{5.15}$$

The last step is for each BS to correct its carrier frequency. For the b^{th} BS, this results in

$$\begin{aligned} \tilde{c}_b^{BS} &= c_b^{BS} - \hat{c}_b^{BS} \\ &= c_{common}^{BS}. \end{aligned} \tag{5.16}$$

This shows that all of the BS CFOs come to a common frequency, irrespective of the MS CFOs. Also, calculating $\tilde{c}_k^{MS}$, we can see that the MS CFOs are all on the same common frequency as well. The result is that the entire system converges to the common frequency c_{common}^{BS} in a single step.

5.2.3 Case 3: Imperfect MS-side CFO Estimates, MS CFO Bias

This is the most comprehensive case, since it combines the optimal joint BS CFO estimation as presented in Section 5.2.1 with the cancellation technique used in Section 5.2.2. Since

the MCEs are now noisy, (5.12) changes to

$$r_{b,k} = c_b^{BS} - c_k^{MS} + \varepsilon_{b,k}. \tag{5.17}$$

Also, we will use the optimal ML estimate for the MS CFO, which is similar in form to the BS CFO ML estimator found in (5.9), so that

$$\hat{c}_k^{MS} = \kappa_k \sum_{b=1}^{B} \sigma_{b,k}^{-2} r_{b,k}, \tag{5.18}$$

where

$$\kappa_k = \left(\sum_{b=1}^{B} \sigma_{b,k}^{-2} \right)^{-1}. \tag{5.19}$$

Then, we use (5.18) in (5.14) to find $\mathbf{r}^{(-)}$.

In this case, the BS CFO ML estimator will substitute $\mathbf{r}$ in (5.9) with $\mathbf{r}^{(-)}$ from (5.14). The BS CFO ML estimate for the b^{th} BS CFO is then

$$\hat{c}_b^{BS} = \beta_b \sum_{k=1}^{K} \sigma_{b,k}^{-2} r_{b,k}^{(-)}, \tag{5.20}$$

where β_b is from (5.11).

For noisy MCEs, the BS CFOs do not converge to exactly the same common CFO. Using (5.20),

$$\begin{aligned} \tilde{c}_b^{BS} &= \left(c_b^{BS} - \hat{c}_b^{BS} \right) \\ &= \beta_b \sum_{k=1}^{K} \sigma_{b,k}^{-2} \left[\left(\kappa_k \sum_{l=1}^{B} \sigma_{l,k}^{-2} \left(c_l^{BS} + \varepsilon_{l,k} \right) \right) - \varepsilon_{b,k} \right], \end{aligned} \tag{5.21}$$

where the BS CFO contribution is accompanied by two noise terms. These noise terms are dependent upon the BS, and by extension on their MCEs. The higher the SNR between a BS and the MSs, the lower the magnitude of both noise terms. Note the c_l^{BS} term; if all channel SNRs were identical, so that $\sigma_{b,k}^2 = \sigma^2 \ \forall \ (b,k)$, then the expression would reduce to

$$\tilde{c}_b^{BS} = c_{common}^{BS} + \overline{\left(\overline{(\varepsilon_{l,k})}^{l} \right)}^{k} - (1/B) \, \overline{(\varepsilon_{b,k})}^{k}, \tag{5.22}$$

where $\overline{\left(\overline{(\cdot)}^{l} \right)}^{k}$ refers to the arithmetic mean over both the l and k indices.

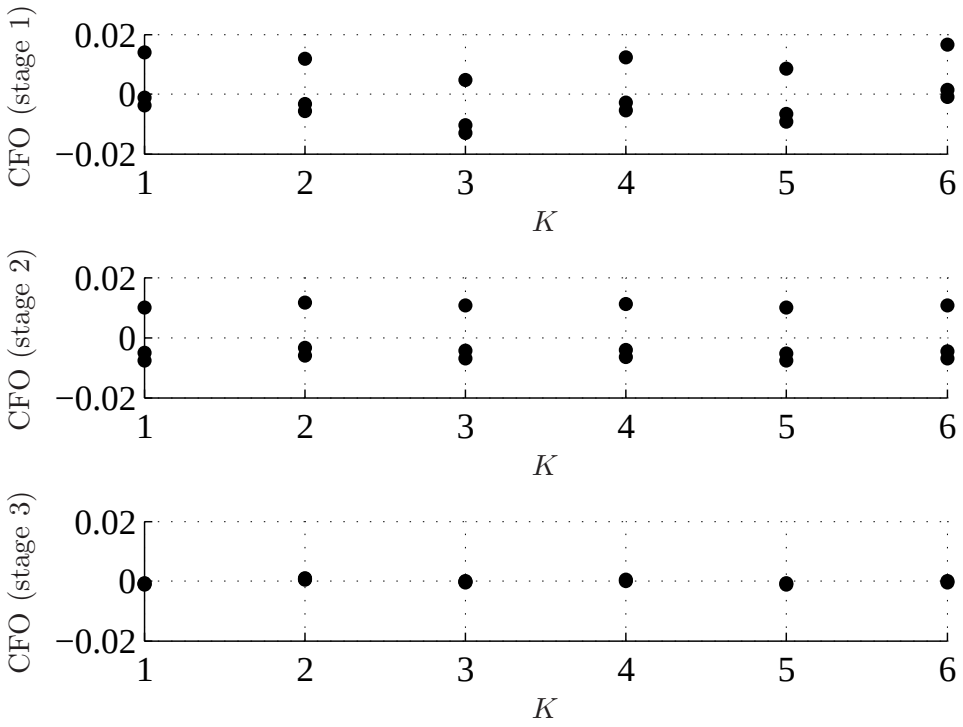

Figure 5.3: Stage 1: Effective CFOs seen by MSs ($c_{b,k}$), Stage 2: Effective CFOs after MS correction, Stage 3: Effective CFOs after MS and BS correction (see Figure 2.5); $B = 3$, $c_{max} = 10^{-2}$, $K = 6$, $N = 64$, $N_R = N_T = 2$, $\Gamma_{b,k} = 10$ dB.

To illustrate, Figure 5.3 shows a realization of the effective CFOs for all BSs and MSs, for a system with $B = 3$ and $K = 6$. The three sub-figures show the CFOs at the three stages in Figure 5.1; that is, the initial CFOs $c_{b,k}$, the CFOs after MS correction, and the CFOs after BS and MS correction. This figure clearly shows how the CFOs are reduced to a fraction of their original value, and why the procedure is referred to as "tightening" of the BS CFOs.

5.3 Post-Correction BS CFO Spread

The capacity of the CMBMU system is a function of the spread of the BS CFOs, as explained in Section 5.2.2. In this section, expressions for the expectation of the BS CFO spread are found for the three cases in Section 5.2. The expectation is taken over CFO, fading channel and noise ensembles.

We define the mean square spread (MSS) for a CMBMU system as

$$\rho = \overline{E_\varepsilon \left[\left(\tilde{c}_b^{BS} - \overline{\tilde{c}_b^{BS}}^b \right)^2 \right]}^b . \tag{5.23}$$

Note that this MSS expression is dependent upon the $\Gamma_{b,k}$ through β_b, κ_k and $\sigma_{b,k}^2$. The MSS is used to measure the variance of the individual BS CFOs after cancellation, and presents a single metric with which overall estimator performance can be judged. Recall also that it is the spread among the CFOs, not the magnitude of the CFOs, that causes loss in system capacity. In the following, simulations are used to verify the analytical results and to help understand the estimation process.

5.3.1 Analysis of Case 1

For case 1, the MSE as well as the MSS will be examined, since it contributes to an understanding of the BS CFO estimator. The MSE for the b^{th} BS CFO estimate is derived using (5.7) and (5.10-5.11) to be

$$E\left\{ \left(\tilde{c}_b^{BS} \right)^2 \right\} = \beta_b, \tag{5.24}$$

where β_b is the normalization term for the b^{th} BS CFO estimate from (5.11). Since it involves a linear combination of the inverses of the MS-side MSEs, low quality estimates will have minimal impact on the estimate variance if high quality estimates exist.

The BS CFO MSS can be calculated using (5.2), (5.7), (5.10-5.11), and (5.23). First, by inserting the actual CFO from (5.7) into (5.10), the estimated CFO is found to be

$$\hat{c}_b^{BS} = c_b^{BS} + \beta_b \sum_k \sigma_{b,k}^{-2} \varepsilon_{b,k}. \tag{5.25}$$

Inserting (5.25) into the expression for $\tilde{c}_b^{BS}$ in (5.2) results in

$$\tilde{c}_b^{BS} = -\beta_b \sum_k \sigma_{b,k}^{-2} \varepsilon_{b,k}. \tag{5.26}$$

Finally, inserting $\tilde{c}_b^{BS}$ from (5.26) into (5.23) results in

$$\begin{aligned} \rho &= \frac{1}{B} \sum_b \left[\frac{1}{B^2} \left(\sum_{l \neq b} \beta_l + (B-1)^2 \beta_b \right) \right] \\ &= \frac{B-1}{B} \overline{\beta_b}^b. \end{aligned} \tag{5.27}$$

where the intermediate steps use the fact that the MCEs are considered independent for all BSs and MSs and that $E_\varepsilon \left[\left(\beta_b \sum_k \sigma_{b,k}^{-2} \varepsilon_{b,k} \right)^2 \right] = \beta_b$. Notice that as $B \to \infty$, the MSS will be equivalent to the arithmetic mean of the MSE in (5.24).

5.3.2 Analysis of Case 2

Since the MS-side estimates are perfect, the MSE in this case is reduced to a constant value of

$$E \left\{ \left(\tilde{c}_b^{BS} \right)^2 \right\} = \left(c_{common}^{BS} \right)^2, \tag{5.28}$$

and the MSS is $\rho = 0$. This demonstrates that, in the absence of estimator noise, the MSS can be reduced to zero in the presence of MS CFOs. Since $\tilde{c}_k^{MS} = c_{common}^{BS}$, the resulting CFO at the MS post-cancellation will be $\tilde{c}_b^{BS} - \tilde{c}_k^{MS} = 0$.

5.3.3 Analysis of Case 3

The BS CFO estimator must now contend with both MS CFO bias and noisy MCEs, so we expect the MSS of $\hat{c}_b^{BS}$ to be no better than that in Section 5.2.1.

The closed form expression for the MSS is found using (5.21) and (5.23). First, the MSS for the b^{th} BS CFO is found using (5.21) to be

$$E_\varepsilon\left[\left(\tilde{c}_b^{BS}-\overline{\tilde{c}_b^{BS}}^b\right)\right]=\frac{1}{B^2}\left\{\begin{array}{c}\sum_q\beta_q-\sum_{q\neq b}\sum_{r\neq b}\beta_q\beta_r\left(\sum_k\sigma_{q,k}^{-2}\sigma_{r,k}^{-2}\kappa_k\right)+(B-1)^2\beta_b\\-(B-1)^2\beta_b^2\sum_k\sigma_{b,k}^{-2}\kappa_k\\+2(B-1)\beta_b\sum_{q\neq b}\left(\beta_q\sum_k\left(\sigma_{q,k}^{-2}\sigma_{b,k}^{-2}\kappa_k\right)\right)\end{array}\right\}, \tag{5.29}$$

where, like in case 1, the intermediate steps use the fact that the MCEs are considered independent for all BSs and MSs and that $E_\varepsilon\left[\left(\beta_b\sum_k\sigma_{b,k}^{-2}\varepsilon_{b,k}\right)^2\right]=\beta_b$. Then, taking the average over all BSs, ρ is found to be

$$\rho=\frac{B-1}{B}\overline{\beta_b}^b+\overline{\left(\begin{array}{c}2(B-1)\beta_b\left\{\sum_{q\neq b}\beta_q\left[\sum_k\sigma_{q,k}^{-2}\sigma_{b,k}^{-2}\kappa_k\right]\right\}-\\(B-1)^2\beta_b^2\left[\sum_k\sigma_{b,k}^{-4}\kappa_k\right]-\\\sum_{q\neq b}\sum_{r\neq b}\beta_q\beta_r\left[\sum_k\sigma_{q,k}^{-2}\sigma_{r,k}^{-2}\kappa_k\right]\end{array}\right)}^b. \tag{5.30}$$

Note that the MSS for case 3 in (5.30) has a common term with the MSS for case 1 in (5.27); the additional term is caused by the non-zero MS CFO. However, note that the β_b terms are inversely proportional to SNR, since they are a function of the MCE error variances. Thus, since the second term in (5.30) consists of second-order products of β_b, it will be much smaller than the first term, and the MSSs for case 1 and 3 will be nearly identical.

5.4 Complexity Reduction for Gauging Quality of MS-side CFO Estimates

This section provides a simplified and parameterized expression for the error variance of the MCE based on the CRLB. The MCE error variances are used when forming BS CFO estimates with the MCEs themselves. The main focus of this chapter, that of BS CFO estimation and correction, can be simplified by using the parameterized variance expression. Instead of relying on an expression for MCE variance that depends on the instantaneous CFOs, channel gains and SNRs, a single-BS, channel-averaged approximation based only on the instantaneous SNR is proposed. As demonstrated in the simulations of Section 5.5, this simplification has no discernable effect on the performance of the tightening procedure.

5.4.1 Single-BS Approximation

The BS CFO tightening procedure of Section 5.2 uses the MCE variance $\sigma^2_{b,k}$. In this section, a simplified version of the CRLB from Appendix A is proposed to provide values for the MCE variances.

The unwieldy nature of the CRLB shown in Appendix A is due to the differences among the BS CFOs. For $B > 1$, the matrix product $\mathbf{D}^\dagger(\mathbf{c}_k)\mathbf{D}(\mathbf{c}_k)$ is not diagonal. However, for $B = 1$, $\mathbf{D}^\dagger(c_k)\mathbf{D}(c_k) = \mathbf{I}$ and the CRLB estimate of the error variance in (A.18) can be reduced to the following expression:

$$\begin{aligned} CRLB_c|_{B=1}(\mathbf{h}_k, \Gamma_k) &= \hat{\sigma}^2_{k,1}(\mathbf{h}_k, \Gamma_k) \qquad (5.31) \\ &= \frac{1}{2\Gamma_k}\left[\mathbf{h}_k^\dagger\left[\mathbf{I}_{N_R} \otimes \left(\mathbf{X}^\dagger\mathbf{Z}^2\mathbf{X} - \mathbf{X}^\dagger\mathbf{Z}\mathbf{X}(\mathbf{X}^\dagger\mathbf{X})^{-1}\mathbf{X}^\dagger\mathbf{Z}\mathbf{X}\right)\right]\mathbf{h}_k\right]^{-1}, \end{aligned}$$

where $\mathbf{X}$ and $\mathbf{Z}$ are defined in Appendix A. Other multi-CFO estimators, such as that in [6], ensure a diagonal $\mathbf{D}^\dagger(\mathbf{c}_k)\mathbf{D}(\mathbf{c}_k)$ by allowing only one antenna to transmit at a time (or in our case, allowing only one BS to transmit at a time). However, they have drawbacks in peak power and in frequency resolution, as discussed in [89].

The expression in (5.31) is more compact and easily and calculable than the true CRLB in (A.18), since it is independent of any CFOs and is quadratic in $\mathbf{h}_{b,k}$. However, the effect of TS correlation as a result of multiple CFOs [6] is disregarded in (5.31). Fortunately, as shown in Section 5.2.1, the covariances among these multiple CFOs are minimal, suggesting that the single-BS approximation in (5.31) may be adequate for calculating the MCE variances. The difference between (5.31) and (A.18) is quantified in the following.

Figure 5.4 shows curves for the CRLB of (A.18) after normalization by the single-BS CRLB of (5.31), where the normalized CRLB is defined as

$$CRLB_{norm} = \frac{E_{h,c}\left[CRLB_c(\mathbf{H}_k, \mathbf{c}_k, \mathbf{\Gamma}_k)\right]}{E_h\left[CRLB_c(\mathbf{H}_k, \Gamma_{k,1})|_{B=1}\right]}. \qquad (5.32)$$

The purpose of these curves is to show the effect of additional independent CFOs on the CRLB. The curves are plotted versus the number of BSs B, with a variety of SNRs and TSs. Each curve was created with 10^6 Monte Carlo realizations on (A.18) with the components of $\mathbf{h}_{b,k}$ being i.i.d. Rayleigh random variables with unit variance; the SNR $\Gamma_{b,k}$ is the same for every BS to MS link, with the transmit power distributed evenly across all BS antennas.

From Figure 5.4, it is evident that each independent CFO added to the system results

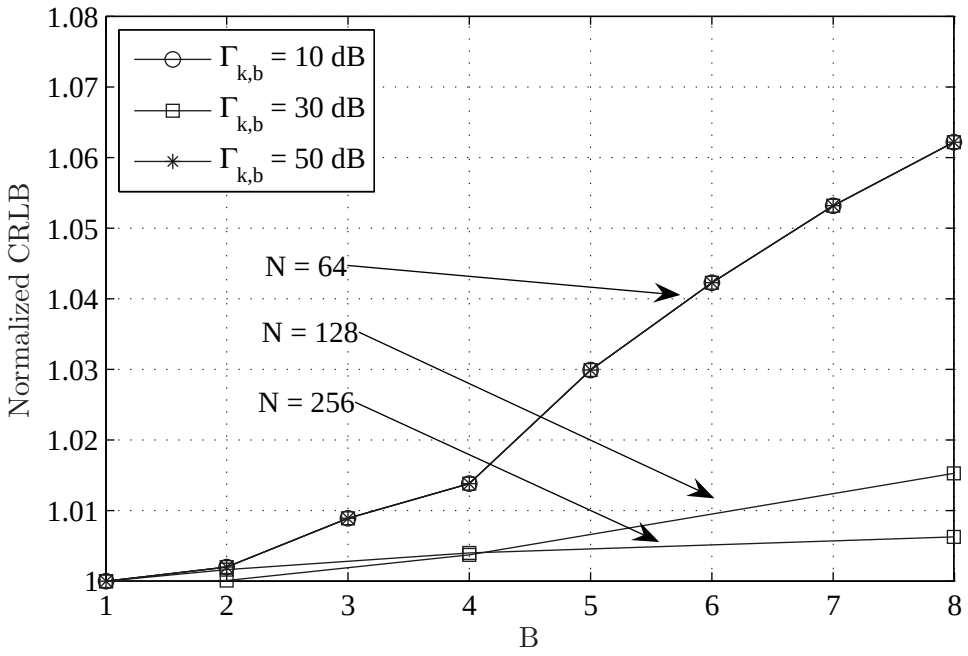

Figure 5.4: Normalized MS-side CFO estimate CRLB versus B; $c_{max} = 10^{-2}$, $N_R = N_T = 2$.

in an increase to $CRLB_{norm}$. This is due to the additional interference caused by CFO-induced TS correlation, and is the reason behind the complexity of the CRLB presented in Appendix A. However, Figure 5.4 shows that this effect is relatively small for longer TSs, with less than a 2% increase in $CRLB_{norm}$ for $N > 128$ and $B < 8$. Since the estimators presented in Section 5.4 do not use the MCE variance directly to calculate the CFOs, but rather as a means of weighting their relative estimate quality, these observations suggest that the simplified single-BS CRLB is adequate.

Figure 5.4 also demonstrates that the SNR has no effect on $CRLB_{norm}$ when B is increased, shown for the $N = 64$ case. However, an increase in temporal aperture does result in a change in $CRLB_{norm}$. The temporal aperture effect can be used to compensate for the TS correlation caused by additional independent CFOs; that is, longer TSs can mitigate the effect of multiple correlated TSs. This result suggests that CMBMU systems with a very large number of BSs are capable of estimating CFOs as long as the TS length can be increased.

5.4.2 Channel State Independent Approximation

In Section 5.4.1, it was demonstrated that the single-BS approximation of the CRLB for the MCEs could be used to calculate the MCE variances. In this section, it is shown that the single-BS approximation can be further simplified by marginalization over the channel gains, as long as the CMBMU system satisfies $N_R N_T >> 1$.

From (5.31), the expectation over the channel gain vector $\mathbf{h}_{b,k}$ of the reciprocal of the MCE variance estimate can be written in terms of the trace of the inverse, so

$$E_h\left[\frac{1}{\hat{\sigma}^2_{b,k}\left(\mathbf{h}_{b,k},\Gamma_{b,k}\right)}\right] = 2\Gamma_{b,k}\, tr\left(\mathbf{I}_{N_R}\otimes\left(\mathbf{X}_b^\dagger\mathbf{Z}^2\mathbf{X}_b - \mathbf{X}_b^\dagger\mathbf{Z}\mathbf{X}_b\left(\mathbf{X}_b^\dagger\mathbf{X}_b\right)^{-1}\mathbf{X}_b^\dagger\mathbf{Z}\mathbf{X}_b\right)E_h\left[\mathbf{h}_{b,k}\mathbf{h}_{b,k}^\dagger\right]\right). \quad (5.33)$$

In the case of independent channel gains, $E_h\left[\mathbf{h}_{b,k}\mathbf{h}_{b,k}^\dagger\right] = \mathbf{I}_{N_R N_T}$, and (5.33) simplifies to

$$E_h\left[\frac{1}{\hat{\sigma}^2_{b,k}\left(\mathbf{h}_{b,k},\Gamma_{b,k}\right)}\right] = 2\Gamma_{b,k}N_R T, \quad (5.34)$$

where

$$T = tr\left(\mathbf{X}_b^\dagger\mathbf{Z}^2\mathbf{X}_b - \mathbf{X}_b^\dagger\mathbf{Z}\mathbf{X}_b\left(\mathbf{X}_b^\dagger\mathbf{X}_b\right)^{-1}\mathbf{X}_b^\dagger\mathbf{Z}\mathbf{X}_b\right) \quad (5.35)$$

is a function of the TSs.

In general, the inverse of (5.34), $1/E_h\left[1/\hat{\sigma}^2_{b,k}\left(\mathbf{h}_{b,k},\Gamma_{b,k}\right)\right]$ is not equivalent to the expectation of the MCE variance estimate, $E_h\left[\hat{\sigma}^2_{b,k}\left(\mathbf{h}_{b,k},\Gamma_{b,k}\right)\right]$. However, the diversity effect provided by multiple antennas reduces the coefficient of variation of the variance estimates. In other words, when the number of independent channel gains $N_R N_T$ is large enough, the MCE variance can be approximated with

$$s^2_{b,k}(\Gamma_{b,k}) \triangleq \frac{1}{E_h\left[\frac{1}{\hat{\sigma}^2_{b,k}\left(\mathbf{h}_{b,k},\Gamma_{b,k}\right)}\right]} = \frac{1}{2\Gamma_{b,k}N_R T}. \quad (5.36)$$

To illustrate the effect of antenna diversity, the percentage difference between (5.31) and (5.36) is shown in Table 5.2, over 10^4 Monte Carlo realizations and for a variety of N_R and N_T values. The results show that the accuracy of the approximation improves as $N_R N_T$ increases.

For the simulations in Section 5.4, the approximation $s^2_{b,k}(\Gamma_{b,k})$ from (5.36) will be used to estimate $\sigma^2_{b,k}$, in place of the channel- and CFO-dependent CRLB.

Table 5.2: Difference between (5.31) and (5.36) for various combinations of N_R and N_T; $\Gamma_{b,k} = 0$ dB, $c_{max} = 10^{-2}$, $N = 128$.

(N_R,N_T)	(1,2)	(1,4)	(2,2)	(4,1)	(4,4)	(8,2)	(2,8)	(16,16)
% Difference	98.0%	34.1%	33.1%	32.3%	6.49%	6.38%	6.26%	0.384%

5.5 Results

For the simulated results, Monte Carlo simulations were done with 10^4 runs on a variety of system configurations. For the m^{th} antenna of the b^{th} BS, the power allocated to each training symbol is defined as $P_{k,b,m} = N_0\Gamma_{b,k}/N_T$. The noise at the receiver, $n_k^{(q)}$, is modeled as additive white Gaussian. The MS-side estimate variance $\sigma_{b,k}^2$ is replaced with $s_{b,k}^2(\Gamma_{b,k})$ in (5.36) from Section 5.4.2. For the BS CFO estimate, the simplified expression (5.10) from Section 5.2 is used here. The distribution for the normalized CFO is defined as uniform over the range $[-c_{max}, +c_{max}]$, and is the same for both BS and MS LOs; while this distribution is based on intuition, and measurements on actual LOs are needed for verification, it has been used before [63]. Unless otherwise specified, the SNRs, $\Gamma_{b,k}$, are identical for all MIMO channels.

Figure 5.5 shows the mean square spread ρ from (5.27) in comparison to simulations of a system with $c_{max} = 10^{-2}$ (i.e., 0.01 radians per symbol time), $K = 6$, $N = 128$, $N_R = N_T = 2$, and a variety of values for B and $\Gamma_{b,k}$. With channels that have identical mean SNRs, the analytical solution follows simulations very closely, as expected for such a straightforward system. The same results are true for channels with non-identical mean SNRs: for a system with $B = 2$, $c_{max} = 10^{-2}$, $K = 3$, $N = 64$, $N_T = N_R = 2$ and with randomly selected channel gains of

$$\mathbf{\Gamma} = \begin{bmatrix} 40 & 35 \\ 38 & 30 \\ 43 & 20 \end{bmatrix} \text{ dB}, \tag{5.37}$$

the analytical solution for the MSS is $\rho = 1.013 \times 10^{-9}$. For 10^4 Monte Carlo realizations, the average is $\rho = 1.012 \times 10^{-9}$. This results in a root MSS of 3.181×10^{-5}, which is an improvement of more than three orders of magnitude on the initial c_{max}. A more detailed system example is given in Section 5.4.1.

Next, the effect of the number of BSs on the MSS was examined. Figure 5.6 shows simulation results in comparison to the analytical expression in (5.30). The difference is

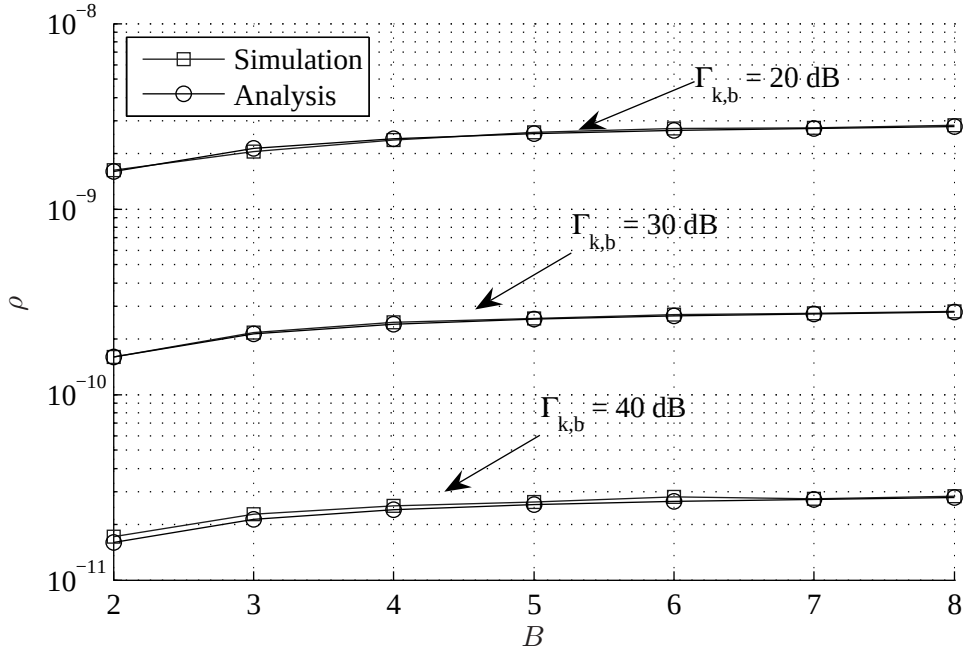

Figure 5.5: Effect of B on BS CFO MSS and comparison of analysis vs. simulation for case 1; $c_{max} = 10^{-2}$, $K = 6$, $N = 128$, $N_R = N_T = 2$.

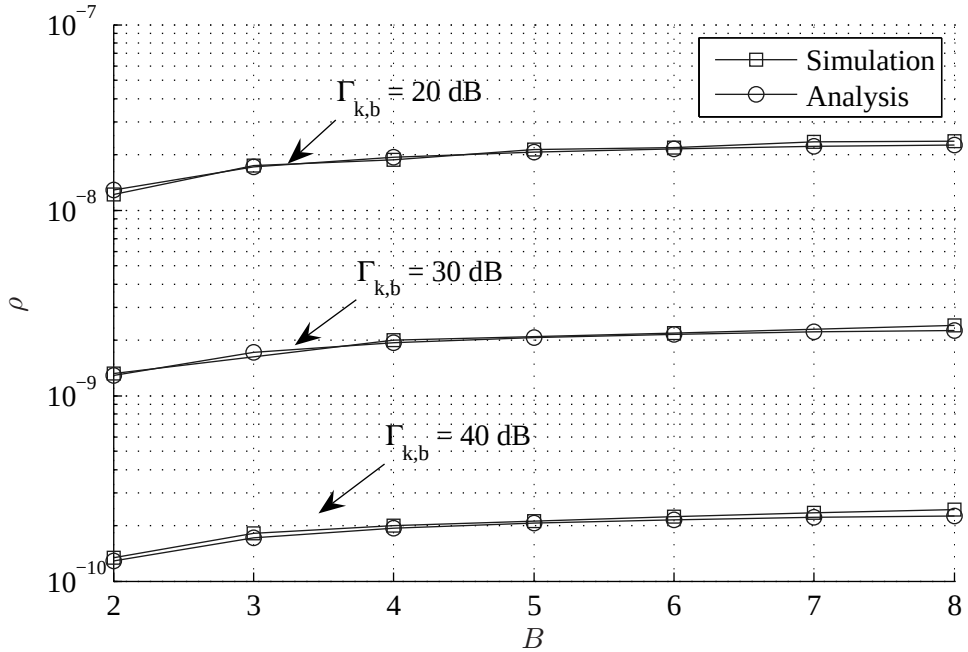

Figure 5.6: Effect of B on BS CFO MSS and comparison of analysis vs. simulation for case 3; $c_{max} = 10^{-2}$, $K = 6$, $N = 64$, $N_R = N_T = 2$.

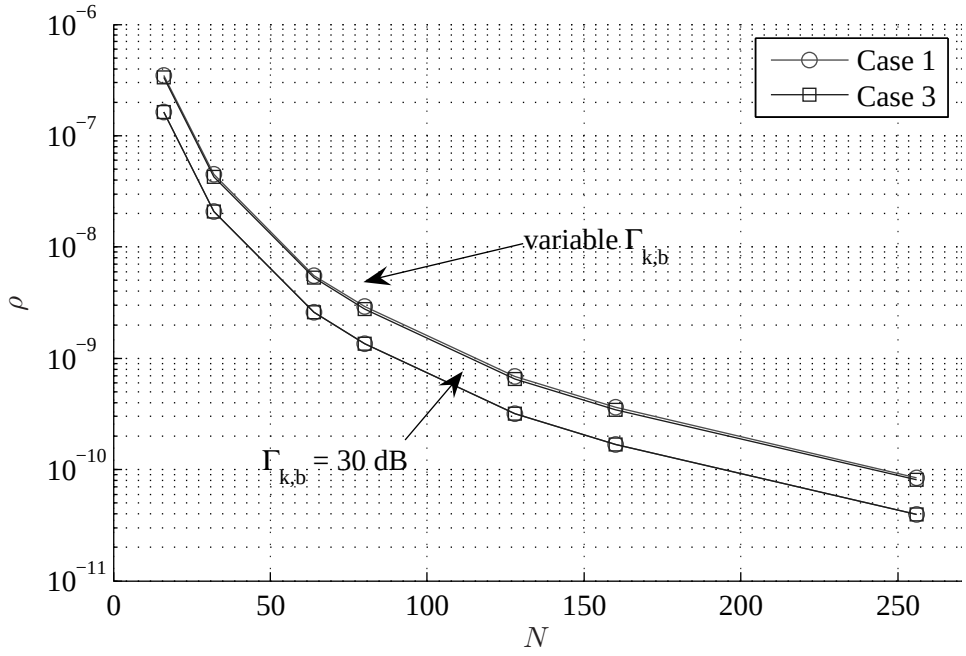

Figure 5.7: Effect of N on analytical BS CFO MSS for case 1 and case 3; $B = 2$, $c_{max} = 10^{-2}$, $K = 3$, $N_R = N_T = 2$.

shown to be small; this shows the effectiveness of removing the MCE as shown in Figure 5.1, where each MS returns only the deviation from the centroid. As in case 1, there is a slight increase in ρ as the number of BSs increases. This result follows from Figure 5.4, which shows that the effect of B on $\sigma^2_{b,k}$ is small, and from the BS CFO estimate MSE in (5.24), which is only dependent on $\sigma^2_{b,k}$ and the number of MSs.

Figure 5.7 shows a comparison of the analytical results for case 1 and case 3 over a variety of TS lengths and SNRs, and demonstrates how the MSS is reduced by increasing the TS length. When the $\Gamma_{b,k}$ are identical for all MIMO channels, the two cases return identical MSSs; this result was predicted in Section 5.3.3. When the $\Gamma_{b,k}$ are set as the non-identical SNRs from the example of Figure 5.5, there is a nearly imperceptible gap between the curves for case 1 and case 3 in Figure 5.7. This shows that the MS CFO estimate removal technique from Section 5.4.1 prevents the MS CFO bias from affecting the MSS of the BS CFOs.

The effect of the number of MSs on the BS CFO MSS for case 3 was also examined. Figure 5.8 shows simulation results, including the analytical results from (5.30). Here we

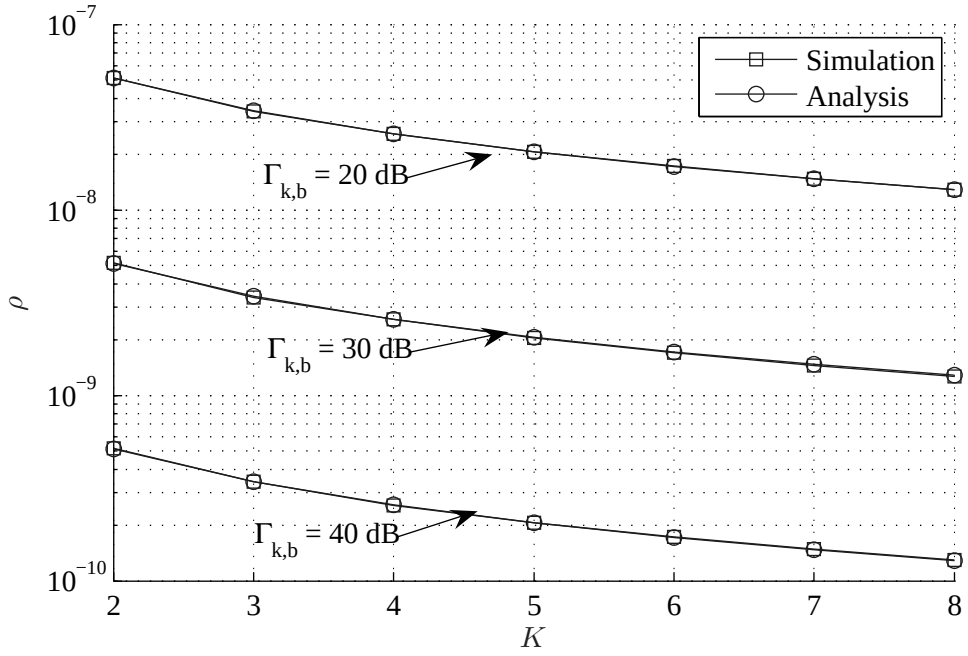

Figure 5.8: Effect of K on BS CFO MSS for case 3, with analytical curves for case 1; $B = 3$, $c_{max} = 10^{-2}$, $N = 64$, $N_R = N_T = 2$.

see a decrease in the BS CFO MSS as the number of MSs increases, which is due to an increase in the number of CFO estimates in the calculation of (5.10). For this example of equal SNRs for all channels, an increase in K results in a linear decrease in BS CFO MSS; by using estimates from $K = 8$ MSs as opposed to only $K = 2$ MSs, the BS CFO MSS is reduced by a factor of four.

Once the SNRs are allowed to vary, the performance of the BS tightening procedure deviates from ρ in (5.30). This is a result of having non-zero MS CFOs. However, the accuracy of the corrected BS CFOs is still improved, although to a lesser degree. For the same system as in Figure 5.8 ($B = 3$, $c_{max} = 10^{-2}$, $K = 5$, $N = 64$, and $N_R = N_T = 2$), simulations were run with $\Gamma_{b,k}$ randomly chosen as either 30 dB or 40 dB with equal probability. The resulting MSS is $\rho = 8.46 \times 10^{-9}$, which is higher than either equal SNR case. For a random SNR of either 20 dB or 40 dB, the MSS rises to $\rho = 1.36 \times 10^{-7}$. This degradation is larger in higher dimensional systems (see Section 5.4.1), so simulations are necessary to gauge the worst case performance of a system. However, even with this degradation, the benefit of BS CFO tightening remains, since the uncertainty of the CFOs

in the 20 dB/40 dB example falls from 2×10^{-2} to the tightened standard deviation of $\sqrt{\rho} = 3.68 \times 10^{-4}$. If we assume a maximum tolerable phase offset of 1×10^{-2} [89], a maximum frame size of $1 \times 10^{-1}/3.68 \times 10^{-4} - 64 = 207$ symbols can be used; note that this calculation does not account for any feedback delay. Without CFO correction at the BSs, the TS length alone would be long enough to violate the phase offset limit.

5.5.1 System Example

To quantify the benefits of the tightening procedure, we offer the following example. Consider a system with $B = 3$, $K = 10$, and a $\Gamma_{b,k}$ that is either 15 dB or 30 dB for each MIMO channel, with equal probability. Also, c_{max} for both the BS and MS is 5×10^{-4}, $N = 64$, $N_T = 4$ and $N_R = 2$. If we use the rough value of 0.1 radians from Chapter 3 for the maximum phase offset before significant capacity loss, an uncorrected system will begin to degrade after approximately $0.1/(5 \times 10^{-4} + 5 \times 10^{-4}) = 100$ symbols. After the TS has been sent, and noting that the CFO is referenced to the beginning of the TS frame, this leaves room for only 36 data symbols.

If we use the BS CFO tightening procedure presented in this paper, the number of data symbols that can be transmitted before the CMBMU channel is degraded can be significantly increased. If we disregard the feedback time of all the $\mathbf{r}_{b,k}^{(-)}$ for this example, simulations show the average MSS of the BS CFOs after estimation and compensation to be 5.15×10^{-8}, or a standard deviation of 2.26×10^{-4}. The corrected BS CFOs are now close enough to each other to avoid significant capacity loss for approximately 454 symbols, or 390 symbols after the TS has been sent.

5.6 Summary

In this Chapter, the topic of CFO estimation and correction for multiple BSs in a CMBMU system is presented. The techniques proposed include ML estimators for both the BS and MS CFO, a feedback technique that removes the bias presented by non-zero MS CFO, and a CRLB-based method to estimate the accuracy of the MCEs. The combination of ML CFO estimation and feedback is termed "BS CFO tightening." Analytical expressions for the mean square spread of the corrected BS CFOs are also derived.

In the tightening procedure, the ML estimators operate on MS-side CFO estimates. First, each MS uses the B BS SNRs and CFO estimates to calculate a ML estimate for the

MS CFO. The MS CFO is then subtracted from the B estimates, and fed-back to the BSs. At the BSs, the BK SNRs and unbiased MS-side CFO estimates are then used to calculate a ML estimate for the BS CFOs. Finally, both the BS CFO estimates and the MS CFO estimates are used for correction at the respective BSs and MSs.

To reduce the amount of overhead necessary when calculating each CFO estimates error variance, an approximation that is based on the Cramer-Rao lower bound is derived. This approximation is made by assuming that the antenna product $N_R N_T >> 1$ and that the system consists of a single BS. The simulations show that the tightening procedure is insensitive to these inaccuracies in the CFO estimate error variance.

The tightening technique is proven to operate just as effectively in the presence of MS CFO as it is without. In addition, since a single iteration is sufficient, this technique can be used at system startup or whenever a BS is added or restarted. The results are encouraging; for normalized BS CFOs on the order of 10^{-3} radians/symbol with a randomly assigned channel SNR of either 15 dB or 30 dB, a ten MS/three BS system using a 64 symbol TS is capable of producing estimator variances of approximately 5.15×10^{-8}. With this amount of accuracy and the assumption of a quasi-static channel, a CMBMU system that uses coordinated beamforming could expect to have a frame size of approximately 390 symbols before experiencing a degradation in capacity. This is in stark contrast to a system without CFO compensation, which could expect a frame size of no more than 36 symbols.

Chapter 6

Multi-CFO Estimation in Time Selective Channels

In Section 3.2, the sum-rate downlink capacity of a CMBMU system in a time-selective channel was examined. When compared individually, the results demonstrated that LO CFO presents a more significant problem to CMBMU downlink capacity than time selectivity. This observation justified the investigations of Chapters 4 and 5, which developed procedures for estimation and correction of multiple CFOs in a quasi-static channel. However, the combination of the two obstacles has not been considered; when CFO estimation is attempted within a time-selective channel, channel variability must be accounted for. In this chapter, an alternative to the LS quasi-static channel estimator (QCE) is presented in the context of multi-CFO estimation. The parameterized channel estimator (PCE) is capable of operating in a time-selective channel, and can be integrated into the existing convex estimation techniques for multiple CFOs (Chapter 4) and the BS CFO correction methods (Chapter 5).

In Section 6.1, the effect of the time-selective channel on the MSE of the CFO and CSI estimates when using the QCE are quantified. Section 6.2 presents a modified version of the ML metric that uses the PCE, which is referred to here as the fade-tolerant metric. Section 6.3 presents simulation results. The time-selective model presented in Section 2.4.2 is used in this chapter. That is, $\mathbf{y}_k^{(t)} \in \mathbb{C}^{NN_R \times 1}$ contains the received samples, $\mathbf{V}^{(t)}(\mathbf{c}_k) \in \mathbb{C}^{N \times BNN_T}$ is the rotated TS matrix, and $\mathbf{h}_k^{(t)} \in \mathbb{C}^{BNN_RN_T \times 1}$ the time-selective channel gains.

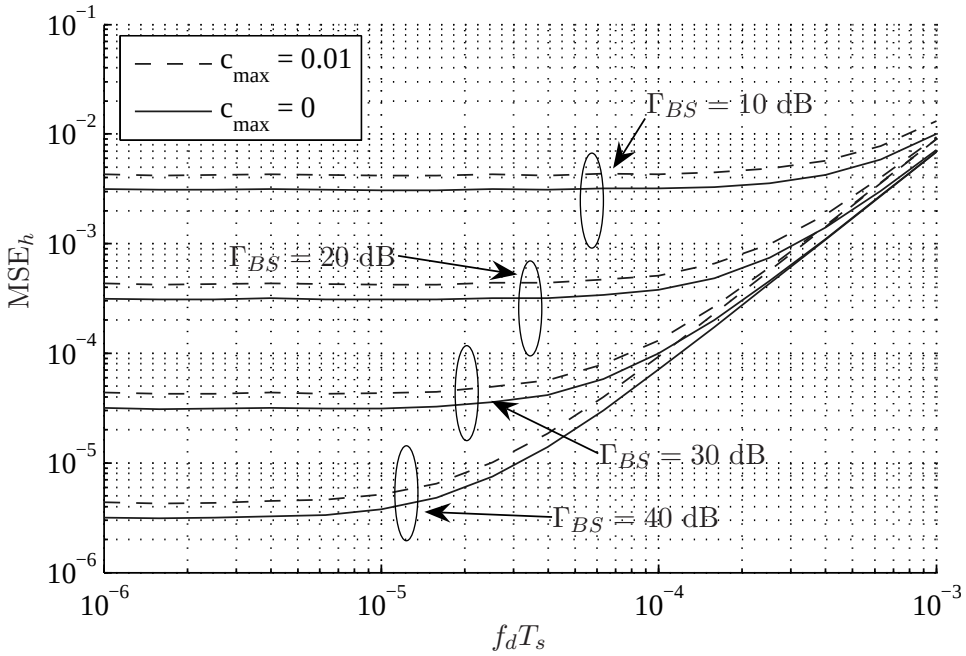

Figure 6.1: Effect of fading channel on sum CSI estimate MSE; $B = 4$, $N = 64$, $N_R = N_T = 2$.

6.1 Effect of Time Selectivity on CFO and CSI MSE

To demonstrate the effect of time selectivity in the synchronization of a CMBMU system, the MSE of joint ST-N CFO and LS CSI estimation is presented here. The following sections present results in fading channels using 10^4 Monte Carlo realizations. All simulations use CFOs that are uniformly distributed between $[-c_{max}, +c_{max}]$. The channels are Rayleigh distributed, with a mean SNR of $\Gamma_{BS} = E_{BS}/N_0$, and have a Jakes spectrum (Section 2.1.2) such that the time autocorrelation function for channel $h^{(t)}_{b,l,k,m}$ is

$$E\left[h^{(t)}_{b,l,k,m}[n]h^{(t)*}_{b,l,k,m}[p]\right] = J_0\left(2\pi f_d T_s\left(n-p\right)\right). \tag{6.1}$$

6.1.1 CSI Estimate

Since all of the CFO estimators presented in chapters 3, 4 and 5 use the LS QCE, the expression for $\hat{\mathbf{h}}_k$ from (4.9) is used here. Figure 6.1 demonstrates the effect of fast fading in a system with $B = 4$, $N = 64$, and the maximum CFO set to $c_{max} = 0$ and 10^{-2}. Since the actual CSI $\mathbf{h}^{(t)}_k$ changes from symbol to symbol and contains BNN_RN_T complex values,

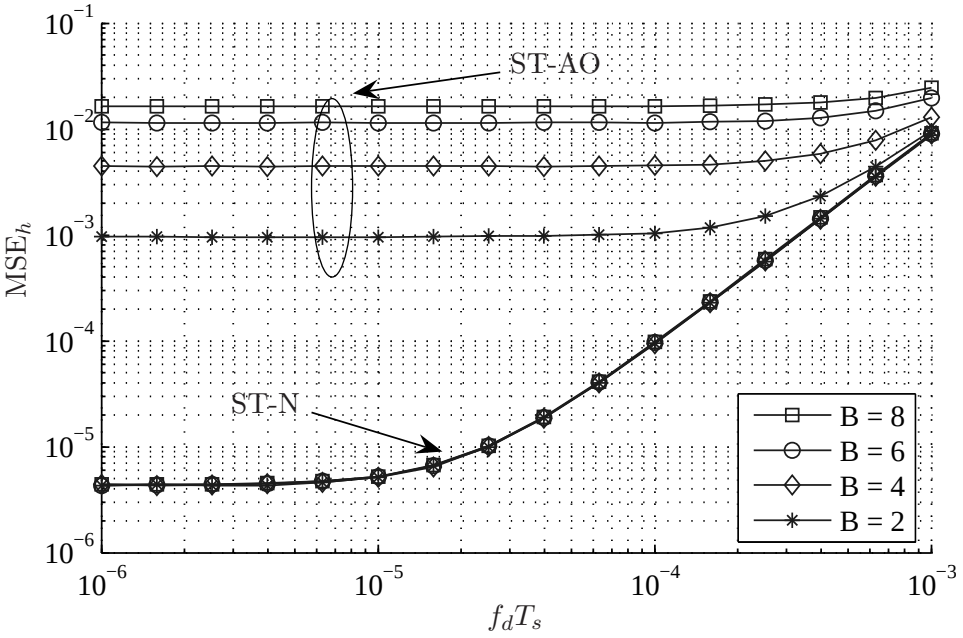

Figure 6.2: Effect of fading channel on MSE$_h$ for simultaneous TSs; $\Gamma_{BS} = 40$ dB, $N = 64$, $c_{max} = 10^{-2}$, $N_R = N_T = 2$.

but the estimated CSI $\hat{\mathbf{h}}_k$ is a snapshot and contains only BN_RN_T values, the MSE of the CSI is defined as

$$\text{MSE}_h = E_h \left[\frac{1}{BNN_RN_T} \sum_{n=1}^{N} \left| \mathbf{h}_k^{(t)}[n] - \hat{\mathbf{h}}_k \right|^2 \right], \tag{6.2}$$

where $\mathbf{h}_k^{(t)}[n]$ and $\hat{\mathbf{h}}_k$ are both length-BN_RN_T vectors. Figure 6.1 shows MSE$_h$ after averaging over 10^4 Monte Carlo realizations. First, it is evident that non-zero CFO has minimal effect on the CSI MSE when compared to the SNR and fade rate. Second, a threshold can be loosely defined above which an increase in the fade rate will result in a increase in MSE$_h$; this increase is proportional to the square of f_dT_s, due to the Jakes autocorrelation function being approximately quadratic for small argument values. This threshold can be used to determine a maximum frame size if the channel variation is not accounted for. Third, an increase in the SNR results in a linear drop in MSE$_h$, since there is no diversity effect in estimation of the CSI. Note that systems with higher SNR are more sensitive to the fading channel, and are subject to a lower fading threshold.

In Figure 6.2, ST-AO and ST-N are compared over both the number of BSs and the fade rate. It is immediately obvious that ST-AO is incapable of handling the effect of the CFO,

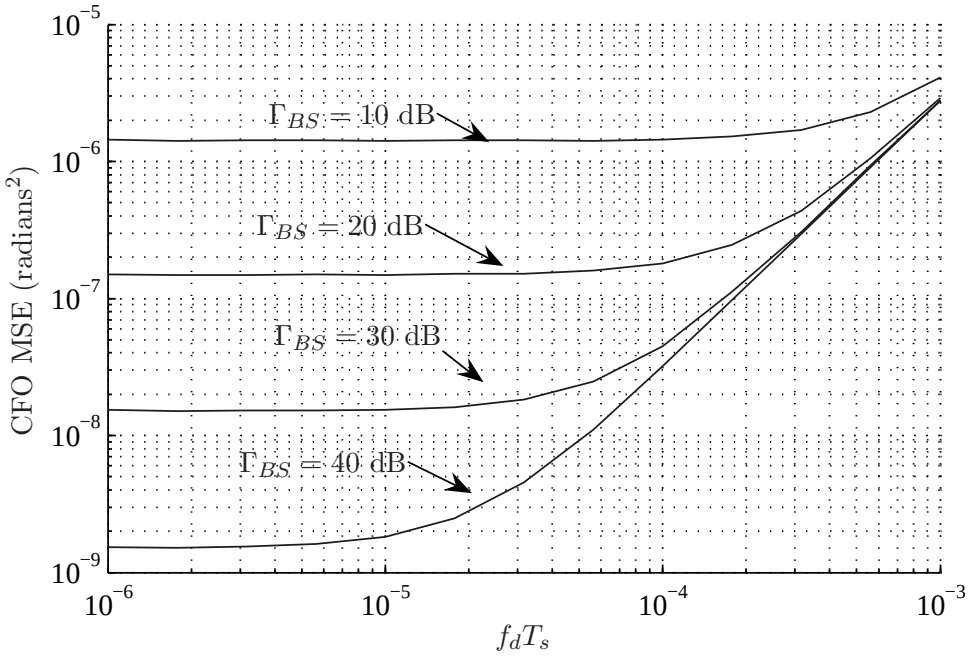

Figure 6.3: Effect of fading channel on ST-N CFO estimate MSE; $B = 4$, $N = 64$, $c_{max} = 10^{-2}$, $N_R = N_T = 2$.

regardless of the fade rate. ST-AO cannot cope with additional BSs because it disregards any cross-correlation due to CFO on the symbols; additional BSs result in extra interference for the estimator. For ST-N, an increase in B does not result in an increase in MSE_h, since ST-N accommodates the cross-correlation coefficients in (4.10).

6.1.2 CFO Estimate

The effect of the fading channel on the ST-N CFO estimate follows the trend shown for the LS QCE closely. Figure 6.3 shows the results of the CFO MSE, where an average of 10^4 Monte Carlo realizations was used to generate the curves. Since the simultaneous TS CFO estimate relies inherently on the QCE, it suffers the same degradation as the fade rate increases.

By using the diversity and extra SNR provided by the N_R antennas at a MS, the performance of the CFO estimator can be improved. Figure 6.4 demonstrates this for a variety of N_R values. For MS antennas that experience independent fading, additional antennas result in a downward shift of the MSE curve. However, the additional receive antennas leave the

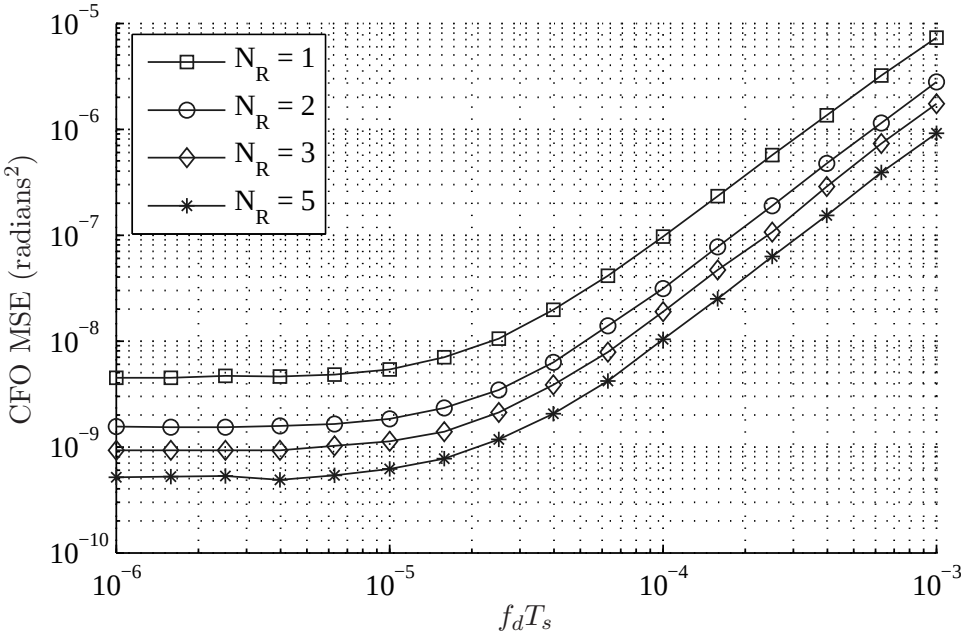

Figure 6.4: Effect of diversity antennas on ST-N CFO estimate MSE in the fading channel; $B = 4$, $N = 64$, $\Gamma_{BS} = 40$ dB, $c_{max} = 10^{-2}$, $N_T = 2$.

threshold unchanged.

6.2 Modified ML Metric

The QCE, which is an LS estimate of the channel gains that is parameterized on the CFOs, is used to remove CSI dependence from the ML metric in section 4.1.2. For the time-selective channel, the limitation of the QCE stems from the fact that the maximum number of independent channel gains that can be estimated equals the maximum rank of the inverse function in (4.10). Since the QCE assumes a quasi-static channel, the maximum rank is

$$rank\left(\mathbf{V}(\mathbf{c}_k)\right) = BN_T. \tag{6.3}$$

To accurately measure each independent gain of a time-selective channel, at every time n, during a length-N TS, would require a matrix with a rank of

$$rank\left(\mathbf{V}^{(t)}(\mathbf{c}_k)\right) = BNN_T. \tag{6.4}$$

This requirement is impossible to meet with the QCE. A channel estimator capable of operating in the fading channel is necessary. The channel estimator can then be integrated into the metric in (4.7).

To provide a good fading channel estimate, a parameter-based estimator is proposed (the PCE) that uses eigenvectors of the channel autocorrelation matrix as basis functions for the gains themselves. This channel gain estimator is similar in construction to [43], which uses polynomials as basis functions. The number of parameterized basis function used per channel gain is defined as P_F. The benefit of using the PCE is that instead of estimating N channel gains per link to capture the channel variability, as few as $P_F = 1$ parameters can be measured with the same effect.

The PCE is derived as follows. First, the $N \times N$ Toeplitz channel autocorrelation matrix is defined as $\mathbf{R}$, where $\mathbf{R}_{n,p} = J_0\left(2\pi f_d T_s(n-p)\right)$. Next, the vectors $\mathbf{q}_F(p_F) \in \mathcal{R}^{N\times 1}$ that hold the eigenvectors corresponding to the p_F^{th} largest eigenvalue of $\mathbf{R}$ are represented in the $N \times P_F$ basis matrix $\mathbf{Q}_F$. The estimation parameters $\hat{\mathbf{a}}_{b,m,k,q}$ are then found such that

$$\hat{\mathbf{h}}_{b,m,k,q}^{(t)} = \mathbf{Q}_F \hat{\mathbf{a}}_{b,m,k,q} \tag{6.5}$$

is the channel estimate. A least squares solution to $\hat{\mathbf{a}}_{k,q} = \left[\mathbf{a}_{1,1,k,q}^T \;\; \mathbf{a}_{1,2,k,q}^T \;\; \cdots \;\; \mathbf{a}_{B,N_T,k,q}^T\right]^T$ as a function of the CFO $\mathbf{c}_k$ is

$$\hat{\mathbf{a}}_{k,q}(\mathbf{c}_k) = \left(\mathbf{Q}^\dagger \mathbf{V}^{(t)\dagger}(\mathbf{c}_k)\mathbf{V}^{(t)}(\mathbf{c}_k)\mathbf{Q}\right)^{-1} \mathbf{Q}^\dagger \mathbf{V}^{(t)\dagger}(\mathbf{c}_k)\mathbf{y}_{k,q}^{(t)}, \tag{6.6}$$

where $\mathbf{Q} = \mathbf{Q}_F \otimes \mathbf{I}_{BN_T}$ represents a separate set of basis functions for each channel gain.

Figure 6.5 shows the first four eigenvectors for the case of $f_d T_s = 10^{-2}$. It is evident that the eigenvectors corresponding to smaller eigenvalues correspond to higher channel variability, as a higher p_F corresponds to a smaller eigenvalue. The value of P_F, or the number of parameters necessary to estimate a channel gain, depends on $f_d T_s$ through $\mathbf{R}$. Table 6.1 shows the value of the first five eigenvalues for a variety of fade rates; these values can be used as a reference to set the number of parameters P_F.

The expressions in (6.5) and (6.6) can be used to replace $\mathbf{h}_k$ in (4.7), resulting in a new ML metric

$$\Lambda_F(\mathbf{c}_k) = \sum_{q=1}^{N_R} \mathbf{y}_{k,q}^{(t)\dagger} \mathbf{V}^{(t)}(\mathbf{c}_k)\mathbf{Q}\left(\mathbf{Q}^\dagger \mathbf{V}^{(t)\dagger}(\mathbf{c}_k)\mathbf{V}^{(t)}(\mathbf{c}_k)\mathbf{Q}\right)^{-1} \mathbf{Q}^\dagger \mathbf{V}^{(t)\dagger}(\mathbf{c}_k)\mathbf{y}_{k,q}^{(t)}. \tag{6.7}$$

A fade-tolerant metric can be created by replacing $\Lambda(\mathbf{c}_k)$ with $\Lambda_F(\mathbf{c}_k)$ for any of the CFO estimators in Chapter 4. Here, the ST-N estimator is given for an example; after replacement,

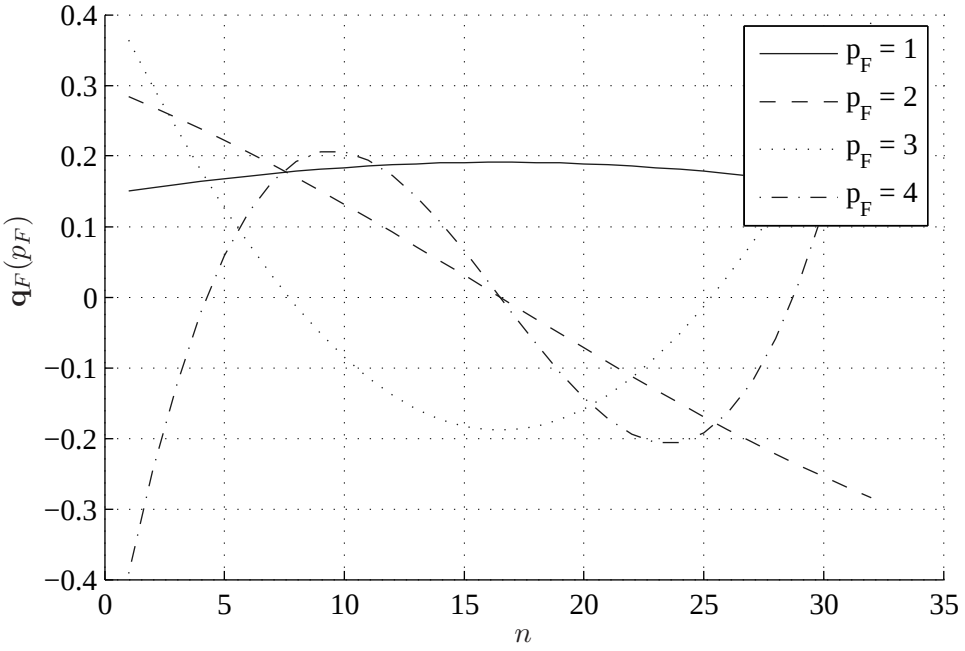

Figure 6.5: Eigenvectors of channel gain autocorrelation matrix $\mathbf{R}$; $f_dT_s = 10^{-2}$, $N = 32$.

Table 6.1: First five eigenvalues of $\mathbf{R}$ versus f_dT_s; $N = 128$.

Eigenvalue	1	2	3	4	5
$f_dT_s = 10^{-5}$	32.00	5.385×10^{-6}	9.002×10^{-14}	3.181×10^{-15}	7.859×10^{-16}
$f_dT_s = 10^{-4}$	32.00	5.384×10^{-4}	9.035×10^{-10}	3.551×10^{-15}	7.935×10^{-16}
$f_dT_s = 10^{-3}$	31.95	5.380×10^{-2}	9.037×10^{-6}	6.466×10^{-10}	2.648×10^{-14}
$f_dT_s = 10^{-2}$	27.28	4.632	9.180×10^{-2}	6.539×10^{-4}	2.571×10^{-6}

$\mathbf{G}'_b(\hat{\mathbf{c}}_k)$ in (4.16), $\mathbf{\Phi}_{b,l}$ in (4.23) and $\mathbf{\Phi}_{b,b}$ in (4.24) become

$$\begin{aligned}\mathbf{G}'_{b,F} &= \mathbf{A}_b^{(t)}(\hat{c}_{b,k})\mathbf{Q}\mathbf{F}^{(t)}(\hat{\mathbf{c}}_k)\mathbf{Q}^\dagger\mathbf{V}^{(t)\dagger}(\hat{\mathbf{c}}_k) + \mathbf{V}^{(t)}(\hat{\mathbf{c}}_k)\mathbf{Q}\mathbf{F}^{(t)}(\hat{\mathbf{c}}_k)\mathbf{Q}^\dagger\mathbf{A}_b^{(t)\dagger}(\hat{c}_{b,k}) \\ &\quad +\mathbf{V}^{(t)}(\hat{\mathbf{c}}_k)\mathbf{Q}\mathbf{E}_b(\hat{\mathbf{c}}_k)\mathbf{Q}^\dagger\mathbf{V}^{(t)\dagger}(\hat{\mathbf{c}}_k),\end{aligned} \tag{6.8}$$

$$\begin{aligned}\mathbf{\Phi}_{b,l,F}(\hat{\mathbf{c}}_k) &= \mathbf{A}_b^{(t)}(\hat{c}_{b,k})\mathbf{Q}\mathbf{F}^{(t)}(\hat{\mathbf{c}}_k)\mathbf{Q}^\dagger\mathbf{A}_l^{(t)\dagger}(\hat{c}_{l,k}) + \mathbf{V}^{(t)}(\hat{\mathbf{c}}_k)\mathbf{Q}\mathbf{E}_b(\hat{\mathbf{c}}_k)\mathbf{Q}^\dagger\mathbf{A}_l^{(t)\dagger}(\hat{c}_{l,k}) \\ &\quad +\mathbf{A}_b^{(t)}(\hat{c}_{b,k})\mathbf{Q}\mathbf{E}_l(\hat{\mathbf{c}}_k)\mathbf{Q}^\dagger\mathbf{V}^{(t)\dagger}(\hat{\mathbf{c}}_k) \\ &= -\mathbf{V}^{(t)}(\hat{\mathbf{c}}_k)\mathbf{Q}\Big(\mathbf{F}^{(t)}(\hat{\mathbf{c}}_k)\mathbf{Q}^\dagger\mathbf{A}_b^{(t)\dagger}(\hat{c}_{b,k})\mathbf{A}_l^{(t)}(\hat{c}_{l,k})\mathbf{Q}\mathbf{F}^{(t)}(\hat{\mathbf{c}}_k) \\ &\quad +\mathbf{E}_b(\hat{\mathbf{c}}_k)\mathbf{Q}^\dagger\mathbf{B}_l^{(t)}(\hat{\mathbf{c}}_k)\mathbf{Q}\mathbf{F}^{(t)}(\hat{\mathbf{c}}_k)\Big)\mathbf{Q}^\dagger\mathbf{V}^{(t)\dagger}(\hat{\mathbf{c}}_k),\end{aligned} \tag{6.9}$$

and

$$\begin{aligned}\mathbf{\Phi}_{b,b,F}(\hat{\mathbf{c}}_k) &= \mathbf{A}_b^{(t)}(\hat{c}_{b,k})\mathbf{Q}\mathbf{F}^{(t)}(\hat{\mathbf{c}}_k)\mathbf{Q}^\dagger\mathbf{A}_b^{(t)\dagger}(\hat{c}_{b,k}) + 2\mathbf{V}^{(t)}(\hat{\mathbf{c}}_k)\mathbf{Q}\mathbf{E}_b(\hat{\mathbf{c}}_k)\mathbf{Q}^\dagger\mathbf{A}_b^{(t)\dagger}(\hat{c}_{b,k}) \\ &\quad +j\mathbf{Z}\mathbf{A}_b^{(t)}(\hat{c}_{b,k})\mathbf{Q}\mathbf{F}^{(t)}(\hat{\mathbf{c}}_k)\mathbf{Q}^\dagger\mathbf{V}^{(t)\dagger}(\hat{\mathbf{c}}_k) \\ &\quad -\mathbf{V}^{(t)}(\hat{\mathbf{c}}_k)\mathbf{Q}\Big(\mathbf{F}^{(t)}(\hat{\mathbf{c}}_k)\mathbf{Q}^\dagger\mathbf{A}_b^{(t)\dagger}(\hat{c}_{b,k})\mathbf{A}_b^{(t)}(\hat{c}_{b,k})\mathbf{Q}\mathbf{F}^{(t)}(\hat{\mathbf{c}}_k) \\ &\quad +\mathbf{E}_b(\hat{\mathbf{c}}_k)\mathbf{Q}^\dagger\mathbf{B}_b^{(t)}(\hat{\mathbf{c}}_k)\mathbf{Q}\mathbf{F}^{(t)}(\hat{\mathbf{c}}_k) \\ &\quad +j\mathbf{F}^{(t)}(\hat{\mathbf{c}}_k)\mathbf{Q}^\dagger\mathbf{V}^{(t)\dagger}(\hat{\mathbf{c}}_k)\mathbf{Z}\mathbf{A}_b^{(t)}(\hat{c}_{b,k})\mathbf{Q}\mathbf{F}^{(t)}(\hat{\mathbf{c}}_k)\Big)\mathbf{Q}^\dagger\mathbf{V}^{(t)\dagger}(\hat{\mathbf{c}}_k),\end{aligned} \tag{6.10}$$

where

$$\begin{aligned}\mathbf{E}_b(\hat{\mathbf{c}}_k) &= -\mathbf{F}^{(t)}(\hat{\mathbf{c}}_k)\mathbf{Q}^\dagger\mathbf{B}_b^{(t)}(\hat{\mathbf{c}}_k)\mathbf{Q}\mathbf{F}^{(t)}(\hat{\mathbf{c}}_k) \in \mathbb{C}^{BN_T\times BN_T}, \\ \mathbf{A}_b^{(t)}(\hat{c}_b) &= [\mathbf{0}_{N\times(b-1)NN_T}\ \ j\mathbf{Z}\mathbf{X}_b^{(t)}\odot\mathbf{\Omega}_b(\hat{c}_b)\ \mathbf{0}_{N\times(B-b)NN_T}] \in \mathbb{C}^{N\times BNN_T} \\ \mathbf{B}_b^{(t)}(\hat{\mathbf{c}}) &= \mathbf{A}_b^{(t)\dagger}(\hat{c}_b)\mathbf{V}^{(t)}(\hat{\mathbf{c}}) + \mathbf{V}^{(t)\dagger}(\hat{\mathbf{c}})\mathbf{A}_b^{(t)}(\hat{c}_b) \in \mathbb{C}^{BNN_T\times BNN_T} \\ \mathbf{F}^{(t)}(\hat{\mathbf{c}}) &= \Big(\mathbf{V}^{(t)\dagger}(\hat{\mathbf{c}})\mathbf{V}^{(t)}(\hat{\mathbf{c}})\Big)^{-1} \in \mathbb{C}^{BNN_T\times BNN_T}.\end{aligned} \tag{6.11}$$

Note that the new basis functions change the rank requirement to

$$rank(\mathbf{Q}^\dagger\mathbf{V}^{(t)\dagger}(\mathbf{c}_k)\mathbf{V}^{(t)}(\mathbf{c}_k)\mathbf{Q}) \geq BN_TP_F. \tag{6.12}$$

Since $\mathbf{Q}$ is $N\times BN_TP_F$ and $rank(\mathbf{Q}) = \min(N, BN_TP_F)$, the new rank condition is achievable as long as $N \geq BN_TP_F$. The following section shows simulations using the new PCE.

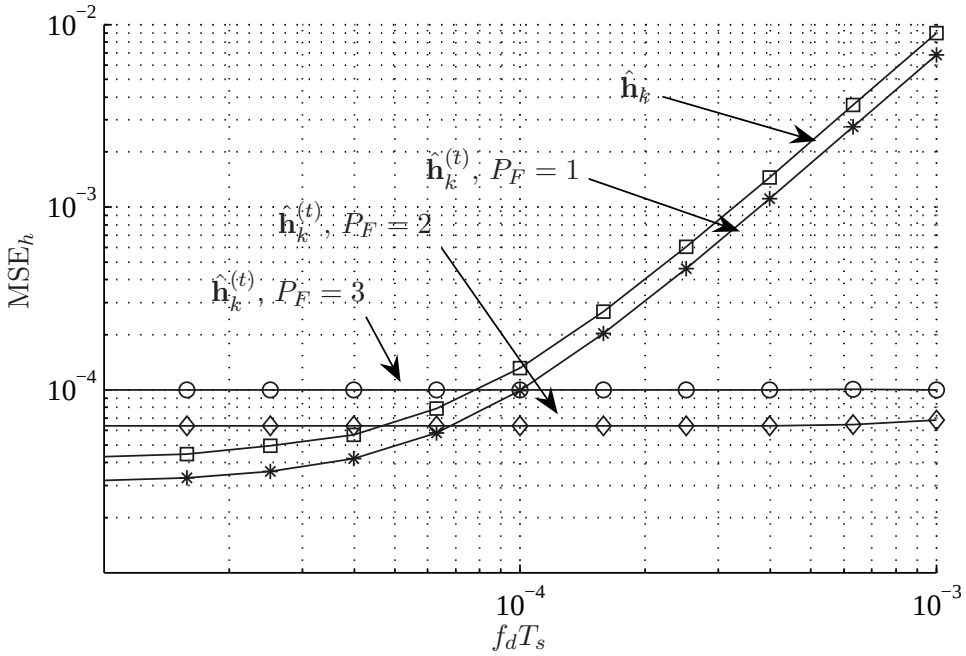

Figure 6.6: Effect of fading channel on CSI estimate MSE for $\hat{\mathbf{h}}_k$ and $\hat{\mathbf{h}}_k^{(t)}$; $B = 4$, $N = 64$, $\Gamma_{BS} = 30$ dB, $c_{max} = 0$, $N_R = N_T = 2$.

6.3 Results

Figure 6.6 compares the MSE_h of $\hat{\mathbf{h}}_k^{(t)}$ in (6.5) which uses the PCE to that of $\hat{\mathbf{h}}_k$ in (4.9) which uses the QCE. Note that for a time-varying channel estimate, MSE_h is redefined as

$$\mathrm{MSE}_h = \frac{1}{BNN_RN_T} \sum_n \left| \mathbf{h}_k[n] - \hat{\mathbf{h}}_k^{(t)}[n] \right|^2. \tag{6.13}$$

These simulations are done in the absence of CFO, with 10^4 Monte Carlo realizations. The figure demonstrates that the MSE of $\hat{\mathbf{h}}_k^{(t)}$ is superior in a fast fading channel. The gap between $\hat{\mathbf{h}}_k$ and $\hat{\mathbf{h}}_k^{(t)}$ in slow fading is due to the number of basis functions P_F. For every added parameter estimate, MSE_h shifts upwards. However, using multiple parameter estimates reduces the CSI estimate sensitivity to f_dT_s. Combined with the results from Section 6.1.2, this suggests that the CFO estimate will have similar benefits when P_F is chosen intelligently.

Next, CFO is included, and the resulting CFO MSE is compared using ST-N with both the original $\Lambda(\mathbf{c}_k)$ metric and the fade-tolerant $\Lambda_F(\mathbf{c}_k)$ metric. These simulations use 10^2 Monte Carlo realizations. The results show that the CFO MSE is highly dependent on N,

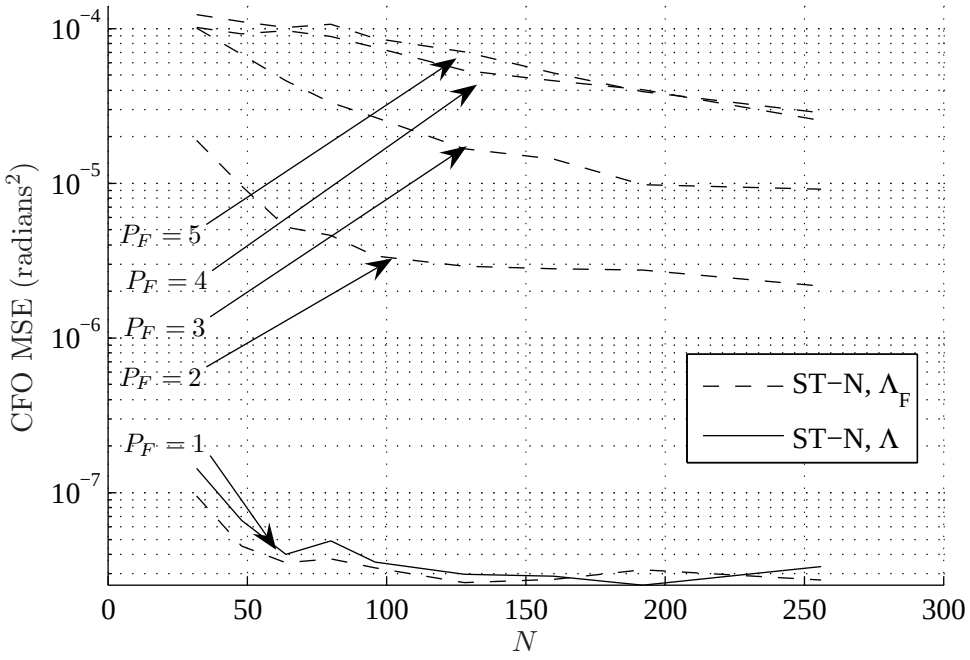

Figure 6.7: CFO MSE versus TS length N; $f_dT_s = 10^{-4}$, $B = 2$, $\Gamma_{BS} = 30$ dB, $c_{max} = 10^{-2}$, $N_R = N_T = 2$.

since for a fixed fade rate and CFO, a larger N results in more variation in the channel gains and larger instantaneous POs near the end of the TS. Figures 6.7-6.9 show the CFO MSE for $f_dT_s = 10^{-4}$, 10^{-3} and 10^{-2} versus the TS length N, respectively.

For $f_dT_s = 10^{-4}$ in Figure 6.7, the channel variability is $\approx 6\%$ of that caused by the CFOs, and as such has no observable impact on the CFO MSE. For $P_F > 1$, the PCE metric has a much higher MSE compared to the QCE metric. Looking at Figure 6.6 shows that at this fade rate, the QCE is just beginning to exhibit degradation.

For $f_dT_s = 10^{-3}$ in Figure 6.8, the channel variability is $\approx 60\%$ of that caused by the CFOs, with the MSE of the two metrics crossing at around $N = 64$ for $P_F = 2$ and $N = 170$ for $P_F = 3$. At this fade rate, the performance of the original metric degrades as N is increased, while the performance improves for the fade-tolerant metric.

Finally, for $f_dT_s = 10^{-2}$ in Figure 6.9, the channel variability is such that the CFO MSE of the original metric is not much better than a random guess, since the variance of the uncompensated CFO is 10^{-4}. However, the fade-tolerant metric can provide around 15 dB improvement if N and P_F are properly chosen. Specifically, CFO MSEs of approximately

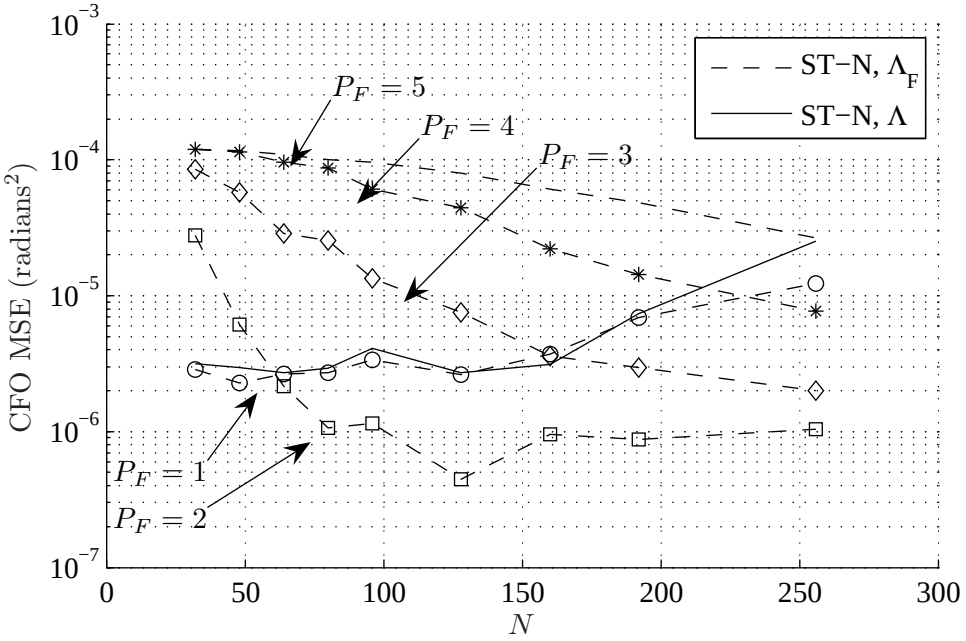

Figure 6.8: CFO MSE versus TS length N; $f_d T_s = 10^{-3}$, $B = 2$, $\Gamma_{BS} = 30$ dB, $c_{max} = 10^{-2}$, $N_R = N_T = 2$.

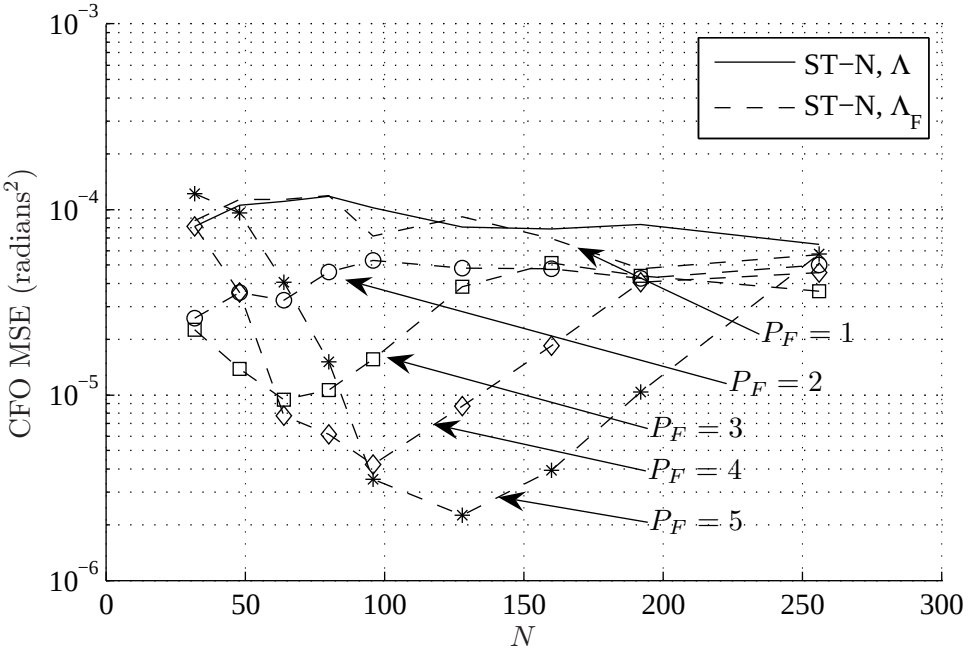

Figure 6.9: CFO MSE versus TS length N; $f_d T_s = 10^{-2}$, $B = 2$, $\Gamma_{BS} = 30$ dB, $c_{max} = 10^{-2}$, $N_R = N_T = 2$.

Table 6.2: Examples of data frame sizes, using the example of capacity degradation with a maximum phase offset of 0.1 radians from Section 3.4.1; $\Gamma_{BS} = 30$ dB, $B = 2$, $c_{max} = 10^{-2}$, $N_R = 2$, $N_T = 4$.

$f_d T_s$	P_F	N	QCE root MSE	Max. # QCE data symbols	PCE root MSE	Max. # PCE data symbols
10^{-3}	2	92	$\approx 1.87 \times 10^{-3}$	53	$\approx 1 \times 10^{-3}$	100
10^{-2}	5	128	$\approx 1 \times 10^{-2}$	10	$\approx 1.55 \times 10^{-3}$	64

1×10^{-5}, 4×10^{-6}, and 2.2×10^{-6} are achievable for $P_F = 3$ and $N = 64$, $P_F = 4$ and $N = 96$, and $P_F = 5$ and $N = 128$, respectively.

A few observations can be made from these simulations. First, when the fade rate is small, it is more effective to use the original metric or to set $P_F = 1$. As the fade rate increases, it is important to match the value of P_F and N to the fade rate when using the fade-tolerant metric. If the value of P_F is too low for a given value of N, then the channel variability is not adequately accounted for; in fact, the MSE using PCE can be much worse than the MSE using QCE. This is visible for the case of $P_F = 3$ for $f_d T_s = 10^{-2}$ and $N > 64$ in Figure 6.9. If the value of P_F is too high, then the system can overcompensate for the channel variability, with a resulting increase in CFO and CSI MSE. This is visible for the case of $P_F = 3$ for $f_d T_s = 10^{-3}$ and $N < 160$. Thus, for higher fade rates, there is an optimum value for N for each P_F, and occurs when the benefit of increasing P_F (capturing the channel variation) exceeds the benefit of increasing N (adding energy and temporal aperture). It is important to note this trade-off: contrary to the quasi-static channel case, increasing N does not result in an unbounded decrease in MSE in a time-selective channel (Figure 6.9).

To demonstrate the effect of the new multi-CFO estimator on CSI estimation, a sample channel is considered. In Figure 6.10, a single channel gain magnitude $|h[n]|$ is plotted versus the symbol time n, along with the PCE estimate $\hat{\mathbf{h}}^{(t)}$ with and without CFO estimation. That is, when CFO estimation is used, the CFO is calculated using ST-N with the metric in (6.7), and if CFO estimation is not used, the $\mathbf{V}^{(t)}(\mathbf{c})$ matrix in (6.6) is replaced with $\mathbf{X}^{(t)}$ to remove CFO dependence. It is evident that in the deep fade, near $n = 70$, PCE with CFO estimation provides a better estimate. This is confirmed by the MSE of each of the estimates, which are $\text{MSE}_h = 6.5 \times 10^{-3}$ with CFO estimation and $\text{MSE}_h = 2.0 \times 10^{-1}$ without CFO estimation.

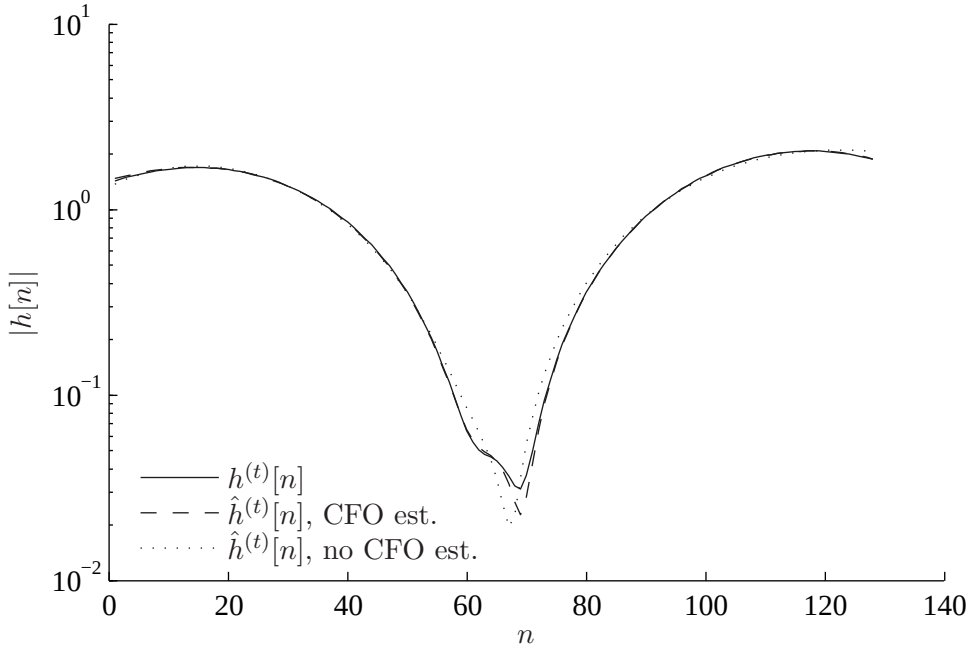

Figure 6.10: CSI magnitude over the TS duration, for the actual channel, the PCE estimate with CFO estimation, and the PCE estimate without CFO estimation; $f_d T_s = 10^{-2}$, $B = 4$, $\Gamma_{BS} = 30$ dB, $c_{max} = 10^{-2}$, $N = 128$, $N_R = N_T = 2$, $P_F = 5$.

Finally, a few comments on the practicality of CFO estimation in the fading channel. In Table 6.2, two examples of the maximum data frame size of QCE and PCE for CFO estimation are given, using data from Figures 6.8 and 6.9. It is clear that CFO estimation with PCE provides a moderate decrease in the root MSE over CFO estimation with QCE. While the data frame size that can be provided by using PCE is much smaller than for the static channel case[1], these examples show that small data frames are still possible in a fast fading channel.

In the case of a low fade rate, a comparison between CFO MSE reduction and the system sum-rate capacity can be done using the capacity curves for the ZF beamformer in Section 3.4, and in particular Figure 3.4. As long as the total phase offset p_{max} is limited within the data frame to below the 10% capacity loss threshold of $p_{max} = 0.1$, the system will encounter minimal capacity loss. Further considerations include the amount of feedback necessary for CFO correction (Chapter 5) and feedback delays that may exist in the system, both of which will decrease the effectiveness of the CFO estimation and correction process. However, as shown in the example of Section 5.5.1, given an appropriate training period, the improvement to the number of full capacity symbol slots will more than make up for the required overhead.

It is possible to improve the MSE values in Table 6.2 further by using PCE with larger values for P_F and N. However, high quality CSI is necessary for downlink beamforming, and up-to-date CSI may not be available in systems with a very large fade rate.

6.4 Summary

This chapter covers the topic of time selectivity for multi-CFO estimation in a CMBMU system.

The effect of a time-selective channel on the MSE of the quasi-static LS channel estimator and the ST-N CFO estimator is investigated. The results demonstrate that a fade rate threshold can be defined, above which the MSE of the CFO or CSI suffers an increase on the order of the square of $f_d T_s$.

For systems that exceed the threshold, a fade-tolerant ML metric is derived which accommodates a parameterized channel estimate, or PCE. This new metric is based on a

[1]For the static channel case with $N = 64$, Figure 4.9 shows a root MSE of 1.73×10^{-4}. Using an allowable maximum phase offset of 0.1 radians results in a possible data frame size of 577 symbols.

model of the channel covariance matrix. The results show that in fast fading conditions, the new fade-tolerant CFO estimates provide superior MSE performance when compared to the original metric, specifically when two conditions are met: that the fade rate is sufficiently large, and that both the TS length and the number of parameters are correctly chosen. For example, in a system with a fade rate of $f_d T_s = 10^{-3}$ and the TS length set to $N = 96$, the fade-tolerant metric gives an almost 5 dB improvement on the CFO MSE.

Examples are given that show the benefit in terms of data symbols of using the PCE for CFO estimation. For instance, with a fade rate of 10^{-2}, the size of the data frame can be increased from 10 symbols to 64 symbols by using the PCE. While these values do not consider the effect of the time selectivity on the channel gains, they do show that CFO can be mitigated for the downlink of a CMBMU system.

Chapter 7

Conclusions

This thesis investigates synchronization techniques for coordinated multibase/multiuser (CMBMU) wireless systems, with a specific focus on carrier frequency offset. The primary goal of this research was to devise efficient synchronization techniques that provide a first step towards implementation of CMBMU systems. In this chapter, a summary of novel contributions and significant findings from the previous chapters are presented.

7.1 Summary of Investigations and Contributions

The major contributions presented in this thesis are summarized as follows:

1. The capacity effects of carrier frequency offset (CFO) caused by independent local oscillators (LOs) at each basestation (BS) are determined to be more detrimental than channel variations due to the mobile fading channel, in Chapter 3.

2. A variety of efficient mobile subscriber (MS) CFO estimators are devised, some of which achieve the Cramer Rao lower bound and can operate under a variety of channel conditions, in Chapters 4 and 6.

3. A novel estimation and correction technique is designed to reduce the spread between BS and MS CFOs, reducing the capacity loss associated with a coordinated multibase system, in Chapter 5.

Details on these contributions are presented here.

Capacity effects of carrier frequency offset

To begin, the effects of a variety of system impairments on the sum-rate capacity of a zero-forcing CMBMU beamformer were examined. Specifically, CFO due to independent local oscillators, CFO due to a single scatterer, and time-selectivity due to multiple scatterers were considered.

- Expressions for the sum-rate capacity are provided for the local oscillator (LO) and time-selective models. For the LO CFO, CFO-induced phase offset causes perturbations on the channel state matrix. Over time, this phase offset accumulates and causes a mismatch between the zero-forcing weights and the actual channel state. For the time-selective channel, Doppler spread is used to model the progressive reduction in correlation between the channel state matrix used to form the zero-forcing weights, and the actual channel state.

- Simulations demonstrate that when comparing the capacity effects of moderate levels of LO accuracy (0.1 to 10 parts per million) to Doppler spreads (4 to 50 km/h), the deterioration caused by LO CFO was more severe. Further, systems that suffer from Doppler can operate if appropriate frame lengths are chosen. Also, given that at least two BSs are coordinating their transmissions, the capacity degradation is shown to be only weakly affected by the number of additional BSs.

Carrier frequency offset estimation techniques

Motivated by the results on the sum-rate capacity, CFO estimators based on known training sequences (TSs) are investigated.

- The Cramer-Rao lower bound (CRLB) for independent LOs at multiple coordinated BSs is derived. This new CRLB is novel since existing multi-CFO CRLBs model CFOs on each antenna-to-antenna link, without several antennas sharing a common CFO, as is considered in this thesis. The CRLB is used is both for assessing estimator performance and for providing error variance values in segmented estimation (see below).

- Estimators based on the gradient and Newton step, collectively referred to as convex estimators, are derived for the CMBMU system. Through simulation, they are shown

to achieve the CRLB. The gradient and Newton estimators are capable of accommodating simultaneously transmitted TSs, which enables them to reduce the power requirements of the RF amplifiers at the BSs. Compared to time orthogonal estimators, the convex techniques reduce transmit power by a factor of B, where B is the number of BSs in the system. Further, compared to implementable time orthogonal techniques, the convex estimators provide a longer time aperture. Finally, the problem of TS correlation, which stems from the CFOs progressive rotation of the training symbols, is eliminated, as evident in the convex estimators optimum performance.

- For frequency selective channels, minor modifications to the signal model allow the convex techniques to accommodate for the interfering multipath. Considering a system modeled with $L + 1$ taps, existing time orthogonal techniques do not provide this without inflating the training period by a factor of L.

- A limit on the CFO, or alternatively on the TS length, that can be estimated is found for the convex estimators. For the maximum normalized CFO c_{max} and the TS length N, the limit is approximated by $N \leq \pi/2c_{max}$. Simulations prove the existence of an error floor if this limit is exceeded.

- To allow for better CFO estimation without an increase in symbol transmit energy or violation of the convexity constraint, segmented estimation is proposed. The segmented estimators, exemplified by the telescoping and combining estimators, use iterative or successive refinement of the CFO estimates. Simulations show that the segmented estimators are capable of converging to the CRLB in the moderate to high SNR range. While the telescoping estimator can provide estimates as the TSs are still arriving, the combining estimator is shown to have better low SNR performance on account of its use of the full TS at every stage.

- The computational complexity of the convex and segmented estimators is shown to be substantially less than that of the optimum maximum likelihood method. In addition, the number of computations can be lowered even further with the use of pre-calculated matrices; it is verified that the Hessian is not highly variable in the convex space, and thus can be pre-calculated for a range of CFOs. Further, matrix sparsity will allow reduction in the size of the matrix products.

- In the presence of time-selective channels, both CFO and CSI estimation is demonstrated to undergo similar performance degradation. A system and SNR dependent threshold can be defined after which the estimate mean square error increases proportionally to the square of the fade rate $f_d T_s$.

- To compensate for time selectivity, modifications to the maximum likelihood (ML) metric are proposed. The modifications consist of replacement of the static channel approximation, which uses a least squares channel estimate, with one that uses the Jakes channel gain autocorrelation model. By parameterizing the eigenvectors of the channel autocorrelation function, a fade-tolerant metric is devised. Simulations are presented for the Newton convex estimator, with results that are dependent on $f_d T_s$ and the number of parameters used, P_F. For example, an improvement of 5 dB is achievable over the static model, for $f_d T_s = 10^{-3}$ and $P_F = 2$.

Estimation and correction for carrier frequency offset

In order to reduce the capacity loss detailed in Chapter 3, it is necessary for the spread between each BS CFO to be significantly reduced. For CMBMU downlink beamforming however, CFO correction of BS CFOs is not possible simply by using the multi-CFO estimation techniques of Chapters 4 and 6 at the MSs. This is due to the mismatch caused by the BS CFOs between the beamforming weights and the actual channel state. As a result, a scheme for estimation and correction for the BS CFOs is investigated. The scheme is based on feedback of the CFO estimates made at all MSs, and is referred to as "BS CFO tightening."

- The presence of independent LOs at each MS is shown to bias the MS-side estimates. To remove the bias, a ML MS CFO estimator is derived, which uses the local MS-side CFO estimates for the BS CFOs. This MS CFO estimate is then removed from the MS-side CFO estimates prior to feedback to the coordinated BSs. Analysis and simulation demonstrates that removal of the bias in this manner negates the effect of non-zero MS CFOs.

- At the coordinated BSs, the unbiased MS-side CFO estimates are used in a ML BS CFO estimator. The spread of the BS CFOs is reduced relative to the number of BS and MS CFOs in the system. It is shown that by increasing the number of MSs, K,

in the system, the BS CFO spread can be reduced on a linear scale with $\log(K)$. For example, in simulations with $B = 3$, $K = 6$, and $c_{max} = 10^{-2}$ radians, a system with an average SNR of 30 dB between the BSs and MSs can expect a BS CFO spread of $\approx 2 \times 10^{-9}$ radians^2. Additionally, it is shown that the BS CFO spread is only weakly affected by an increase in the number of BSs. For the same example above, by increasing the number of BSs from 3 to 8, the BS CFO spread only increases by a factor of ≈ 1.3. This correlates with findings in Chapter 3.

- For systems with different SNRs between each BS and MS, simulations show that BS CFO tightening is effective. For example, with $B = 3$, $K = 5$, and $c_{max} = 10^{-2}$, and with the BS-MS SNR randomly allocated as either 30 dB or 40 dB, the simulated BS CFO spread is 8.46×10^{-9} radians^2. Note that this is an improvement of more than four orders of magnitude from the original BS CFO spread.

- For the ML estimators used to calculate the BS and MS CFOs, the error variance of the MS-side CFO estimates are needed. Instead of using the actual CRLB expression from Chapter 4, an approximation to the error variance is used. The approximation assumes a single BS CFO and that $N_R N_T >> 1$, where N_R and N_T are the number of MS antennas and BS antennas, respectively. Simulations show that the accuracy of this approximation is adequate for the purposes of the ML estimators.

- The final conclusion of this chapter rests on a simple example; that is, for a system with $B = 3$ and $K = 10$, by using the BS CFO tightening procedure, the data frame size of a CMBMU system can be increased from 36 symbols to 390 symbols. This shows that downlink beamforming in a CMBMU system is possible, and that further research into both synchronization and system throughput are warranted.

7.2 Future Research

The topic of synchronization for the CMBMU downlink is vast. Aside from demonstrating that CMBMU system synchronization is possible, a secondary goal of this thesis is to provide motivation for future research into the CMBMU downlink. A number of potential research topics are presented here.

- At the beginning of Chapter 3, it was stated that the effect of phase noise is not considered in the capacity model. Future research into the effect of phase noise in

both CFO estimation and CMBMU systems is warranted. For the non-coordinated system, recent work has been done by Barbieri and Colavolpe [4] that considers the effect of phase noise on the single CFO CRLB; their work demonstrates an SNR error floor which could be very destructive to CMBMU systems. A study into the severity of phase noise that could be expected in a CMBMU system, and a look at the CRLB for multiple CFOs is necessary.

- In Chapter 6, the modified ML metric is shown capable of operating in a fast fading channel. Since beamformers must operate with high quality channel state information, it is necessary to quantify what type of beamformers are operable in this scenario. Background research into existing time-selective beamforming technology, if available, would be instructive. The insertion of periodic training symbols within the data, or data-dependent superimposed training symbols like those proposed by Moosvi et. al. [47], may also prove to be helpful.

- For the static channel case, a capacity or throughput analysis should be done for other beamformers, such as the optimal beamformers in [21] that do not rely so heavily on exact placement of nulls. The optimal beamformers may provide more flexibility for the CMBMU system.

- In terms of practical implementation of a CMBMU system, it may be possible to include coordinated beamforming into the current IEEE 802-16e WiMAX standard [44]. In WiMAX, there exists a "Macro Diversity Handoff" mode for the downlink, as well as smart antenna technology for spatial multiplexing [23]. Future research could include a study into the feasibility of combining these two advanced features to create an operational CMBMU system.

Appendix A

CRLB for Multi-CFO Estimation in a CMBMU System

This bound was derived with the aid of the Slepian-Bangs formula [74]. It was originally presented in [91], with the revised notation below to appear in [92].

After setting $N_{ss} = 1$ and $L = 0$, and assuming a quasi-static channel, the training model presented in Section 2.4.2 for the k^{th} MS is re-written as

$$\mathbf{y} = \mathbf{\Psi}_1(\mathbf{c})\,\mathbf{h} + \mathbf{z}, \tag{A.1}$$

where

$$\begin{aligned}
\mathbf{\Psi}_1(\mathbf{c}) &= \mathbf{I}_{N_R} \otimes \mathbf{D}(\mathbf{c})\,\tilde{\mathbf{X}}\sqrt{\mathbf{P}} \in \mathbb{C}^{NN_R \times BN_R N_T} \\
\mathbf{D}(\mathbf{c}) &= [\mathbf{D}_1(c_1) \;\; \cdots \;\; \mathbf{D}_B(c_B)] \in \mathbb{C}^{N \times BN} \\
\mathbf{D}_b(c_b) &= diag\left(1 \;\; e^{jc_b} \;\; \cdots \;\; e^{jc_b(N-1)}\right) \in \mathbb{C}^{N \times N} \\
\tilde{\mathbf{X}} &= blkdiag(\mathbf{X}_1 \;\; \cdots \;\; \mathbf{X}_B) \in \mathbb{R}^{BN \times BN_T} \\
\mathbf{P} &= blkdiag(\mathbf{P}_1 \;\; \cdots \;\; \mathbf{P}_B) \in \mathbb{R}^{BN_T \times BN_T} \\
\mathbf{P}_b &= (N_0\Gamma_b/N_T)\,\mathbf{I}_{N_T} \in \mathbb{R}^{N_T \times N_T} \\
\mathbf{h} &= \left[\mathbf{h}_{1,1}^T \;\; \cdots \;\; \mathbf{h}_{B,1}^T \;\; \cdots \;\; \mathbf{h}_{B,N_R}^T\right]^T \in \mathbb{R}^{BN_R N_T \times 1},
\end{aligned} \tag{A.2}$$

$\mathbf{X}_b \in \mathbb{R}^{N \times N_T}$ contains the length-N TSs for the N_T antennas at the b^{th} BS and Γ_b is the total MIMO link SNR between the k^{th} MS and the b^{th} BS.

The FIM for the CMBMU CSI and CFO is found as follows. From (4.38), the vector of

CFOs and channel gains $\boldsymbol{\eta}(\mathbf{c},\mathbf{h})$ is defined as

$$\boldsymbol{\eta}(\mathbf{c},\mathbf{h}) = \begin{bmatrix}\mathbf{h}_R^T & \mathbf{h}_I^T & \mathbf{c}^T\end{bmatrix}^T \in \mathbb{R}^{2BN_RN_T+B\times 1}, \tag{A.3}$$

where $\mathbf{h}_R = Re(\mathbf{h})$ and $\mathbf{h}_I = Im(\mathbf{h})$. Also, from (4.39), the received sample vector of $\mathbf{u}(\mathbf{c})$ is defined as

$$\mathbf{u}(\mathbf{c},\mathbf{h}) = \boldsymbol{\Psi}_1(\mathbf{c})\mathbf{h} \in \mathbb{C}^{NN_R\times 1}. \tag{A.4}$$

The FIM can then be represented as

$$\begin{aligned}\mathbf{F}(\mathbf{h},\mathbf{c}) &= \frac{2}{N_0}Re\left(\frac{\partial\mathbf{u}^\dagger(\mathbf{c},\mathbf{h})}{\partial\boldsymbol{\eta}(\mathbf{c},\mathbf{h})}\frac{\partial\mathbf{u}(\mathbf{c},\mathbf{h})}{\partial\boldsymbol{\eta}^T(\mathbf{c},\mathbf{h})}\right) \in \mathbb{R}^{2BN_RN_T+B\times 2BN_RN_T+B} \qquad (A.5)\\ &= \left[\begin{array}{c|c}\mathbf{F}_H(\mathbf{c}) & \mathbf{F}_{Hc}(\mathbf{c},\mathbf{h})\\ \hline \mathbf{F}_{cH}(\mathbf{c},\mathbf{h}) & \mathbf{F}_c(\mathbf{c},\mathbf{h})\end{array}\right].\end{aligned}$$

Using the relation

$$\mathbf{h} = \tilde{\mathbf{I}}\mathbf{h}_{RI}, \tag{A.6}$$

where $\tilde{\mathbf{I}} = [\mathbf{I}_{BN_T} \;\; j\mathbf{I}_{BN_T}]$ and $\mathbf{h}_{RI} = \begin{bmatrix}\mathbf{h}_R^T & \mathbf{h}_I^T\end{bmatrix}^T$, the submatrices are found to be

$$\begin{aligned}\mathbf{F}_H(\mathbf{c}) &= \frac{2}{N_0}Re\left(\frac{\partial\mathbf{u}^\dagger(\mathbf{c},\mathbf{h})}{\partial\mathbf{h}}\frac{\partial\mathbf{u}(\mathbf{c},\mathbf{h})}{\partial\mathbf{h}^T}\right) \in \mathbb{R}^{2BN_RN_T\times 2BN_RN_T} \qquad (A.7)\\ &= \left[\begin{array}{cc}\frac{2}{N_0}Re\left(\frac{\partial\mathbf{u}^\dagger(\mathbf{c},\mathbf{h})}{\partial\mathbf{h}_R}\frac{\partial\mathbf{u}(\mathbf{c},\mathbf{h})}{\partial\mathbf{h}_R^T}\right) & \frac{2}{N_0}Re\left(\frac{\partial\mathbf{u}^\dagger(\mathbf{c},\mathbf{h})}{\partial\mathbf{h}_R}\frac{\partial\mathbf{u}(\mathbf{c},\mathbf{h})}{\partial\mathbf{h}_I^T}\right)\\ \frac{2}{N_0}Re\left(\frac{\partial\mathbf{u}^\dagger(\mathbf{c},\mathbf{h})}{\partial\mathbf{h}_I}\frac{\partial\mathbf{u}(\mathbf{c},\mathbf{h})}{\partial\mathbf{h}_R^T}\right) & \frac{2}{N_0}Re\left(\frac{\partial\mathbf{u}^\dagger(\mathbf{c},\mathbf{h})}{\partial\mathbf{h}_I}\frac{\partial\mathbf{u}(\mathbf{c},\mathbf{h})}{\partial\mathbf{h}_I^T}\right)\end{array}\right]\\ \mathbf{F}_{cH}(\mathbf{c},\mathbf{h}) &= \frac{2}{N_0}Re\left(\frac{\partial\mathbf{u}^\dagger(\mathbf{c},\mathbf{h})}{\partial\mathbf{c}}\frac{\partial\mathbf{u}(\mathbf{c},\mathbf{h})}{\partial\mathbf{h}^T}\right) \in \mathbb{C}^{B\times 2BN_RN_T} \qquad (A.8)\\ &= \left[\begin{array}{cc}\frac{2}{N_0}Re\left(\frac{\partial\mathbf{u}^\dagger(\mathbf{c},\mathbf{h})}{\partial\mathbf{c}}\frac{\partial\mathbf{u}(\mathbf{c},\mathbf{h})}{\partial\mathbf{h}_R^T}\right) & \frac{2}{N_0}Re\left(\frac{\partial\mathbf{u}^\dagger(\mathbf{c},\mathbf{h})}{\partial\mathbf{c}}\frac{\partial\mathbf{u}(\mathbf{c},\mathbf{h})}{\partial\mathbf{h}_I^T}\right)\end{array}\right]\\ \mathbf{F}_{Hc}(\mathbf{c},\mathbf{h}) &= \mathbf{F}_{cH}^\dagger(\mathbf{c},\mathbf{h}) \in \mathbb{C}^{2BN_RN_T\times B} \qquad (A.9)\\ \mathbf{F}_c(\mathbf{c},\mathbf{h}) &= \frac{2}{N_0}Re\left(\frac{\partial\mathbf{u}^\dagger(\mathbf{c},\mathbf{h})}{\partial\mathbf{c}}\frac{\partial\mathbf{u}(\mathbf{c},\mathbf{h})}{\partial\mathbf{c}}\right) \in \mathbb{C}^{B\times B} \qquad (A.10)\end{aligned}$$

Each of the submatrices in (A.7) through (A.10) is defined separately in the following. The FIM for the channel is found using (A.6) and (A.7) to be

$$\begin{aligned}\mathbf{F}_H &= \frac{2}{N_0}Re\left(\frac{\partial\mathbf{u}^\dagger}{\partial\boldsymbol{\eta}}\frac{\partial\mathbf{u}}{\partial\boldsymbol{\eta}^T}\right) \qquad (A.11)\\ &= \frac{2}{N_0}Re\left\{\begin{bmatrix}\mathbf{I}_{N_R} & j\mathbf{I}_{N_R}\\ -j\mathbf{I}_{N_R} & \mathbf{I}_{N_R}\end{bmatrix} \otimes \sqrt{\mathbf{P}_k}^T\tilde{\mathbf{X}}^T\mathbf{D}^\dagger(\mathbf{c}_k)\mathbf{D}(\mathbf{c}_k)\tilde{\mathbf{X}}\sqrt{\mathbf{P}_k}\right\}.\end{aligned}$$

The joint FIM for the channel and CFO is found using (A.8) and (A.9) to be

$$\begin{aligned}\mathbf{F}_{cH}(\mathbf{c},\mathbf{h}) &= \frac{2}{N_0} Re\left(\frac{\partial \mathbf{u}^{\dagger}(\mathbf{c},\mathbf{h})}{\partial \mathbf{c}} \frac{\partial \mathbf{u}(\mathbf{c},\mathbf{h})}{\partial \mathbf{h}^T}\right) \\ &= \frac{2}{N_0} Re\left\{\tilde{\mathbf{h}}^{\dagger}\left[-j\boldsymbol{\Psi}_1^{\dagger}(\mathbf{c},\mathbf{h})\boldsymbol{\Psi}_2(\mathbf{c}) \;\; \boldsymbol{\Psi}_1^{\dagger}(\mathbf{c},\mathbf{h})\boldsymbol{\Psi}_2(\mathbf{c})\right]\right\}\end{aligned} \tag{A.12}$$

and

$$\mathbf{F}_{Hc}(\mathbf{c},\mathbf{h}) = \frac{2}{N_0} Re\left(\frac{\partial \mathbf{u}^{\dagger}(\mathbf{c},\mathbf{h})}{\partial \mathbf{h}} \frac{\partial \mathbf{u}(\mathbf{c},\mathbf{h})}{\partial \mathbf{c}^T}\right) = \mathbf{F}_{cH}^{\dagger}(\mathbf{c},\mathbf{h}), \tag{A.13}$$

respectively, where

$$\tilde{\mathbf{h}} = blkdiag\left(\mathbf{h}_1 \;\; \cdots \;\; \mathbf{h}_B\right) \in \mathbb{C}^{BN_RN_T \times B} \tag{A.14}$$

$$\boldsymbol{\Psi}_2(\mathbf{c}) = \begin{bmatrix} \left(\mathbf{I}_{N_R} \otimes \mathbf{Z}\mathbf{D}_1\left(c_1\right)\mathbf{X}_1\sqrt{P_1}\right)^T \\ \vdots \\ \left(\mathbf{I}_{N_R} \otimes \mathbf{Z}\mathbf{D}_1\left(c_B\right)\mathbf{X}_B\sqrt{P_B}\right)^T \end{bmatrix} \in \mathbb{C}^{NN_R \times BN_RN_T}.$$

The FIM for the CFO alone is found using (A.10) to be

$$\begin{aligned}\mathbf{F}_{c}(\mathbf{c},\mathbf{h}) &= \frac{2}{N_0} Re\left(\frac{\partial \mathbf{u}^{\dagger}(\mathbf{c},\mathbf{h})}{\partial \mathbf{c}} \frac{\partial \mathbf{u}(\mathbf{c},\mathbf{h})}{\partial \mathbf{c}^T}\right) \\ &= \frac{2}{N_0} Re\{\tilde{\mathbf{h}}^{\dagger}\boldsymbol{\Psi}_2^{\dagger}(\mathbf{c})\boldsymbol{\Psi}_2(\mathbf{c})\tilde{\mathbf{h}}\}.\end{aligned} \tag{A.15}$$

For the CRLB, it is necessary to take the inverse of the FIM in (A.5). Since we are primarily interested in the diagonals of the CRLB, specifically the matrix $\left[\mathbf{F}^{-1}\right]_c \in \mathbb{C}^{B\times B}$ which corresponds to the lower right block of $\mathbf{F}^{-1}$, the use of the matrix inverse lemma [62] would be efficient. The matrix inverse lemma states that the inverse of the lower right block of $\mathbf{F}$ is

$$\mathbf{CRLB}_c(\mathbf{c},\mathbf{h}) = \left[\mathbf{F}^{-1}(\mathbf{c},\mathbf{h})\right]_c = \left(\mathbf{F}_c(\mathbf{c},\mathbf{h}) - \mathbf{F}_{cH}(\mathbf{c},\mathbf{h})\mathbf{F}_H^{-1}(\mathbf{c})\mathbf{F}_{Hc}(\mathbf{c},\mathbf{h})\right)^{-1}. \tag{A.16}$$

For the channel state, the CRLB is

$$\mathbf{CRLB}_H(\mathbf{c},\mathbf{h}) = \left[\mathbf{F}^{-1}(\mathbf{c},\mathbf{h})\right]_H = \left(\mathbf{F}_H(\mathbf{c}) - \mathbf{F}_{Hc}(\mathbf{c},\mathbf{h})\mathbf{F}_c^{-1}(\mathbf{c},\mathbf{h})\mathbf{F}_{cH}(\mathbf{c},\mathbf{h})\right)^{-1}. \tag{A.17}$$

The average of the diagonals of $\mathbf{CRLB}_c$ and $\mathbf{CRLB}_H$ correspond to the Cramer-Rao lower bound for the CFO and CSI, respectively, so

$$CRLB_c = \frac{1}{B} trace\left(\mathbf{CRLB}_c\right) \tag{A.18}$$

$$CRLB_H = \frac{1}{BN_RN_T} trace\left(\mathbf{CRLB}_H\right). \tag{A.19}$$

Appendix B

Marginalization of Channel Gains

Beginning with the conditional pdf in (4.6), the marginalization of the channel gain vector can be represented as

$$\begin{aligned} p\left(\mathbf{y}|\mathbf{c}\right) &= \int_{\mathbf{h}} p\left(\mathbf{y}|\mathbf{h},\mathbf{c}\right) p\left(\mathbf{h}\right) d\mathbf{h} \\ &= \int_{\mathbf{h}} \frac{1}{\left(2\pi\right)^{NN_R} NN_R N_0} e^{-\frac{\left|\left|\mathbf{y}-\overline{\mathbf{V}}(\mathbf{c})\mathbf{h}\right|\right|^2}{2N_0}} p\left(\mathbf{h}\right) d\mathbf{h}, \end{aligned} \tag{B.1}$$

where $p\left(\mathbf{h}\right)$ is the pdf of the channel gain vector $\mathbf{h}$. For the Rayleigh channel,

$$p\left(\mathbf{h}\right) = \frac{1}{\left(2\pi\right)^{BN_RN_T} BN_RN_T} e^{-\frac{\left|\left|\mathbf{h}\right|\right|^2}{2}}. \tag{B.2}$$

The pdf in (B.1) can be simplified by weighting and combining the exponential terms, then completing the square in the numerator. First, rearranging the exponential terms results in

$$\begin{aligned} \left|\left|\mathbf{y}-\overline{\mathbf{V}}(\mathbf{c})\mathbf{h}\right|\right|^2 + N_0\left|\left|\mathbf{h}\right|\right|^2 &= \mathbf{y}^\dagger\mathbf{y} - \mathbf{y}^\dagger\overline{\mathbf{V}}(\mathbf{c})\mathbf{h} - \mathbf{h}^\dagger\overline{\mathbf{V}}^\dagger(\mathbf{c})\mathbf{y} \\ &\quad + \mathbf{h}^\dagger\left(\overline{\mathbf{V}}^\dagger(\mathbf{c})\overline{\mathbf{V}}(\mathbf{c}) + N_0\mathbf{I}_{BN_RN_T}\right)\mathbf{h}. \end{aligned} \tag{B.3}$$

Substituting $\mathbf{C} = \overline{\mathbf{V}}^\dagger(\mathbf{c})\overline{\mathbf{V}}(\mathbf{c}) + N_0\mathbf{I}_{BN_RN_T}$, expanding $\mathbf{C} = \mathbf{Q}\mathbf{\Xi}^2\mathbf{Q}^\dagger$ via eigendecomposition, and then substituting again with a product of the channel gains $\mathbf{u} = \mathbf{\Xi}\mathbf{Q}^\dagger\mathbf{h}$ reforms (B.3) into

$$\mathbf{y}^\dagger\mathbf{y} - \mathbf{y}^\dagger\overline{\mathbf{V}}(\mathbf{c})\mathbf{B}\mathbf{u} - \mathbf{u}^\dagger\mathbf{B}^\dagger\overline{\mathbf{V}}^\dagger(\mathbf{c})\mathbf{y} + \mathbf{u}^\dagger\mathbf{u}, \tag{B.4}$$

where $\mathbf{h} = \left(\mathbf{\Xi}\mathbf{Q}^\dagger\right)^{-1}\mathbf{u} = \mathbf{B}\mathbf{u}$ and $\mathbf{Q}$ is a unitary matrix. Completing the square transforms (B.4) into

$$\left|\left|\mathbf{u} - \mathbf{B}^\dagger\overline{\mathbf{V}}^\dagger(\mathbf{c})\mathbf{y}\right|\right|^2 + \mathbf{y}^\dagger\left(\mathbf{I}_{NN_R} - \overline{\mathbf{V}}(\mathbf{c})\mathbf{B}\mathbf{B}^\dagger\overline{\mathbf{V}}^\dagger(\mathbf{c})\right)\mathbf{y}. \tag{B.5}$$

At this point, the marginalized pdf in (B.1) can be expressed as

$$p\left(\mathbf{y}|\mathbf{c}\right) = \frac{1}{\left(2\pi\right)^{NN_R} NN_R \left|\mathbf{\Xi Q}^{\dagger}\right|} e^{-\frac{\mathbf{y}^{\dagger}\left(\mathbf{I}_{NN_R} - \overline{\mathbf{V}}(\mathbf{c})\mathbf{B}\mathbf{B}^{\dagger}\overline{\mathbf{V}}^{\dagger}(\mathbf{c})\right)\mathbf{y}}{2N_0}} \times \int_{\mathbf{u}} \frac{1}{\left(2\pi\right)^{BN_RN_T} BN_RN_TN_0} e^{-\frac{\left|\left|\mathbf{u}-\mathbf{B}^{\dagger}\overline{\mathbf{V}}^{\dagger}(\mathbf{c})\mathbf{y}\right|\right|^2}{2N_0}} d\mathbf{u}, \tag{B.6}$$

where the term $\left|\mathbf{\Xi Q}^{\dagger}\right|$ in the denominator is the Jacobian that transforms the pdf from $\mathbf{h}$ to $\mathbf{u}$. Since the term within the integral in (B.6) falls to one (the integral of a Gaussian distribution), the simplified expression for the marginalized pdf is

$$p\left(\mathbf{y}|\mathbf{c}\right) = \frac{1}{\left(2\pi\right)^{NN_R} NN_R \left|\mathbf{\Xi Q}^{\dagger}\right|} e^{-\frac{\mathbf{y}^{\dagger}\left(\mathbf{I}_{NN_R} - \overline{\mathbf{V}}(\mathbf{c})\mathbf{B}\mathbf{B}^{\dagger}\overline{\mathbf{V}}^{\dagger}(\mathbf{c})\right)\mathbf{y}}{2N_0}}. \tag{B.7}$$

Bibliography

[1] S. Ahmed, S. Lambotharan, A. Jakobsson, and J. A. Chambers. Mimo frequency-selective channels with multiple-frequency offsets: estimation and detection techniques. *IEE Proc. Commun.*, 152(4):489–494, August 2005.

[2] S. M. Alamouti. A simple transmit diversity technique for wireless communications. *IEEE J. on Sel. Areas Commun.*, 16(8):1451–1458, October 1998.

[3] M. N. Bacha, J. S. Evans, and S. V. Hanly. On the capacity of mimo cellular networks with macrodiversity. In *IEEE Australian Commun. Theory Workshop (ACTW)*, volume 1, pages 105–109, Perth, Australia, February 2006.

[4] A. Barbieri and G. Colavolpe. On the cramer-rao bound for carrier frequency estimation in the presence of phase noise. *IEEE Trans. Wireless Commun.*, 6(2):575–582, February 2007.

[5] M. Bengtsson and B. Ottersten. Optimal transmit beamforming using convex optimization, 1999. Submitted to IEEE Trans. Commun.

[6] O. Besson and P. Stoica. On parameter estimation of mimo flat-fading channels with frequency offsets. *IEEE Trans. Signal Process.*, 51(3):602–613, March 2003.

[7] A. Bletsas and A. Lippman. Implementing cooperative diversity antenna arrays with commodity hardware. *IEEE Commun. Mag.*, 44(12):33–40, December 2006.

[8] S. D. Blostein and H. Leib. Multiple antenna systems: their role and impact in future wireless access. *IEEE Commun. Mag.*, 41(7):94–101, July 2003.

[9] S. Boyd and L. Vandenberghe. *Convex Optimization*. Cambridge University Press, Cambridge, UK, 2006.

[10] Z. Cao, U. Tureli, and Y. D Yao. Deterministic multiuser carrier-frequency offset estimation for interleaved ofdma uplink. *IEEE Trans. Commun.*, 52(9):1585–1594, September 2004.

[11] J. K. Cavers. Fast acquisition of carrier and timing in low snr and fading using diversity antennas. In *IEEE Vehic. Tech. Conf. (VTC)*, volume 3, pages 1748–1752, Phoenix, AZ, USA, May 1997.

[12] J. K. Cavers. *Mobile Channel Characteristics*. Springer, Norwell, MA, 2000.

[13] J. K. Cavers. Frequency offset estimation in space-time coding and mimo applications, 2002. Written for Tait Communications.

[14] R. L. U Choi, M. T. Ivrlac, R. D. Murch, and W. Utschick. On strategies of multiuser mimo transmit signal processing. *IEEE Trans. Wireless Commun.*, 3(6):1936–1941, January 2004.

[15] S. T Chung, A. Lozano, and H. C. Huang. Approaching eigenmode blast channel capacity using v-blast with rate and power feedback. In *IEEE Veh. Technol. Conf. (VTC)*, volume 2, pages 915–919, Atlantic City, NJ, USA, October 2001.

[16] M. Costa. Writing on dirty paper. *IEEE Trans. Inf. Theory*, 29(3):439–441, May 1983.

[17] T. A. Cover and J. A. Thomas. *Elements of Information Theory*. John Wiley and Sons, Inc., New York, New York, 1991.

[18] Croven Crystals. Precision quartz crystals.

[19] N. H. Dawod, I. D. Marsland, and R. H. M. Hafez. Improved transmit steering for mimo-ofdm downlinks with distributed base station antenna arrays. *IEEE J. Sel. Areas Commun.*, 24(3):419–426, March 2006.

[20] K. Deng, Y. Tang, S. Shao, and S. Li. Carrier frequency offset estimation for mimo correlated fading channels. In *IEEE Wireless Commun. and Networking Conf. (WCNC)*, volume 1, pages 1035–1038, Hong Kong, March 2007.

[21] A. Ekbal and J. M. Cioffi. Distributed transmit beamforming in cellular networks - a convex optimization perspective. In *IEEE Int. Conf. Commun. (ICC)*, volume 4, pages 2690–2694, Seoul, South Korea, May 2005.

[22] U. Erez and St Brink. A close-to-capacity dirty paper coding scheme. *IEEE Trans. Inf. Theory*, 51(10):3417–3432, October 2005.

[23] WiMAX Forum. Mobile wimax part i: A technical overview and performance evaluation. Technical report, 2006.

[24] G. J. Foschini and M. J. Gans. On limits of wireless communications in a fading environment when using multiple antennas. *Wireless Personal Commun.*, 6(3):311–335, March 1998.

[25] M. Ghogho and A. Swami. Training design for multipath channel and frequency-offset estimation in mimo systems. *IEEE Trans. Signal Process.*, 54(10):3957–3965, October 2006.

[26] G. D. Golden, C. J. Foschini, R. A. Valenzuela, and P. W. Wolniansky. Detection algorithm and initial laboratory results using v-blast space-time communication architecture. *IEEE Elec. Lett.*, 35(1):14–16, January 1999.

[27] A. Goldsmith, S. A. Jafar, N. Jindal, and S. Vishwanath. Capacity limits of mimo channels. *IEEE J. Sel. Areas Commun.*, 21(5):684–702, June 2003.

[28] S. J. Grant and J. K. Cavers. Performance enhancement through joint detection of cochannel signals using diversity arrays. *IEEE Trans. Commun.*, 46(8):1038–1049, August 1998.

[29] D. Hammarwall, M. Bengtsson, and B. Ottersten. On downlink beamforming with indefinite shaping constraints. *IEEE Trans. Signal Processing [see also Acoustics, Speech, and Signal Processing, IEEE Transactions on]*, 54:3566–3580, September 2006.

[30] S. V. Hanly. Capacity and power control in spread spectrum macrodiversity radio networks. *IEEE Trans. Commun.*, 44(2):247–256, February 1996.

[31] B. Hassibi and B. M. Hochwald. How much training is needed in multiple-antenna wireless links? *IEEE Trans. Inform. Theory*, 49(4):951–963, April 2003.

[32] S. Haykin. *Communication Systems*. John Wiley and Sons, Inc., New York, New York, 1994.

[33] S. Haykin. *Adaptive Filter Theory*. Prentice-Hall, Inc., Upper Saddle River, NJ, 2001.

[34] M. G. Hebley and D. P. Taylor. The effect of diversity on a burst-mode carrier-frequency estimator. *IEEE Trans. Commun.*, 46(4):553–560, April 1998.

[35] M. F. Iskander. *Electromagnetic Fields and Waves*. Prentice-Hall, Inc., Englewood Cliffs, NJ, 1992.

[36] H. Jung and M. D. Zoltowski. Timing and frequency offset estimation in asynchronous multi-user ofdm systems. In *IEEE Military Commun. Conf. (MILCOM)*, volume 3, pages 1491–1495, Monterey, CA, USA, October 2004.

[37] S. Karimifar and J. K. Cavers. Optimized cell ordering for multiuser macrodiversity detection with the conditional metric merge algorithm. In *IEEE 60th Veh. Technol. Conf. (VTC)*, volume 3, pages 1865–1869, Los Angeles, CA, USA, September 2004.

[38] J. Y. Kim, G. L. Stuber, and I. F. Akyildiz. Macrodiversity power control in hierarchical cdma cellular systems. *IEEE J. Sel. Areas Commun.*, 19(2):266–276, February 2001.

[39] R. Knopp and P. A. Humblet. Information capacity and power control in single-cell multiuser communications. In *IEEE Int. Conf. on Commun. (ICC)*, volume 1, pages 331–335, Seattle, WA, USA, June 1995.

[40] G. Lebrun. A study of wireless modem performance using multiple element antennas, 2004. Ph.D. Thesis.

[41] G. Lebrun, J. Gao, and M. Faulkner. Mimo transmission over a time-varying channel using svd. *IEEE Trans. Wireless Commun.*, 4(2):757–764, March 2005.

[42] J. Y Lee, H. C Liu, and H. Samueli. Performance analysis of synchronization errors on digital adaptive beamforming for a high bit-rate qam receiver. In *IEEE 47th Veh. Technol. Conf. (VTC)*, volume 2, pages 1064–1068, Phoenix, AZ, USA, May 1997.

[43] W. S. Leon and D. P. Taylor. Generalized polynomial-based receiver for the flat fading channel. *IEEE Trans. Commun.*, 51(6):896–899, June 2003.

[44] B. Li, Y. Qin, C. P. Low, and C. L. Gwee. A survey on mobile wimax. *IEEE Commun. Mag.*, 45(12):70–75, December 2007.

[45] Y. Liu, T. F. Wong, and A. Pandharipande. Timing estimation in multiple-antenna systems over rayleigh flat-fading channels. *IEEE Trans. Signal Process.*, 53(6):2074–2088, June 2005.

[46] P. H. Moose. A technique for orthogonal frequency division multiplexing frequency offset correction. *IEEE Trans. Commun.*, 42(10):2908–2914, October 1994.

[47] S. M. A. Moosvi, D. C. McLernon, A. G. Orozco-Lugo, M. M. Lara, and M. Ghogho. Carrier frequency offset estimation using data-dependent superimposed training. *IEEE Commun. Lett.*, 12(3):179–181, March 2008.

[48] M. Morelli. Timing and frequency synchronization for the uplink of an ofdma system. *IEEE Trans. Commun.*, 52(2):296–306, February 2004.

[49] R. Mudumbai, G. Barriac, and U. Madhow. On the feasibility of distributed beamforming in wireless networks. *IEEE Trans. Wireless Commun.*, 6(5):1754–1763, May 2007.

[50] J. Murtagh, 2006. Personal communications.

[51] B. K. Ng and E. S. Sousa. On bandwidth-efficient multiuser-space-time signal design and detection. *IEEE J. on Sel. Areas in Commun.*, 20(2):320–329, February 2002.

[52] B. L. Ng, J. Evans, and S. Hanly. Distributed linear multiuser detection in cellular networks based on kalman smoothing. In *IEEE Global Telecommun. Conf. (GLOBECOM)*, volume 1, pages 134–138, Dallas, TX, USA, November 2004.

[53] B. L. Ng, J. S. Evans, S. V. Hanly, and D. Aktas. Transmit beamforming with cooperative base stations. In *IEEE Int. Symp. on Inf. Theory (ISIT)*, pages 1431–1435, Adelaide, Australia, September 2005.

[54] M. K Oh, X. Ma, G. B. Giannakis, and D. J Park. Cooperative synchronization and channel estimation in wireless sensor networks. In *Conf. Record of Thirty-Seventh Asilomar Conf. On Signals, Systems and Computers*, volume 1, pages 238–242, Pacific Grove, CA, USA, November 2003.

[55] D. P. Palomar, J. M. Cioffi, and M. A. Lagunas. Joint tx-rx beamforming design for multicarrier mimo channels: a unified framework for convex optimization. *IEEE Trans. Signal Processing [see also Acoustics, Speech, and Signal Processing, IEEE Transactions on]*, 51:2381–2401, September 2003.

[56] S. Parkvall, E. Dahlman, A. Furuskar, Y. Jading, M. Olsson, S. Wanstedt, and K. Zangi. Lte-advanced - evolving lte towards imt-advanced. In *IEEE 68th Veh. Technol. Conf. (VTC)*, Calgary, September 2008.

[57] J. G. Proakis. *Digital Communications*. McGraw-Hill, New York, New York, 2001.

[58] T. S. Rappaport. *Wireless Communications: Principles and Practice*. Prentice Hall, Upper Saddle River, NJ, 1996.

[59] F. Rashid-Farrokhi, K. J. R. Liu, and L. Tassiulas. Transmit beamforming and power control for cellular wireless systems. *IEEE J. Sel. Areas Commun.*, 16(8):1437–1450, October 1998.

[60] F. Rashid-Farrokhi, L. Tassiulas, and K. J. R. Liu. Joint power control and beamforming for capacity improvement in wireless networks with antenna arrays. In *Global Telecommun. Conf. (GLOBECOM)*, volume 1, pages 555–559, London, UK, November 1996.

[61] J. M. Romero-Jerez, C. Tellez-Labao, and M. Ruiz-Garcia. Effects of macrodiversity on cellular cdma networks with fast power control under multipath fading. In *IEEE Int. Conf. Commun. (ICC)*, volume 7, pages 4280–4284, Paris, France, June 2004.

[62] L. L. Scharf. *Statistical signal processing: detection, estimation and time series analysis*. Addison-Wesley, Reading, MA, 1991.

[63] M. Schellmann and S. Stanczak. Multi-user mimo channel estimation in the presence of carrier frequency offsets. In *Conf. Record of Thirty-Ninth Asilomar Conf. On Signals, Systems and Computers*, volume 1, pages 462–466, Pacific Grove, CA, USA, October 2005.

[64] M. Schubert and H. Boche. Solution of the multiuser downlink beamforming problem with individual sinr constraints. *IEEE Trans. Veh. Technol.*, 53(1):18–28, January 2004.

[65] M. Schubert and H. Boche. Iterative multiuser uplink and downlink beamforming under sinr constraints. *IEEE Trans. Signal Process.*, 53(7):2324–2334, July 2005.

[66] G. Seber and A. Lee. *Linear Regression Analysis*. John Wiley and Sons, Hoboken, NJ, 2002.

[67] P. M. Shankar. Outage probabilities of a mimo scheme in shadowed fading channels with micro- and macrodiversity reception. *IEEE Trans. Wireless Commun.*, 7(6):2015–2019, June 2008.

[68] L. Shao and S. Roy. Downlink multicell mimo-ofdm: an architecture for next generation wireless networks. In *IEEE Wireless Commun. and Networking Conf. (WCNC)*, volume 2, pages 1120–1125, New Orleans, LA, USA, March 2005.

[69] F. Simoens and M. Moeneclaey. Reduced complexity data-aided and code-aided frequency offset estimation for flat-fading mimo channels. *IEEE Trans. Wireless Commun.*, 5(6):1558–1567, June 2006.

[70] B. Sklar. A structured overview of digital communications-a tutorial review-part i. *IEEE Commun. Mag.*, 21(5):4–17, August 1983.

[71] B. Sklar. A structured overview of digital communications–a tutorial review–part ii. *IEEE Commun. Mag.*, 21(7):6–21, October 1983.

[72] Q. H. Spencer, A. L. Swindlehurst, and M. Haardt. Zero-forcing methods for downlink spatial multiplexing in multiuser mimo channels. *IEEE Trans. Signal Process.*, 52(2):461–471, February 2004.

[73] P. Stoica and O. Besson. Training sequence design for frequency offset and frequency-selective channel estimation. *IEEE Trans. Commun.*, 51(11):1910–1917, November 2003.

[74] P. Stoica and R. Moses. *Introduction to Spectral Analysis*. Prentice Hall, Upper Saddle River, NJ, 1997.

[75] I. E. Telatar. Capacity of multi-antenna gaussian channels. *European Transactions on Telecommunications*, 10(6):585–595, 1999.

[76] D. Veronesi and D. L. Goeckel. Multiple frequency offset compensation in cooperative wireless systems. In *Global Telecommun. Conf. (GLOBECOM)*, pages 1–5, San Fransisco, CA, USA, November 2006.

[77] B. Vucetic and J. Yuan. *Turbo Codes: Principles and Applications*. Kluwer, Norwell, MA, 2000.

[78] C. Wang and R. D. Murch. Adaptive cross-layer resource allocation for downlink multiuser mimo wireless system. In *IEEE Veh. Technol. Conf. (VTC)*, volume 3, pages 1628–1632, Stockholm, Sweden, May 2005.

[79] R. Wang and G. B. Giannakis. Approaching mimo channel capacity with reduced-complexity soft sphere decoding. In *IEEE Wireless Commun. and Networking Conf. (WCNC)*, volume 3, pages 1620–1625, Atlanta, GA, March 2004.

[80] X. Wang and H. V. Poor. Iterative (turbo) soft interference cancellation and decoding for coded cdma. *IEEE Trans. Commun.*, 47(7):1046–1061, July 1999.

[81] L. Welburn, J. K. Cavers, and K. W. Sowerby. Multiuser-macrodiversity detection in rayleigh fading channels. In *IEEE Veh. Tech. Conf. (VTC)*, volume 5, pages 2340–2347, Boston, MA, USA, September 2000.

[82] L. R. Welburn, J. K. Cavers, and K. W. Sowerby. Multiuser macrodiversity detection in asynchronous ds-cdma systems. *IEEE Trans. Wireless Commun.*, 3(2):544–554, March 2004.

[83] S. B. Wicker. *Error Control Systems for Digital Communication Systems.* Prentice Hall, Upper Saddle River, NJ, 1995.

[84] J. Winters. Optimum combining in digital mobile radio with cochannel interference. *IEEE J. Sel. Areas Commun.*, 2(4):528–539, July 1984.

[85] J. H. Winters, J. Salz, and R. D. Gitlin. The impact of antenna diversity on the capacity of wireless communication systems. *IEEE Trans. Commun.*, 42(2,3,4):1740–1751, February/March/April 1994.

[86] Y. S Yeh, J. C. Wilson, and S. C. Schwartz. Outage probability in mobile telephony with directive antennas and macrodiversity. *IEEE J. Sel. Areas Commun.*, 2(4):507–511, July 1984.

[87] T. Yoo and A. Goldsmith. On the optimality of multiantenna broadcast scheduling using zero-forcing beamforming. *IEEE J. Sel. Areas Commun.*, 24(3):528–541, March 2006.

[88] W. Yu, W. Rhee, S. Boyd, and J. M. Cioffi. Iterative water-filling for gaussian vector multiple-access channels. *IEEE Trans. Inform. Theory*, 50(1):145–152, January 2004.

[89] B. W. Zarikoff and J. K. Cavers. Carrier frequency offset in coordinated multibase mimo narrowband systems. In *IEEE 67th Veh. Technol. Conf. (VTC)*, volume 1, pages 872–877, Singapore, May 2008.

[90] B. W. Zarikoff and J. K. Cavers. Multiple carrier frequency offset and channel state estimation in the fading channel. In *IEEE 68th. Veh. Technol. Conf. (VTC)*, Calgary, September 2008.

[91] B. W. Zarikoff and J. K. Cavers. Multiple frequency offset estimation for the downlink of coordinated mimo systems. *IEEE J. Sel. Areas Commun.*, 26(6):901–912, August 2008.

[92] B. W. Zarikoff and J. K. Cavers. Coordinated multibase systems: Carrier frequency offset estimation and correction. *IEEE Trans. Wireless Commun.*, to be published.

[93] B. W. Zarikoff, J. K. Cavers, and S. Bavarian. An iterative groupwise multiuser detector for overloaded mimo applications. *IEEE Trans. Wireless Commun.*, 6(2):443–447, February 2007.

[94] Y. Zeng, A. R. Leyman, and Y. C Liang. Estimation of time delay, frequency o set and channel for asynchronous multiuser mimo with multipath. In *IEEE 65th Veh. Technol. Conf. (VTC)*, pages 1455–1459, Dublin, Ireland, April 2007.